Surface Trap Passivation and Characterization of Lead Sulfide Quantum Dots for Optical and Electrical Applications

by

Gyuweon Hwang

B.S., Seoul National University (2004)
M.S., Seoul National University (2006)

Submitted to the Department of Materials Science and Engineering
in Partial Fulfillment of the Requirements for the Degree of

Doctor of Philosophy
at the
MASSACHUSETTS INSTITUTE OF TECHNOLOGY
June 2015

Signature of Author Signature redacted
Department of Materials Science and Engineering
May 14, 2015

Certified by Signature redacted
Moungi G. Bawendi
Lester Wolfe Professor of Chemistry
Thesis Supervisor

Certified by Signature redacted
Klavs F. Jensen
Warren K. Lewis Professor of Chemical Engineering
Professor of Materials Science and Engineering
Thesis Reader

Accepted by Signature redacted
Donald R. Sadoway
Chair, Departmental Committee on Graduate Students

Surface Trap Passivation and Characterization of Lead Sulfide Quantum Dots for Optical and Electrical Applications

by

Gyuweon Hwang

Submitted to the Department of Materials Science and Engineering on May 14, 2015,
in partial fulfillment of the requirements for the degree of
Doctor of Philosophy

Abstract

Quantum dots (QDs) are semiconductor nanocrystals having a size comparable to or smaller than its exciton Bohr radius. The small size of QDs leads to the quantum confinement effects in their electronic structures. Their unique optical properties, including a tunable emission from UV to IR, make QDs attractive in optoelectronic applications. However, further improvements in device performance are required to make them competitive. One well-known factor that presently limits the performance of QD thin film devices is sub-bandgap states, also referred to as trap states. For instance, trap states impair optical properties and device performance by providing alternative pathways for exciton quenching and carrier recombination. Chemical modification of QDs has been commonly used for passivating trap states and thereby improving QD devices. However, the influence of chemical modifications of ligands, QD surfaces, or synthetic routes on electrical properties of QD thin films is not sufficiently characterized.

Suppressing the trap states in QD thin films is a key to improve the performance of QD-based optoelectronics. This requires fundamental understanding of trap state source, which is lacking in these materials. In this thesis, I pursue to find a systematic method to control density of trap states by exploring different characterization techniques to investigate trap states in QD thin films. These attempts provide insight to develop a rationale for fabricating better performing QD devices.

This thesis focuses on the trap states in IR emitting lead sulfide (PbS) QD thin films, which have great potential for application in photovoltaics, light emitting diodes (LEDs), photodetectors, and bio-imaging. Previously, QD thin films are treated with different ligands to passivate trap states and thereby improve the device performance. Through my work, I pursued to unveil the electrical characteristics and chemical origin of trap states, and develop a strategy to suppress the trap states.

First, I hypothesize that surface dangling bonds are a major source of trap states. An inorganic shell layer comprised of cadmium sulfide (CdS) is introduced to PbS QDs to passivate the surface states. Addition of CdS shell layers on PbS QDs yields an enhanced stability and quantum yield (QY), which indicates decreased trap-assisted exciton quenching. These PbS/CdS core/shell QDs have a potential for deep-tissue bio-imaging in short-wavelength IR windows of 1550-1900 nm. However, the shell layer acts as a transport barrier for carriers and results in a significant decrease in conductivity. This hinders the incorporation of the core/shell QDs in electrical applications. An improved reaction condition enables the synthesis of PbS/CdS QDs having a monolayer-thick CdS shell layer. These QDs exhibit QY and stability comparable to thick-shell PbS/CdS QDs. Incorporation of these thin-shell QDs improves external quantum efficiency of IR QD-LEDs by 80 times compared to PbS core-only QDs.

In the second phase of my work, I explore capacitance-based measurement techniques for better understanding of the electrical properties of PbS QD thin films. For in-depth analysis, capacitance-based techniques are introduced, which give complementary information to current-based measurements that are widely used for the characterization of QD devices. Nyquist plots are used to determine the dielectric constant of QD films and impedance analyzing models to be used for further analysis. Mott-Schottky measurements are implemented to measure carrier concentration and mobility to compare PbS core-only and PbS/CdS core/shell QD thin films. Drive-level capacitance profiling is employed to characterize the density and energy level of trap states when QD films are oxidized.

Lastly, I investigate the chemical origin of trap states and use this knowledge to suppress the trap states of PbS QD thin films. Photoluminescence spectroscopy and X-ray photoelectron spectroscopy show that standard ligand exchange procedures for device fabrication lead to the formation of sub-bandgap emission features and under-charged Pb atoms. Our experimental results are corroborated by density functional theory simulation, which shows that the presence of Pb atoms with a lower charge in QDs contributes to sub-bandgap states. The trap states generated after ligand exchange were significantly reduced by oxidation of under-charged Pb atoms using 1,4-benzoquinone. The density of trap states measured electrically with drive-level capacitance profiling shows that this reduces the electrical trap density by a factor of 40.

In this thesis, I characterized trap states and showed that by suppressing the trap states we can modify the electrical properties of QD thin films, which influence the performance of QD devices directly. This work is a starting point to fully analyze the trap states in QD thin devices and thereby provides insight to design a rationale for fabricating better performing QD devices.

Thesis Suprevisor: Moungi G. Bawendi
Title: Lester Wolfe Professor of Chemistry

Acknowledgements

There are many people who I would like to thank for making this thesis possible. My journey for starting over graduate school in different field other than my 5-year experience in research could be completed with supports from people around me. This acknowledgement is a small token of my appreciation for their supports. I sincerely thank God for allowing me have these people, having the relationship with me, and what he has done and is willing to do before, during, and after my Ph.D. study.

First of all, I owe my deepest gratitude to Prof. Moungi Bawendi for giving me an opportunity to work in his group. He has provided an example of what it means to be a scientist. I am extremely fortunate to have worked with him and have learned science under his guidance. He has also been patient with me as I learned from mistakes and struggles. The chance to have autonomy and straggling has been one of indispensable experiences and the best opportunities to step up during the Ph.D. studies.

All the Bawendi group members I have met are not only great lab mates, colleagues, friends but also remarkable teachers to me. There is a saying in the Analects of Confucius (論語), 三人行 必有我帥—three walk together, there must be a teacher for me (rough translation by me, and this is written in Chinese, not Korean!). I really appreciate every discussion, inspiration, and conversation with my lab mates. I am sincerely thankful for having a wonderful time with all of you, the first-year office mates—Dan, Jenn, Jose, He Wei, and Russ—and device sub-group—Scott, Liang-Yi, Jie, Darcy, Dong-Kyun, Jenn, Chia-hao, Whitney—and also Raoul, Jian, Jie, Mark, Igor, Justin, Dan F., Oliver, Jess, Francesca, Thomas, Andrew, David, Lisa, Jing, Brian, Zoran, Peter, Numpon, August, Cliff, Ou, Yue, and Dan. M. I would like to mention my thanks to some individually: Jenn taught me basic procedures in Wet lab experiments, made me a chemist, and she is also a good mentor and friend. Jose is always a good consultant to me in Chemistry, and He Wei shared his fume hood with me for years. Dan as DMSE class mates, we spent much time in the classrooms as well in the lab. Mark is a wonderful lab mate to share exciting science as well as great fun, and he has helped me a lot in English writing also. I also have a good collaborators—Geoffrey, Patrick, Joel, Katherine and Yasuhiro in Bulovic group and Donghun in Grossman group—for expanding and embracing my research.

I am indebted to many of my colleagues and friends to support me outside the lab. The members of KGMSE, and families in Step Stone Church are provided me another space to

relax and enjoy a life in Boston. Moreover, I have many old friends—5 undergraduate classmates and 14 high school classmates—who have attended MIT and Harvard as graduate students or post-docs and they have made me feel this new strange place, Boston, as a familiar pleasant place. Sung Whan, Yong Cheol, Jae-Jin, Hyung-kyu, Sangyeop, Dong-Hoon, Seunghyuk, Sungwook, Jungwon, Kyung-sun, Hee-Chul, Miso, Sungjoon, Gyu-Boong, and Hyeyeon—it is a blessing to me having such many good old friends over 10,000 km away from home. And I thank my previous advisor, Prof. Cheol Seong Hwang, who is still willing to give advices and encourage me all the time.

Lastly, I thank my family. To my parents and my lovely wife, Hee-Sun: I know that "thank you" is not enough to express my heart, but there is nothing more to say apart from "thank you".

Thanks again to all who were there with me throughout the whole time and made my life possible up to this point. Without you this thesis would not be possible. I will remember you all.

This work was supported in part by the U. S. Army Research Laboratory and the U. S. Army Research Office through the Institute for Soldier Nanotechnologies, under contract number W911NF-13-D-0001, and by the Samsung Advanced Institute of Technology.

Preface

Parts of this thesis were reproduced in part from the following references:

- Supran GJ, Song KW, Hwang GW, Correa RE, Scherer J, Dauler EA, Shirasaki Y, Bawendi MG, Bulovic V. "High-Performance Shortwave-Infrared Light-Emitting Devices Using Core-Shell (PbS-CdS) Colloidal Quantum Dots" *Advanced Materials*. **2015**, 27 (8), 1437-1442.

- Hwang GW, Kim D, Cordero JM, Wilson MWB, Chuang, CHM, Grossman JC, Bawendi MG. "Identifying and Eliminating Emissive Sub-Bandgap States in Thin Films of PbS Nanocrystals" *Advanced Materials*. (accepted)

Table of Contents

Abstract 3

Acknowledgements 5

Preface 7

Chapter 1. Introduction 17

1.1 Quantum Confinement System 17

1.2 Lead Sulfide QDs 18

1.3 Applications of Colloidal PbS QDs 21

1.4 Trap States 23

1.5 Thesis Overview 25

Chapter 2. PbS/CdS Core/Shell QDs 27

2.1 Material System 28

2.2 Synthesis 31

2.2.1 PbS Core Synthesis 31

2.2.2 PbS/CdS Core/Shell QD Synthesis 34

2.3 Characterization of PbS/CdS Core/Shell QDs 37

2.3.1 Optical Characterization 37

2.3.2 Shell Thickness 41

2.4 SWIR *in vivo* Deep-Tissue Imaging 43

2.5 Light Emitting Diodes Applications 47

2.5.1 Electrical Conductivity of PbS/CdS QD Thin Films 48

2.5.2 Monolayer Shell Growth 49

2.5.3 Device Characterization 53

2.6 Summary 57

Chapter 3. Electrical Characterization of QD Thin Films 59
3.1 Capacitance 60
3.2 Measuring Dielectric Constant 61
3.3 Junction Capacitance 65
3.3.1 Mott-Schottky Analysis 66
3.3.2 Drive-Level Capacitance Profiling 69
3.4 Summary 76
Chapter 4 Chemical Origin of Trap States 77
4.1 Motivation 77
4.2 Experiments 78
4.3 Sub-Bandgap Emission and Its Origin 79
4.4 Theoretical Study 88
4.5 Effect of Oxidation 96
4.6 Summary 98
Chapter 5 Conclusion and Future Outlook 99
Appendix A Self-Assembly Binary Nanocrystal Superlattice 103
A.1 Motivation 103
A.2 Preparation 104
A.3 Characterization 107
A.4 Device Applications 110
References 113

List of Figures

Figure 1-1. Emission from different sizes of PbS QDs shows the wide range of band gap tunability. 20
Figure 1-2. A typical experimental set-up using Schlenk line for synthesis of colloidal PbS QDs. The image is adopted from Refs: [25] 21
Figure 1-3. Schematic diagram of trap-assisted process—electron capture (c_n), electron emission (e_n), hole capture (c_p), and hole emission (e_p). 24
Figure 2-1. Schematic diagram of band alignment for the type-I (CdSe/ZnS) (left) and type–II (CdTe/CdSe) (right) heterojunction QDs, figure taken from Ref: [52] 29
Figure 2-2. Vertical section at 50 at.% S of the Pb-Cd-S ternary phase diagram, images taken from Refs: [56] and [57]. 30
Figure 2-3. Schematic diagram demonstrating the stages of nucleation and growth for the QDs in the framework of the LaMer model. Image is taken from Refs: [59] 32
Figure 2-4. Schematic diagram of the cation exchange reaction 35
Figure 2-5. Transmission electron microscopy (TEM) images of (a) PbS core-only QDs and (b) PbS/CdS core/shell QDs 35
Figure 2-6. A typical experimental set-up using Schlenk line for cation exchange reaction with colloidal PbS QDs and Cd-precursors. The image is adopted from Refs: [25] 36
Figure 2-7. PL results from aliquots collected during the cation exchange reaction of PbS/CdS QDs. (a) shows shell growth rate decreased after 5 minutes, and (b) shows the shell thickness seemed to be saturated after 24 hr. 38
Figure 2-8. QY of PbS and PbS/CdS QDs depending on the reaction time 39
Figure 2-9. Spectral shifts of air-exposed (a) PbS core-only QDs and (b) PbS/CdS core/shell QDs. Emission peak of PbS core-only QDs shows blue shift after air-exposures, while that of PbS/CdS core/shell QDs remains same. 40
Figure 2-10. Time-resolved PL (tPL) results for PbS core-only (red) and PbS/CdS core/shell QDs (black) measured on glass substrates. 41

Figure 2-11. (a) Atomic composition of PbS/CdS QDs measured by WDS. (b) Calculated radial distribution of PbS/CdS. 43
Figure 2-12. Tissue transmission in NIR and SWIR. Image reproduced from [34]....44
Figure 2-13. Still images captured from the fluorescent deep-tissue imaging video of an awaken mouse to which 1630 nm emitting PbS/CdS QDs were injected....45
Figure 2-14. Images of brain vasculature through the skull of an anesthetized mouse in the SWIR (a) with 1250-long-pass (LP) filter and (b) 1500-nm LP filter. 46
Figure 2-15. Conductivity of QD thin films made with 1,2-ethanedithiol (EDT)-treated PbS core-only QDs and PbS/CdS core/shell QDs. 49
Figure 2-16. Emission of Pbs and PbS/CdS QDs with different reaction conditions. An extra emission peak is observed when cation exchange was performed at lower temperature (80 °C) or for a short time (less than 5 min). The QDs colored in green is PbS/CdS QDs with 2 MLs of CdS. Therefore, we speculate that the shoulder peaks near 1400 nm (arrow) are from PbS/CdS QDs with 1 ML of CdS. 50
Figure 2-17. (a) When cation exchange of PbS QDs is performed at a lower temperature (60 °C), single emission peak is observed at higher wavelength than PbS/CdS with 2 MLs of CdS shell (red). (b) Emission of PbS/CdS QDs that are cation exchanged with different Cd-precursors – Cd-TDPA and $Cd(OA)_2$. 51
Figure 2-18. QY measurements show that QDs with a monolayer shell have a QY that is comparable to that of the other thicker shell QDs. 52
Figure 2-19. Schematic diagram of the 'type-IV' QD-LED structure used for this study. ...53
Figure 2-20. Average EQE at near 1300 nm *vs.* current density of IR QD-LEDs with PbS/CdS core/shell QDs and PbS core-only. The EQE of devices depends on current density (as known as efficiency droop) and the highest EQE value is referred as peak-EQE. 54
Figure 2-21. Average peak EQEs for all devices and the champion device with PbS core-only QDs and thin-shell and thick shell (highest QY) PbS/CdS QDs. Blue bars represent the average of the peak-EQEs from devices on all chips, and red bars

represent the average among the devices on the best-performing chip (1 chip contains 10 devices). 54
Figure 2-22. Peak EQE progression of visible and IR QD-LED performance over time. Image adopted from Refs: [32,33] 55
Figure 2-23. Average peak EQE and relative *in situ* PL intensity of QDs with different shell thickness. 56
Figure 2-24. PL decay curves for PbS core-only (red) and PbS/CdS core/shell QDs (black) (a) on the glass substrates and (b) with CTLs (*in situ*). 57
Figure 3-1. Dielectric constant (ε') and dielectric loss (ε'') *vs.* frequency showing frequency dependence of polarization mechanism. Image taken from Ref: [77] 61
Figure 3-2. (a) Typical C-V measurement scheme for a MIM capacitor, (b) an equivalent circuit model with both contact resistance (R_s) and leakage currents (R_p), (c) a simplified equivalent circuit when R_p is dominant and (d) when R_s is dominant. 63
Figure 3-3. Schematic diagram of Nyquist plots for each corresponding equivalent circuit model. (a) C_p model, (b) C_s model, and (c) model considering both R_p and R_s. 64
Figure 3-4. Capacitance *vs.* frequency sweep measurement at 0 V with 20 mV modulation results illustrated by Nyquist plots for (a) EDT-treated PbS QD thin films and (b) PbS QD thin films with native OA ligands. 65
Figure 3-5. Results of Mott-Schottky analysis for thin films of (a) PbS core-only QDs and PbS/CdS QDs with a thin ML CdS shell layer and (b) with a thick CdS shell layer used in Chapter 2. 68
Figure 3-6. (a) Carrier concentration from Mott-Schottky analysis and (b) extracted mobility combining with conductivity measurements for PbS core-only and PbS/CdS core/shell QDs used in Chapter 2. 69
Figure 3-7. Schematic diagram showing trap response at <x> to the AC modulation. Image adopted from Ref: [79] 71
Figure 3-8. Schematic illustration of the description of applying bias. DC bias and AC amplitude must be adjusted together to keep the position <x> same throughout the DLCP measurement. Image reproduced from: [79] 72

Figure 3-9. Results of DLCP measurement: Raw data (point) and quadratic fitting (line) to extract coefficient C_0 and C_1. Each color represents different measurement frequencies. 72
Figure 3-10. Density of drive-level states (N_{DL}) *vs.* frequency for BDT treated PbS QDs before and after oxidation by annealing at 80 °C in air. 75
Figure 3-11. Energy of trap states in BDT-treated PbS QD thin films before and after oxidation. 76
Figure 4-1. PL from PbS QD thin films with different ligands – OA (black), TBAI (green), EDT (blue), MPA (orange), and nBA (red) 80
Figure 4-2. XPS on the Pb 4f feature for PbS QD thin films with different ligands – OA (black), TBAI (green), EDT (blue), MPA (orange), and nBA (red). The binding energies of metallic Pb, Pb-S, and COO:Pb are highlighted. 81
Figure 4-3. The deconvoluted spectrum of PbS QD thin films with native OA ligands. The spectrum is well fitted with the sum of the peaks from Pb-S and Pb-carboxylates.[105] 82
Figure 4-4. The XPS results of PbS QD thin films with different length of dithiol ligands are compared with oleic acid (OA) ligand : 1,2-ethanedithiol (EDT), 1,4-butanedithiol(BuDT), 1,8-octanedithiol(ODT), and 1,3-benzendithiol (BDT). Under-charged Pb atoms exist regardless of the length of dithiol ligands. 82
Figure 4-5. XPS results show the under-charged Pb atoms in TBAI-treated PbS QDs result from four different synthetic batches of Hines method and Cl-synthesis. 83
Figure 4-6. XPS measurements of ligand-exchanged PbS QD thin films following oxidation with BQ – OA (black), TBAI (green), EDT (blue), MPA (orange), and nBA (red). The binding energies of Pb-S are highlighted. 84
Figure 4-7. PL measurements of ligand-exchanged PbS QD thin films following oxidation with BQ– OA (black), TBAI (green), EDT (blue), MPA (orange), and nBA (red). 84
Figure 4-8. (a) The XPS results of TBAI-treated PbS QD thin films with different oxidation methods: TBAI-treated films as a reference (black), TBAI-treated films followed by 0.8 % (v/v) pyruvic acid treatment[91] (blue), which is a well-known oxidant in metabolic pathways in muscles,[106] TBAI-treated films followed by annealing at 80°C

in air for 30min (red). Under-charged Pb features at the shoulder of Pb-S peak are disappeared with pyruvic acid treatment and air-annealing. (b) The PL shows that the emission from sub-bandgap states removed after the treatment.....85
Figure 4-9. XPS results of TBAI-treated samples with and without 1,4-hydroquinone (HQ) treatment. HQ is a product from the reduction of BQ. Minimal change in the spectral features of (a) Pb 4f and (b) O 1s is observed before and after the HQ treatment. This result indicates limited binding of HQ on the QD surface. O-to-Pb ratio with background correction increases 9% after the HQ treatment. We suspect that oxygen in the samples is originated from residual OA ligands or air-exposures during the sample transfer to XPS chamber.....87
Figure 4-10. The truncated octahedron shape of the model PbS QD used for the DFT calculations.....89
Figure 4-11. Bader charge analysis gives the charge distribution for each element—Pb (blue), S(red) and I (green).....90
Figure 4-12. The simulated charge distribution of different Pb-to-S ratio samples to show that the level of charge threshold for under-charged Pb species is 0.8.....90
Figure 4-13. (a) The DoS (total, black) from DFT, broken into PDoS for each chemical species—S (orange), I (purple), all Pb (blue). The PDoS of Pb further subdivided—contributions from under-charged Pb atoms (<0.8, red), and Pb atoms with a charge greater than 0.8 (green). (b) An enlarged view of (a) highlighting the DoS near the band gap.....91
Figure 4-14. The DFT results shows that under-charged Pb species are located on the (111) facet, and induce sub-bandgap states.....92
Figure 4-15. (a) DoS and (b) Bader analysis for the comparison of bare QDs and iodine passivated QDs. I^- ligands suppress under-charged Pb species, and sub-bandgap states in off-stoichiometric PbS QDs. As a reference, calculations on stoichiometric QDs show no sub-bandgap states and no reduced Pb atoms.....94
Figure 4-16. DFT results show that I^- and fluoride (F^-) ligands induce different suppression of under-charged Pb species and a different profile of sub-bandgap states.....95

Figure 4-17. A schematic of the Schottky diodes used for the DLCP measurements.....97
Figure 4-18. DLCP measurement of the density of states of EDT-treated PbS films with and without the BQ treatment. The low frequency regime (red box) includes contributions from carriers interacting with conductive and trap states, while the high frequency regime (green box) gives the density of conductive states only.....97
Figure A-1. (a) Space filling factor, ρ *vs.* radius ration between two spheres, γ showing the criteria for various binary ordered structures. Image adopted from Refs:[114,122,123] (b) Calculated phase diagram at γ=0.558 showing possible phases. Image adopted from Refs:[119].....105
Figure A-2. AB_2 structure illustrating with (a) space filling model, (b) ball-and-stick model, and (c) (001) projection. Same illustration for *ico*-AB_{13} structure (d), (e), and (f) and for *cub*-AB_{13} structure (g), (h), and (i). Images adopted from Refs: [123–125].....106
Figure A-3. Schematic diagram for BNSL preparation steps: Two different QDs are dissolved in TCE. The solution is slowly dried in tilted vial under controlled environments to deposit BNSL films on substrates.....106
Figure A-4. (a) High-resolution (HR) TEM image and (b) false color image of *cub*-AB_{13} structure deposited on TEM grid. (c) Dark-field scanning transmission electron microscopy (DF-STEM) image and (d) (100) view of *cub*-AB_{13} structure, image taken from Refs:[114].....108
Figure A-5. SEM image of *cub*-AB_{13} BNSL thin films on (a) Si substrates and (b) and (c) on SiO_2 substrates. (d) Fluorescent optical microscopy images taken with 595 nm ± 25 nm band-pass filter.....109
Figure A-6. Optical characterization showing (a) energy donation from C-QDs and (b) energy acceptance by P-QDs. (c) tPL demonstrating a rising time at the beginning by FRET.....110
Figure A-7. Schematic illustration for a structure of BNSL LEDs.....111
Figure A-8. Electrical characterization of BNSL-LEDs. (a) J-V, (b) EQE, and (c) electroluminescence (EL) spectra.....112

List of Tables

Table 1-1. Representative combinations of precursors and solvent/surfactant for PbS QD synthesis. 20

Table 2-1. Typical reaction conditions used for PbS QD synthesis. For S-precursors, 3.15 mL of $(TMS)_2S$ in 150 mL of ODE solution is used for all the reactions..... 34

Table 4-1. The atomic ratios of PbS QDs used in this work. Experimental data for the Pb-to-S ratio is obtained using WDS, and the I-to-Pb in TBAI-treated PbS QD thin films is measured using XPS. The ratios for the simulated QD used in DFT calculations is included for comparison..... 86

Chapter 1.

Introduction

Quantum Dots and Their Application in Optoelectronics

1.1 Quantum Confinement System

When the size of materials approaches to the magnitude of electron wave function, the properties of the materials deviate significantly from those of bulk materials. For instance, in semiconductor nanocrystals (NCs), known as quantum dots (QDs), three-dimensional quantum confinement of excitons leads to their size-dependent electronic and optical properties.[1] When the size of semiconductors becomes comparable to or smaller than their exciton Bohr radius[a], the electronic structure is modified to confine wave function of electrons and holes inside the system. The exciton Bohr radii of lead chalcogenides materials are 20 nm for lead sulfide (PbS), 46 nm for lead selenide (PbSe), and 104 nm for lead telluride (PbTe).[2,3] As a consequence, the electronic structure for a quantum confined QD system is perturbed from its bulk structure. For instance, energies of electron-hole pair

[a] $a_B = \varepsilon \frac{m_0}{m^*} a_0$, where a_B is the exciton Bohr radius, ε is the dielectric constant of the material, m_0 is the rest mass of electron, m^* is reduced mass of exciton or electron-hole pair, and a_0 is the Bohr radius of hydrogen atom

(ehp) states is calculated in a particle-in-a-sphere model with effective mass approximation as described in Equation 1.1.[4]

$$E_{ehp}(n_h L_h n_e L_e) = E_g + \frac{\hbar^2}{2a^2}\left\{\frac{\alpha^2_{n_h,L_h}}{m^v_{eff}} + \frac{\alpha^2_{n_e,L_e}}{m^c_{eff}}\right\} - E_c \quad \text{(Equation 1.1)}$$

In this equation, E_g is the band gap energy of bulk semiconductors, a is radius, n_h, L_h, n_e, and L_e are quantum numbers for holes and electrons, $\alpha_{n,l}$ is the n-th zero of l-th order spherical Besel function, $m^v{}_{eff}$ is effective mass for holes in valence band, $m^c{}_{eff}$ is effective mass for electrons in conduction band, and E_c is the first-order Coulomb correction term[b].

1.2 Lead Sulfide QDs

PbS is a compound semiconductor having a rock-salt crystal structure (space group: $Fm\bar{3}m$, No.225) with a lattice parameter of 5.934 Å.[5] Bulk PbS has a band gap energy (E_g) of 0.29 eV at the L point,[6,7] and its effective mass for electrons and holes are 0.087 m_0 and 0.083 m_0, respectively.[8]

Colloidal PbS QDs have been studied intensively in optoelectronic application because of their following properties: First, PbS QDs have a wide range of the tunable band gap energy from 0.6 eV to 1.8 eV,[9–12] which covers the ideal band gap energy for single- or multi-junction photovoltaics, the short-wavelength infrared (SWIR)[c] window for optical

---

[b] $E_c = 1.8\frac{e^2}{\varepsilon a}$, where e is a unit electron charge, a is the radius of a particle, and ε is dielectric constant

[c] The definition of near-infrared (NIR) and SWIR in this thesis are based on the response of various detectors: [126]
- NIR: from 0.7 to 1.0 μm (from the approximate end of response of the human eye to that of silicon)
- SWIR: from 1.0 to 3.0 μm (from the cut-off of silicon to that of the mid-wavelength IR atmospheric window)

communications and deep-tissue bio-imaging (Figure 1-1). Second, they have relative high quantum yield (QY) in SWIR range longer than 1000 nm in wavelength compared to organic fluorophores.[13–16] Lastly, colloidal-synthesized PbS QDs have great potential to mass-production because they are composed of earth-abundant elements, eligible for large-scale synthesis, compatible with conventional semiconductor fabrication technology and promising to a large-area solution process such as roll-to-roll, ink-jet and spray casting.

Colloidal PbS QDs are synthesized in solution using a hot-injection method.[12,17–19] The reaction is carried out with a high boiling point solvent at temperature between 50 °C and 200 °C under inert atmosphere. In general, the reaction solution contains lead (Pb) and sulfur (S) precursors, surfactants and ligands. Both surfactants and ligands control reaction kinetics, and provide the oleophilic moieties for solubility by binding to the QD surfaces. Fatty amines or fatty acids such as carboxylic acid or phosphonic acids are commonly used for ligands. A typical experimental set-up for the colloidal PbS QD synthesis is shown in Figure 1-2. All procedures are performed under inert atmosphere to avoid oxidation of PbS QDs and the impurity effect from moisture.[20,21] For instance, preparation of the precursor solutions, hot injection of the precursors, and purification of the QD products are performed in a nitrogen filled glovebox or using Schlenk line techniques (Figure 1-2). Commonly used combinations of precursors and solvent/surfactant for PbS QD synthesis are summarized in Table 1-1. The size of QDs is controlled by reaction temperature, reaction time, precursor ratio, and ligand chemistry (different combinations or concentrations of ligands). To produce mono-disperse QDs, intense efforts for developing reaction conditions and precursors have been made to maintain the narrow size distribution during the growth. The detailed procedures for PbS QD synthesis will be described in Chapter 2.

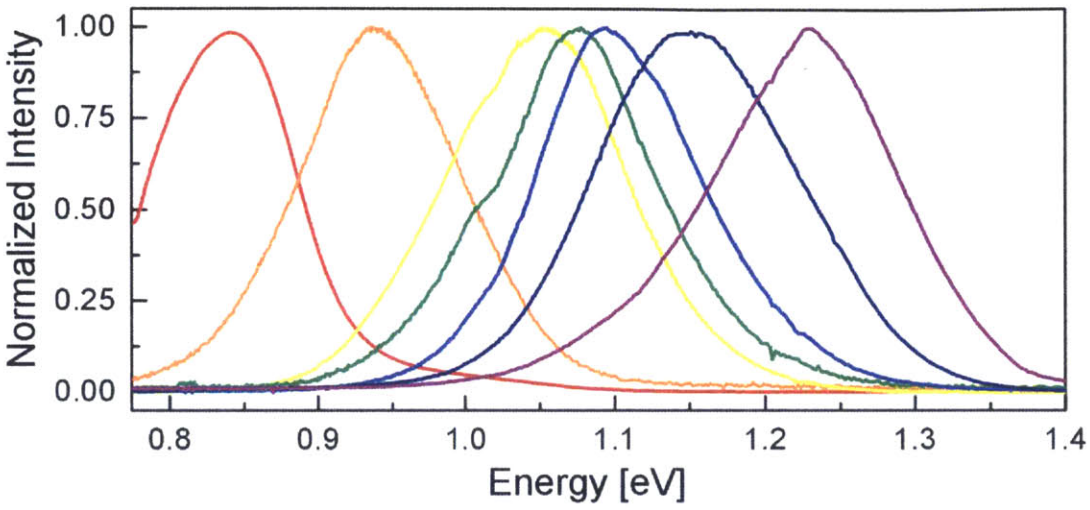

Figure 1-1. Emission from different sizes of PbS QDs shows the wide range of band gap tunability.

Table 1-1. Representative combinations of precursors and solvent/surfactant for PbS QD synthesis.

Pb precursors	S precursors	Solvent/Surfactant	Refs
lead (II) oleate ($Pb(OA)_2$) via PbO or lead (II) acetate	hexamethyldisilathiane (as known as bis(trimethylsilyl)sulfide $(TMS)_2S$))	1-octadecene (ODE) /oleic acid (OA)	[12]
$PbCl_2$	elemental S	Oleylamine (OAm)	[17,22]
$PbCl_2$	elemental S	OAm / tri-n-phosphine (TOP)	[23]
lead halide (PbX_2, X = Cl, Br, and I)	$(TMS)_2S$	OAm	[18]
$Pb(OA)_2$ via lead (II) acetate	Na_2S / thiourea / thioacetamide	n-decane/OA	[24]
$Pb(OA)_2$ (purifed[d])	Thiourea	ODE / OA	[19]

[d] They used purified oleic acid to avoid involving H_2O in the reactions.

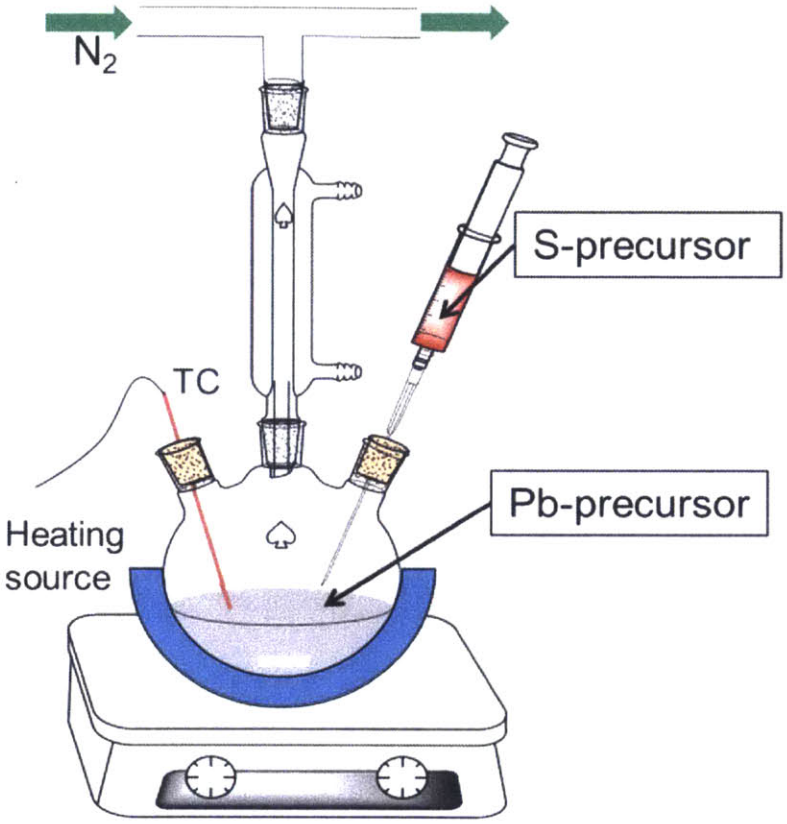

Figure 1-2. A typical experimental set-up using Schlenk line for synthesis of colloidal PbS QDs. The image is adopted from Refs: [25]

1.3 Applications of Colloidal PbS QDs

In addition to fundamental study of PbS QDs, interests in their application to optoelectronics and biology have grown. Among various applications, colloidal PbS QDs have been researched intensively for active layers (or absorbing layers) in photovoltaics during past decades. The tunable range of band gap energy (E_g) covering the ideal value for solar cells

towards Shockley-Queisser limit[e], their potential to low-cost solution-based fabrication,[26] and possibility of efficient carrier multiplication (CM)[f,27] make PbS QDs attractive materials for photovoltaics. And the tunable band gap gives opportunity to multi-junction solar cells by satisfying the ideal combination of band gaps for higher ideal efficiency—44 % for double junction and 49 % triple junction.[28]

Applications in a photodetector are another field using their light-absorbing property. PbS QDs are considered as promising candidates for IR-photon detecting materials used for optical communication and night vision applications due to their band gap range covering IR window of atmosphere. In addition to their optical properties, their process compatibility with Si integration technology and low-cost solution techniques provides distinct advantages over current technology based on III-V semiconductors such as InAs and $In_{1-x}Ga_xAs$.[29] In addition, their high photoluminescence (PL) QY gives another photon detection opportunity with combination of Si technology. Down-conversion dual band detectors increase responsivity of UV range using PbS QDs by down-converting UV lights to more efficient detecting range of Si detectors.[30]

Furthermore, as an NIR or SWIR emitting light source, colloidal PbS QDs are low-cost alternatives for single crystalline inorganic semiconductors, which require expensive high temperature growth process. In contrast to the visible regime, organic dyes cannot be a good alternative any longer, because their poor QY in the IR regime longer than 1000 nm in wavelength.[13–16] Thus, PbS QDs have been researched for the application in IR light emitting diodes (LEDs)[31–33] and deep-tissue imaging in biology.[25,34,35]

---

[e]Ideally, power conversion efficiency (PCE) is achievable up to 33.7 % assuming a single p-n junction solar cell with a band gap of 1.34 eV under AM 1.5 solar spectrum.[127]

[f] The degree of CM in QDs is controversial. G. Nair and his coworkers reported that the CM in QDs is not as strong as previous results, and they discussed thoroughly about experimental results and their mechanism.[128]

1.4 Trap States

In semiconductors, sub-bandgap states, referred as trap states, are localized electron states inside band gap caused by material imperfections. Trap states are categorized into two states depending on their energy levels: shallow-level states, known as doping states, and deep-level states. Doping states have energy levels of a few tens of meV from the valance or conduction band and are intentionally introduced by dopants[g] to control electrical properties of semiconductors. Deep-level traps are undesirable states located deeper in energy and directly interfere with the operation of semiconductor devices by providing intermediate states to facilitate the recombination of holes and electrons and leakage current sources. The well-known origins of deep-level trap states are surface states, most of impurities, and crystallographic defects in lattice such as dislocations, stacking faults, vacancies, or interstitials. Hereinafter, only deep-level states are referred as trap states.

Trap states, especially surface states, are also problematic in QDs.[36–38] Because of a large surface-to-volume ratio, surface trap states in QDs have great influence on electrical and optical properties of QDs.[39] Surface states are thought to be participated in Auger ionization process, broadening of emission peak width, shortening of the exciton lifetime, and decreasing of QY. As a recombination center, for instance, trap states in QDs provide a fast non-radiative decay pathway and yield a decrease of QY[h] and exciton lifetime.

Trap states are very effective in enhancing the generation and recombination rates in a semiconductor. Trap-assisted generation and recombination process, described in Shockley-

---

[g] An important difference to other impurities is that dopants are foreign atoms that are fairly similar to those of the host semiconductors, which create states very close to the band edges.

[h] PL QY is described as: [129]

$$\mathrm{QY} = \frac{\#\ of\ emitted\ photons}{\#\ of absorbed\ photons} \propto \frac{k_r}{k_r + k_{nr}}$$

where k_r is a rate constant of radiative decay and k_{nr} is a rate constant of non-radiative decay.

Read-Hall (SRH) model, is the most pervasive generation and recombination mechanisms in semiconductor devices. Figure 1-3 schematically illustrates the each capture and emission process of electrons and holes in SRH model. For the generation and recombination of carriers, through intermediate trap states, instead of requiring a single event with energy larger than the band gap, two separate capture and emission events with substantially less energy are sequentially needed. As a consequence, the trap-assisted generation and recombination exhibit much faster rates than band-to-band generation and recombination. Additionally, trap states help to satisfy the momentum requirements of the transitions. Trap-assisted recombination shortens the carrier lifetime and diffusion length, which strongly influence the behavior of microelectronic devices as well as the performance of QD-optoelectronic devices such as LEDs, photodetectors, and photovoltaics.

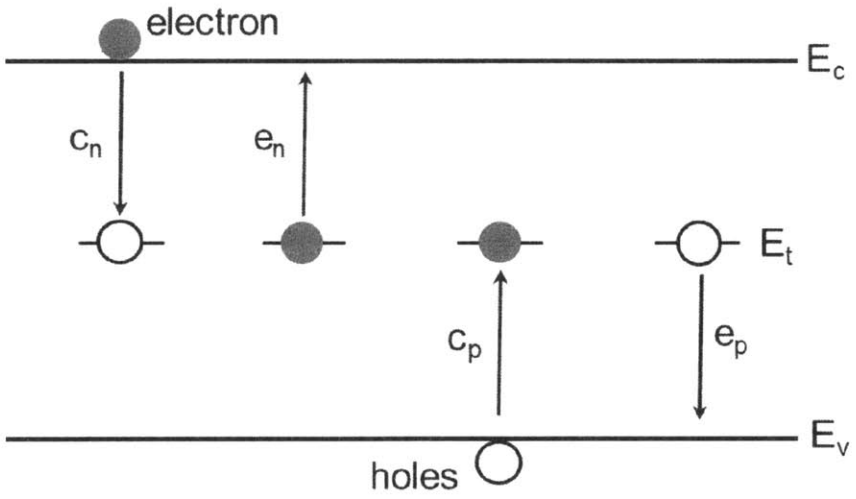

Figure 1-3. Schematic diagram of trap-assisted process—electron capture (c_n), electron emission (e_n), hole capture (c_p), and hole emission (e_p).

1.5 Thesis Overview

This thesis focuses on reducing trap states by passivating surface dangling bonds and by eliminating their chemical origins. The approaches are evaluated by showing the improvement of device performance and characterizing QD thin films directly using capacitance-based measurement techniques.

Chapter 2 first gives an overview of PbS QD synthesis and then explains the growth of CdS as an inorganic shell layers. The surface states of PbS are passivated by CdS shell layers, and the improvements are demonstrated by optical characterizations and performance evaluation in optical and electrical applications.

Chapter 3 presents capacitance-based characterization techniques for QD thin films as complementary methods to conventional current-based measurements. These techniques provide reliable information for the density of carriers and enable analyzing trap states in QD thin films.

Chapter 4 describes identification of the chemical origin of trap states using the combination of chemical analysis using X-ray photoelectron spectroscopy (XPS) and theoretical studies using density functional theory. This chemical origin is directly managed by chemical treatments, which leads a rationale for control of trap states.

Chapter 5 summarizes the findings made from this thesis work and briefs the future work that can be done to further understanding of the trap states in QD thin films.

Additionally, Appendix A demonstrates a possibility for designing a novel type of active layer in QD-LEDs using Förster resonance energy transfer (FRET) in self-assembly binary NCs superlattices (BNSLs).

Chapter 2.

PbS/CdS Core/Shell QDs

Synthesis and their characterization for applications

In past decades, PbS QDs have been explored in opto-electric applications because of the following properties of QDs: a high absorption coefficient, a high QY, a tunable band gap, and compatibility with low-cost solution processing.[26,40–43] In particular, PbS QDs shows great potentials to applications in IR optoelectronics such as photovoltaics, photodetectors, and LEDs. However, current QD devices show inferior performance compared to conventional bulk semiconductor devices.[43–45] This is mainly due to a high density of surface traps, insufficient stability of QDs, and low conductivity of QD thin films. Inorganic shells can passivate the dangling bonds of the core surface, which are thought to be a major source of surface traps and provide both chemical and physical protection of the QD cores from degradation by environmental exposures. In addition, inorganic shells will allow harsh chemical treatment such as ligand exchange.[46–48] Therefore, core/shell QDs with PbS cores are synthesized and characterized to adopt into QD devices. Our study shows that core/shell QDs yield an improved the QY and stability of QDs but it decreases the conductivity of QD thin films due to the hopping barrier. The low conductivity of core/shell QD thin films is mitigated by synthesizing core/shell QDs with a monolayer of shell.

2.1 Material System

The shell materials in core/shell QDs need to satisfy several conditions. First, shell materials need to have good lattice compatibility with the cores to passivate surface dangling bonds on the core with suppressing additional defect formation.[49] In order to suppress interfacial defects between cores and shell materials, shell materials that can be grown epitaxially on the core materials are preferred.[50] The criteria of epitaxial growth are minimal mismatch of lattice parameters and the same crystal structure of the core and the shell. For a very thin shell layer, epitaxial growth requirements for shell materials are less strict; the lattice constraint at the interface helps them grow epitaxially even if they have a different crystal structure from the cores at the standard ambient temperature and pressure (SATP).[i,50] However, beyond a critical thickness, which is determined by thermodynamics—competition between phase change energy and interfacial energy, the shell materials' thermodynamically stable structure evolves and strain is released by defect formations such as interfacial dislocations.[50,51] Another consideration for the shell materials is the band alignment of the core- and the shell-materials. The band alignment strongly influences charge separation and transport process. For instance, carriers (both electrons and holes) are mainly confined in the core in the case of type-I heterojunction QDs, and therefore, type-I QDs exhibit high excition recombination rates. In contrast, carriers are more separated in type-II heterojunction QDs and type-II QDs exhibit relatively low exciton recombination rates (Figure 2- 1).[49]

[i] Standard ambient temperature and pressure is defined as a temperature of 298.15 K (25 °C, 77 °F) and an absolute pressure of exactly 100 kPa (14.504 psi, 0.987 atm) by National Bureau of Standards.[130]

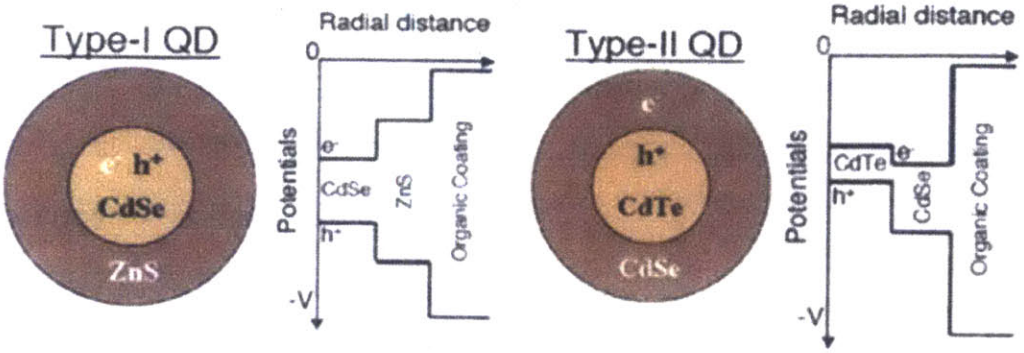

Figure 2-1. Schematic diagram of band alignment for the type-I (CdSe/ZnS) (left) and type–II (CdTe/CdSe) (right) heterojunction QDs, figure taken from Ref: [52]

As a partner for PbS cores, CdS is selected as a shell material because they share S ions and have a small lattice mismatch of 1.7 %.[53] In SATP condition, thermodynamic equilibrium phase is a rock-salt structure for PbS and a zincblende structure for CdS, and also a meta-stable wurtzite phase and a high-pressure rock-salt structure are known for CdS. Both zincblende and rock-salt structures have a common face-centered cubic (FCC) structure of S ion. The difference between two structures is a location of cations: at the octahedral interstitial sites of S ions in the rock-salt structures, and at the tetrahedral interstitial sites in the zincblende structures. The common array of FCC-structured S ions is thought to satisfy the interfacial continuity for the shell formation. In addition, rock-salt CdS shell is expected on the PbS cores by lattice constraint at the interface in case of very thin shell layers. The rock-salt CdS is reported under high pressure,[54] which means that rock-salt phase of CdS has tolerable energy difference from wurtzite or zincblende especially under interfacial strains. Inferring the band alignment at the PbS/CdS interface is intricate. Their junction is expected to be a type-I heterojuction based on the bulk properties such as E_g and electron affinity. However, there is a report on the formation of a type-II heterojunction in an alternating super-lattice thin film structure due to the lattice constraint.[55] According to this result, the junction between PbS and CdS would be more likely to be a type-II

heterojunction rather than a type-I heterojunction, when a thin CdS shell layer is grown epitaxially with the rock-salt structure on the PbS cores. In addition, the PbS/CdS system has other advantageous characteristics such as negligible solubility of the metal ions in each other. Figure 2-2 shows the vertical section of the ternary phase diagram of the Pb-Cd-S system.[56,57] At 300 °C, the solubility of Cd in PbS is less than 2 atomic % (at.%), and therefore, intermixing of Cd and Pb under the shell growth condition (80–120 °C) is expected to be negligible.

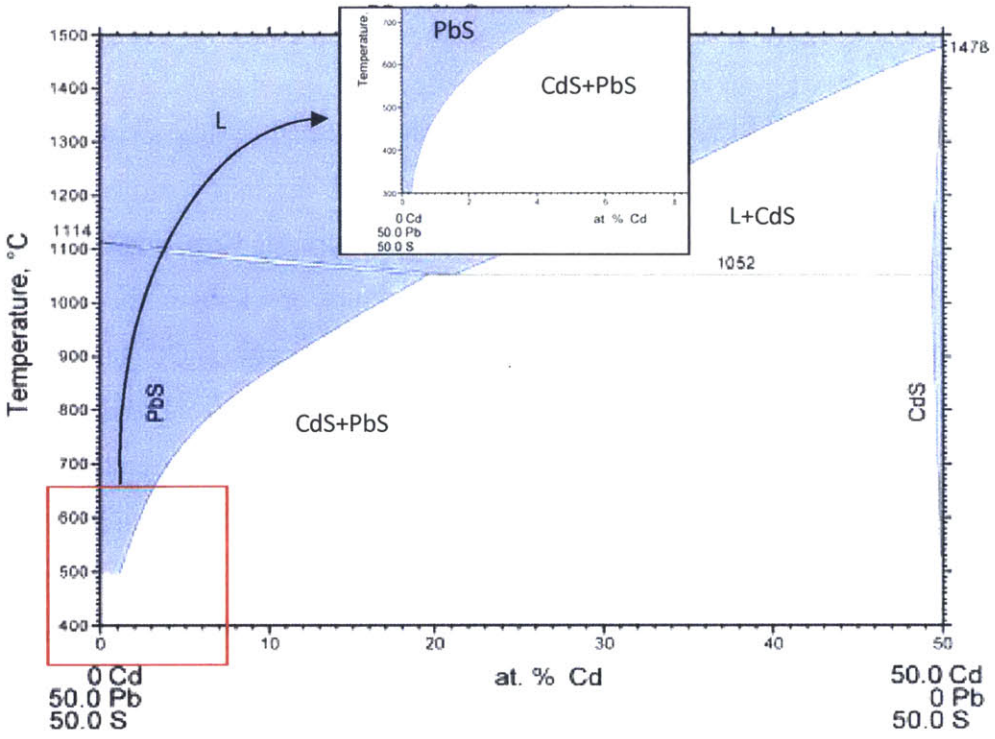

Figure 2-2. Vertical section at 50 at.% S of the Pb-Cd-S ternary phase diagram, images taken from Refs: [56] and [57].

2.2 Synthesis

2.2.1 PbS Core Synthesis

The synthesis of QDs requires controllability of size of nanoparticles, while maintaining a narrow size distribution. The strategy to maintain a narrow size distribution is using reaction kinetics with nucleation and growth mechanism suggested by LaMer *et al.*[58] Figure 2-3 shows the typical time line of QD synthesis,[58,59] and it shows the Ostwald ripening followed by the nucleation and the growth stage. The Ostwald ripening starts when precursors are depleted. The thermodynamic driving force for the Ostwald ripening can be explained by the Gibbs-Thomson equation (Equation 2.1).[51] As described in the Equation 2.1, the additional Gibbs free energy (ΔG_γ) due to interfaces is proportional to the curvature (= 1/r). Thus, larger dots tend to have lower Gibbs free energy than smaller dots, and it eventually drives the Ostwald ripening. Lifshitz, Slyozov and Wagner developed a model (known as the LSW theory) predicting the ripening kinetics and the particle size distribution function under the dilute condition assuming the zero volume fraction of coarsening phase, which limit the validity of LSW theory (Equation 2.2).[60] More realistic models were proposed to explain the phenomena, however, a fully satisfactory approach has not yet been found.[60] The Ostwald ripening broadens the size distribution of QDs, hence PbS QDs synthesis procedures should be designed to avoid the Ostwald ripening.

$$\Delta G_\gamma = \frac{2\gamma\Omega}{r} \qquad \text{(Equation 2.1)}$$

where ΔG_γ is increase of Gibbs free energy, γ is surface energy, Ω is molar volume, and r is radius of particles.

$$\bar{r}^3(t) - \bar{r}^3(0) = \frac{8\gamma c_\infty \Omega^2 D}{9RT} t \qquad \text{(Equation 2.2)}$$

where $\bar{r}(t)$ is average radius of all particles as a function of time, t is time, γ is surface energy, c_∞ is solubility of particle materials, Ω is molar volume, D is diffusion coefficient of particle materials, R is ideal gas constant, and T is temperature (in K).

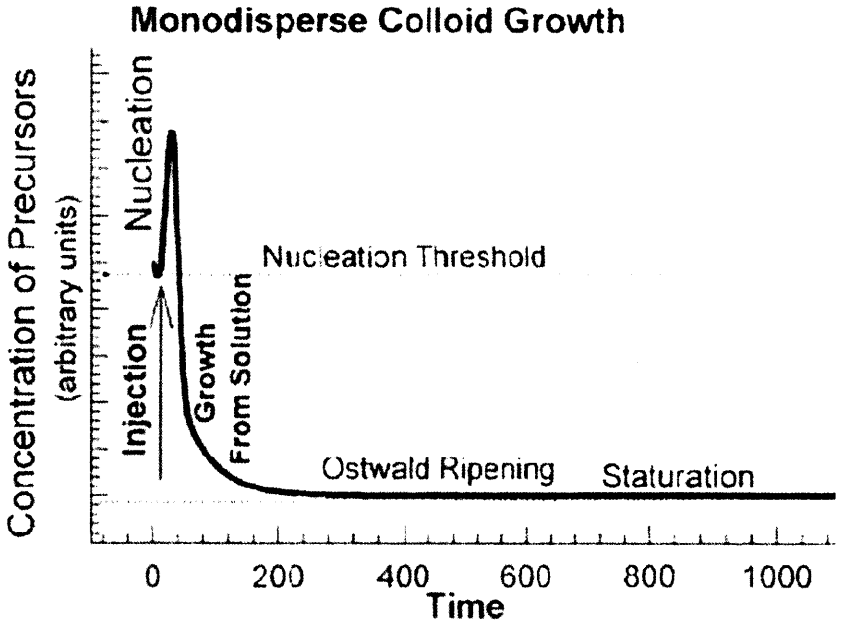

Figure 2-3. Schematic diagram demonstrating the stages of nucleation and growth for the QDs in the framework of the LaMer model. Image is taken from Refs: [59]

PbS QDs are commonly synthesized using several different precursors as mentioned in Table 1-1. Those methods are categorized into two representative methods by Pb precursors, and their modifications: 1) $Pb(OA)_2$-based (referred to as Hines method) and 2) $PbCl_2$-based synthesis route.

Hines method uses $Pb(OA)_2$ as a Pb-precursor, $(TMS)_2S$ as a S-precursor, OA as a surfactant and ODE as a solvent. The temperature ranges for the synthesis is between 90 and 150 °C depending on the target size of QDs. The size of QDs is mainly determined by concentration of surfactant and the reaction temperature. One of the advantages of this method is scalability, because the final size of QDs is determined mainly by initial conditions such as growth temperature, surfactant concentration. And this method offers

synthesizing small PbS QDs in the range of 1st absorption peak from 500 nm to 1700 nm,[9–12] which covers the ideal band gap for solar cells. Recent researches show that residual H_2O while the preparation of $Pb(OA)_2$ have an important role to passivating surface dangling bonds,[20] however, the removal of this H_2O helps the precise control of QD synthesis kinetics.[19]

$PbCl_2$-route is another representative preparation method for synthesizing monodispersed PbS QDs.[17] The reaction condition of this method leads less nucleation events, and eventually, leads narrower size distribution. In addition, chloride (Cl^-)ions from the Pb-precursor passivate the surface effectively as a native ligand, which can provide better air-stability and QY.[23] However, synthesizing smaller size—bellow 1100 nm of 1st absorption peak (corresponding 3.6 nm in diameter, approximately)—is not achievable with this method,[17,18] which is critical for photovoltaic applications. Several modified methods are reported to improve size distribution, to extend synthesizable size range, and to limit Ostwald ripening.[17,22]

In this work, PbS QDs synthesized by the Hines method[12] are mainly used. As an example, 4-nm PbS QDs are prepared by following steps: For Pb-precursors, lead (II) acetate trihydrate ($Pb(CH_3CO_2)_2 \cdot 3H_2O$, 11.38 g) was dissolved in 150 mL of OA and 150 mL of ODE, and heated for 100 °C under vacuum using Schlenk line to remove by-product, H_2O. The solution was degassed for overnight with stirring. S-precursor solution was prepared by adding 3.15 mL of $(TMS)_2S$ into 150 mL of ODE in a nitrogen-filled glovebox. Before injection of the S-precursor solution, Pb-precursor solution was heated to 150 °C under nitrogen, and reaction was triggered by rapid injection of the S-precursor solution into Pb-precursor solution. Heating source was removed after a minute, and let the solution cool down itself. The cooled solution was transferred into the glovebox without air-exposure and purified by precipitation. Butanol and methanol were used to precipitation, and QDs were dissolved again in hexane after the separation by centrifugation. The conditions for different size of QDs are tabulated in Table 2-1. PbS QDs synthesized by other methods are used occasionally for the purpose of comparison in properties.

Table 2-1. Typical reaction conditions used for PbS QD synthesis. For S-precursors, 3.15 mL of $(TMS)_2S$ in 150 mL of ODE solution is used for all the reactions.

1st exciton peak (in nm, approximately)	Pb-precursor solution			Injection T (in °C)	Heating Duration (in sec)	Cooling method
	OA (in mL)	ODE (in mL)	$Pb(OAc)_2 \cdot 3H_2O$ (in g)			
950	21	300	11.38	120	0	water bath
1150	75	225	11.38	150	60	self-cooling
1350	150	150	11.38	150	60	self-cooling
1600	150	150	11.38	150	80	self-cooling
1750	200	100	11.38	150	0	self-cooling

2.2.2 PbS/CdS Core/Shell QD Synthesis

The formation of an inorganic shell material on the QD core is commonly achieved by three synthetic routes:[61,62] 1) injection method, 2) successive ion layer adsorption and reaction (SILAR), and 3) cation exchange. Injection method is conducted with the simultaneous injection of highly reactive positive and negative ion precursors at lower temperatures than that of the QD core synthesis, in order to prevent the nucleation of the shell materials instead of depositing on the cores. And SILAR is inspired by atomic layer deposition (ALD), which uses less reactive precursors. The SILAR method utilizes alternating injection of precursors followed by a high-temperature annealing step. The size of the cores remains the same during those two synthetic methods, and only the shell layer thickness grows. Cation exchange, an alternative method for shell formation, requires only a cation precursor to be added into the QD core solution. In this method, the shell layer grows into the cores, *i.e.*, the overall size of the QDs remains the same and the core shrinks, as shown in Figure 2-4 and Figure 2-5.

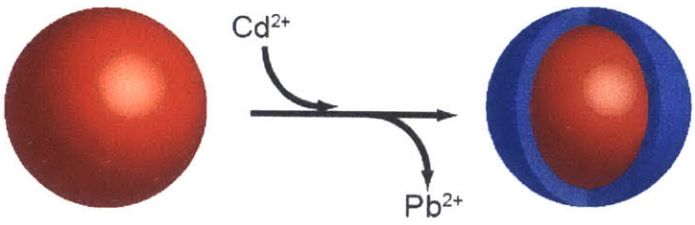

Figure 2-4. Schematic diagram of the cation exchange reaction.

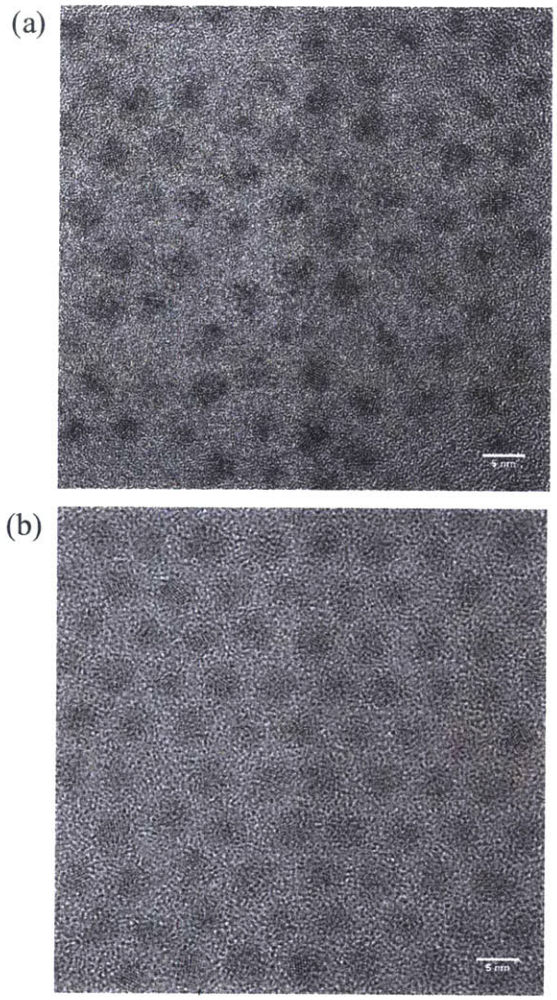

Figure 2-5. Transmission electron microscopy (TEM) images of (a) PbS core-only QDs and (b) PbS/CdS core/shell QDs

The CdS shell is not able to be grown directly on the PbS core surface so the cation exchange method, reported by the Klimov group,[62] is used for the CdS shell layer formation. The CdS shell layer on the PbS QD-cores are grown by following steps: 6 mL of toluene added to 5 mL of PbS QDs in hexane (75 mg/mL), and they were degassed and a pre-synthesized Cd-precursor solution, 12 mL of cadmium oleate ($Cd(OA)_2$) in diphenylether (0.33 M), was injected to the QD solution at 120 °C. The reaction is quenched by injecting excess amount of room-temperature hexane. The shell thickness is controlled by the growth time.

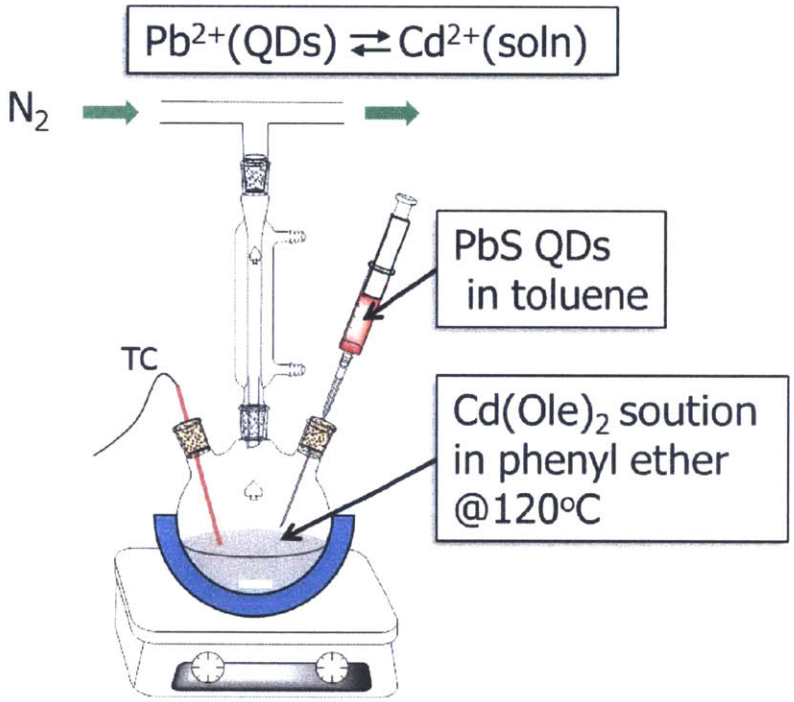

Figure 2-6. A typical experimental set-up using Schlenk line for cation exchange reaction with colloidal PbS QDs and Cd-precursors. The image is adopted from Refs: [25]

2.3 Characterization of PbS/CdS Core/Shell QDs

2.3.1 Optical Characterization

The PLs from aliquots are measured to observe a time-dependent shell growth. As shown in Figure 2-7 (a), the PL peak is blue-shifted, which indicates decreasing PbS core size. Since the size of the QDs does not change after reaction, we can conclude that CdS shell is grown towards the center *via* cation exchange and the shell thickness increases with time. Of note, the shell thickness seems to be saturated after 24 hr due to the depletion of Cd-precursor (Figure 2-7 (b)).

QY is a good measure for trap passivation. To confirm that the surface traps are passivated with inorganic CdS shell layer, the QY is directly measured with a 452 nm diode laser and integrating sphere. Figure 2-8 shows that the QY increases until 30 min, which corresponds to ~2.5 monolayers (MLs). The same trend is reported in CdSe/ZnS core/shell QDs that the QY increase is due to the surface passivation with a ZnS shell.[61] However, after a certain thickness, ~3 ML, the QY starts to decrease because the stress induced from lattice mismatch becomes larger with increasing shell thickness, and this stress acts as an energy source for defect formation.[61]

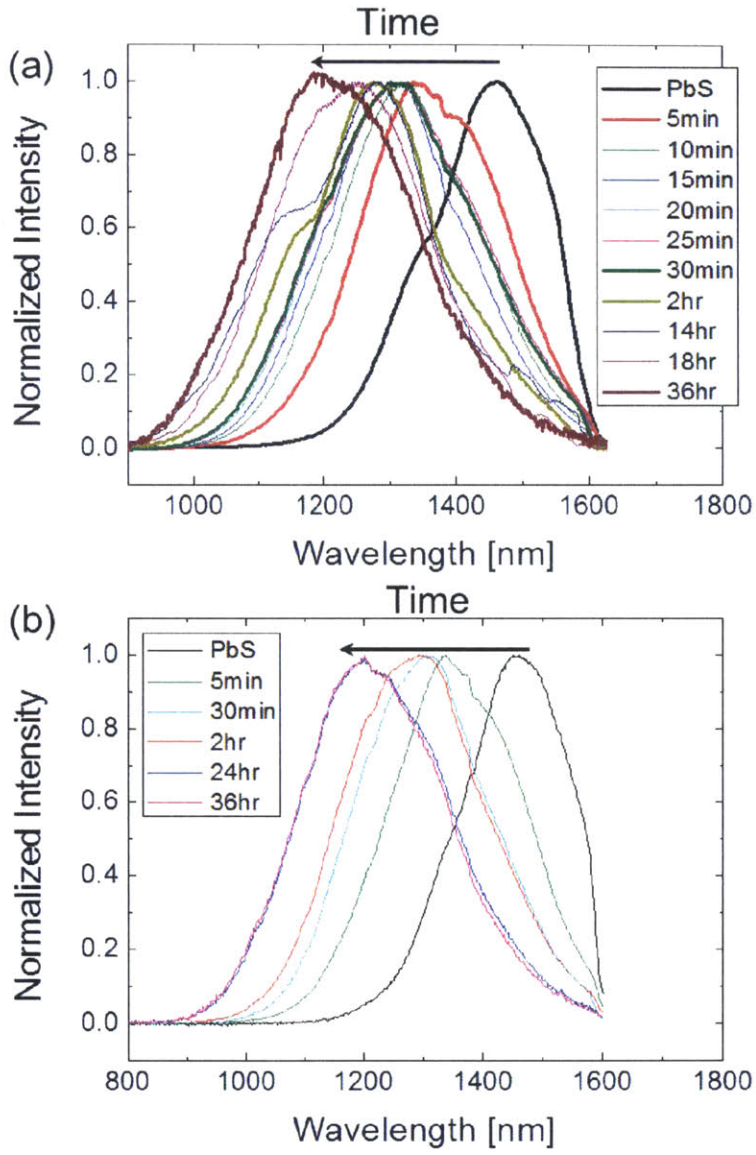

Figure 2-7. PL results from aliquots collected during the cation exchange reaction of PbS/CdS QDs. (a) shows shell growth rate decreased after 5 minutes, and (b) shows the shell thickness seemed to be saturated after 24 hr.

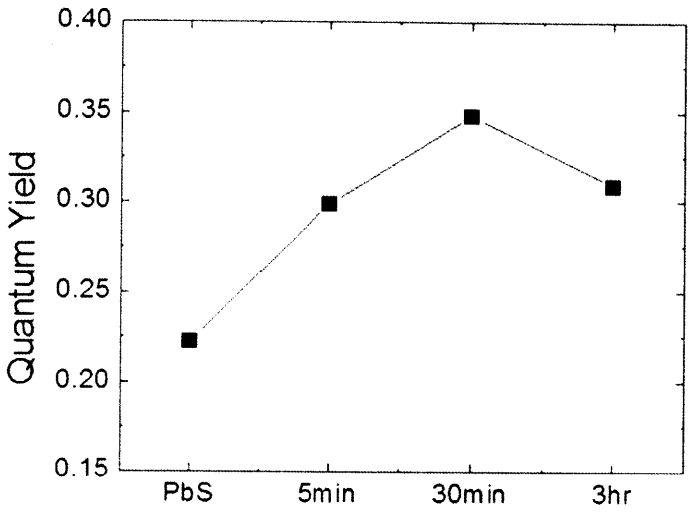

Figure 2-8. QY of PbS and PbS/CdS QDs depending on the reaction time

The air-stability of core/shell QDs is examined to show the protection ability of the shell layer from environmental exposures. PbS QDs are known to be oxidation-prone materials. The surface of PbS QDs, for instance, is oxidized to $PbSO_3$, $PbSO_4$, and PbO by air-exposure at the room temperature.[21,29,63,64] As a result, the emission from QDs is blue-shifted because effective size of QDs decreases as shown in Figure 2-9 (a). However, the emission from PbS/CdS QDs is stable in air (Figure 2-9 (b)). After a week air-exposure, the emission from core/shell QDs does not show any shift, while PbS QDs shows a blue-shift. This result suggests that core/shell QDs suppress environmental degradation of the optical properties, which will be beneficial in device applications.

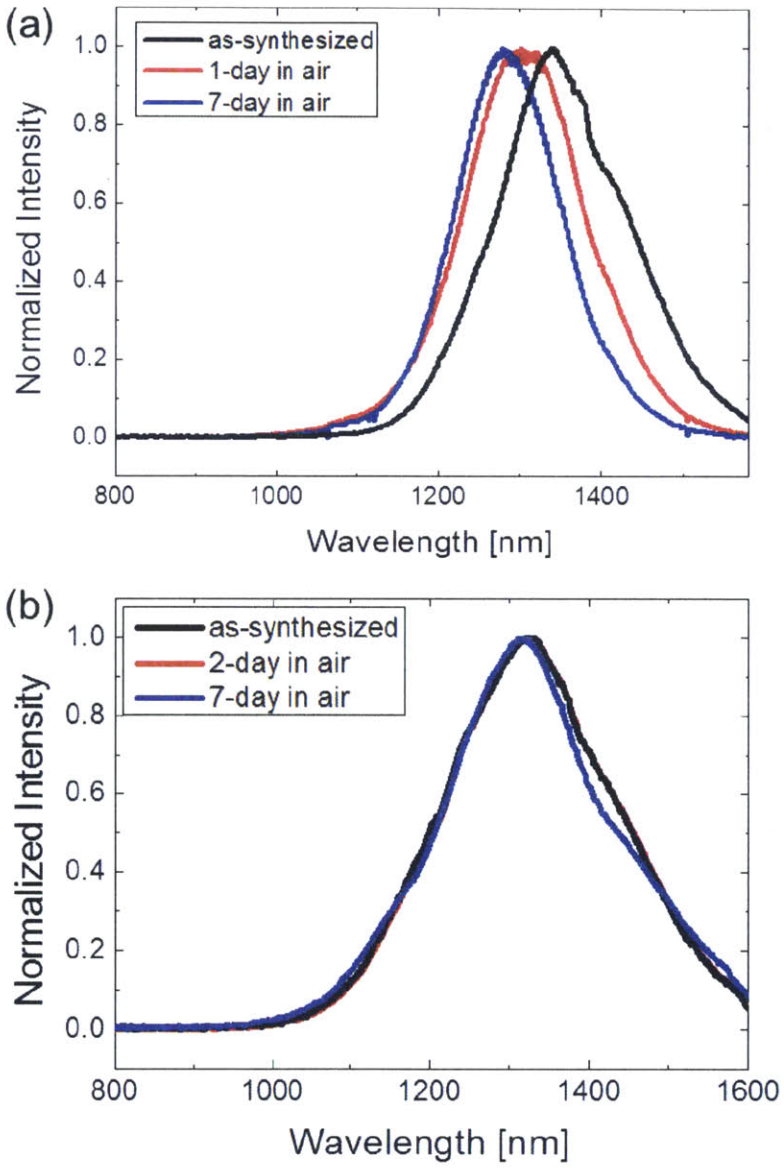

Figure 2-9. Spectral shifts of air-exposed (a) PbS core-only QDs and (b) PbS/CdS core/shell QDs. Emission peak of PbS core-only QDs shows blue shift after air-exposures, while that of PbS/CdS core/shell QDs remains same.

PL lifetime is compared for thin films of PbS core-only and PbS/CdS core/shell QDs with 5 min of cation exchange on glass substrates. As shown in Figure 2-10, PL lifetime increases with shell formation, which can be interpreted as decrease of the fast trap-assisted non-radiative exciton decay paths due to the reduction of trap states.

The optical characterization of QDs confirms that the CdS shell grows into the PbS core by cation-exchanges and this shell layer effectively passivates the surface states and protects the PbS core from degradation.

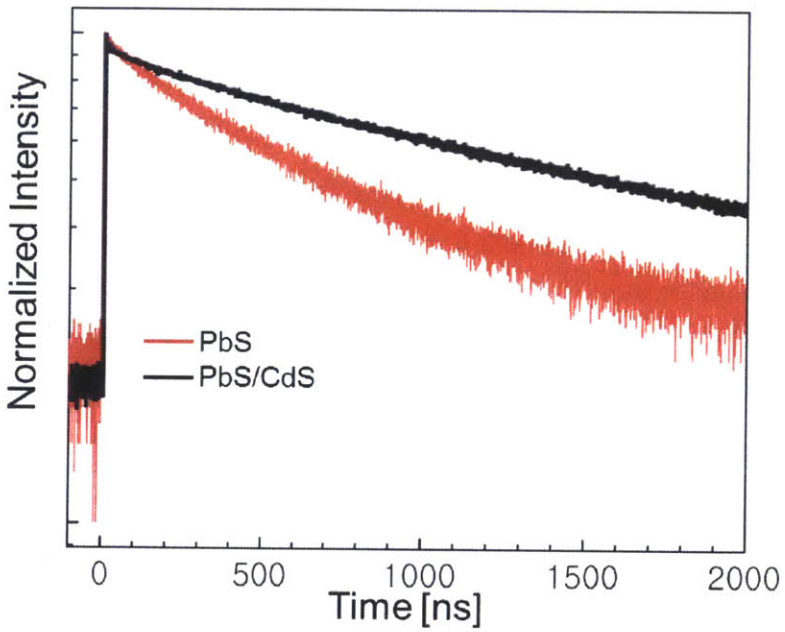

Figure 2-10. Time-resolved PL (tPL) results for PbS core-only (red) and PbS/CdS core/shell QDs (black) measured on glass substrates.

2.3.2 Shell Thickness

To calculate the shell thickness of CdS layer, the overall composition of Cd versus (*vs.*) Pb is measured for PbS/CdS QDs. For this calculation, two assumptions are required. First, there is no intermixing between PbS and CdS. This assumption is based on the abrupt core/shell boundary observed with anomalous small angle X-ray scattering (ASAXS) near

the Pb-absorption edge,[65] and the phase diagram (Figure 2-2). Second, PbS and CdS have the same unit cell volumes. At the interface, both Cd–S and Pb–S are strained because of lattice constraint and expected to have the same length. With these assumptions, the shell thickness is determined once the size of the QDs and the ratio of Pb-to-Cd are specified. Figure 2-11 (a) shows the composition analysis results using wavelength dispersion spectroscopy (WDS), and Figure 2-11 (b) shows the shell thickness as a function of the reaction time. The bond length of Cd–S calculated from the lattice constant is 253 pm.[j] The calculated numbers of MLs are 2, 2.5, 3, and 3.5 for PbS/CdS QDs that are cation exchanged for 5 min, 30 min, 2 hr, and 24 hr, respectively. During the initial 5 min, 2 ML of CdS shell is formed very rapidly. Then, these first two MLs act as a diffusion barrier, and slow down reaction rates for further reaction.[66] For electrical application of these core-shell QDs, PbS/CdS QDs with a thinner layer of the shell is required. However, our results show that first two layers of CdS form rapidly and it is challenging to grow a thin CdS shell that is less than 0.5 nm. Further discussion is presented in section 2.5.

[j] Further details of the crystal structure investigation(s) may be obtained from the Fachinformationszentrum Karlsruhe, 76344 Eggenstein-Leopoldshafen (Germany), on quoting the depository number ICSD-81925 for CdS at https://icsd.fiz-karlsruhe.de/search/basic.xhtml

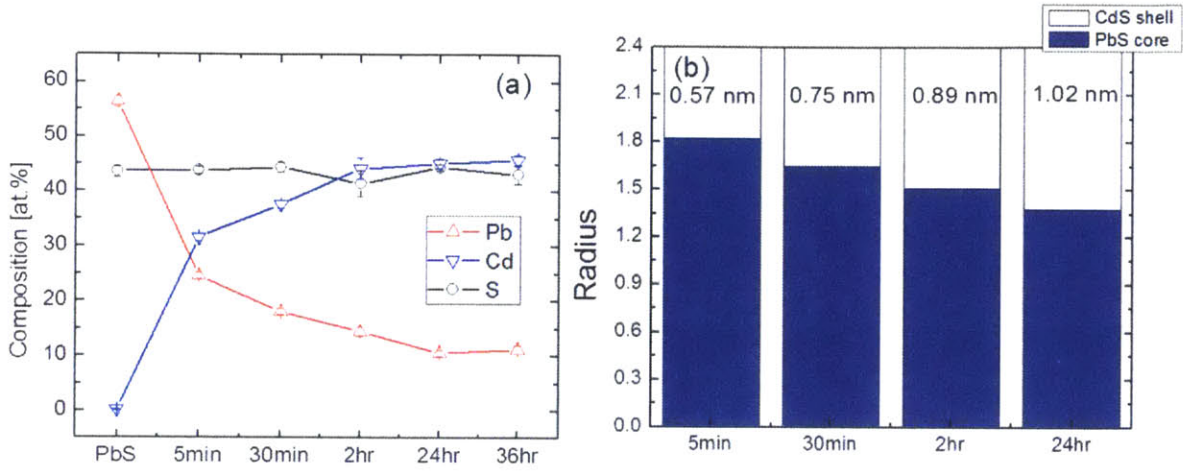

Figure 2-11. (a) Atomic composition of PbS/CdS QDs measured by WDS. (b) Calculated radial distribution of PbS/CdS.

2.4 SWIR *in vivo* Deep-Tissue Imaging

In vivo fluorescence imaging in the SWIR has several advantages in deep-tissue observation compared to visible and NIR. A mouse can be translucent in this range due to a long penetration depth and low scattering cross-section. Light attenuation due to absorption from blood and other tissue is limited in two spectral windows (1100–1400 nm and 1550–1900 nm) in SWIR (Figure 2-12),[34,35] and also low autofluorescence of tissue in this range leads to an increased sensitivity. However, SWIR imaging has been challenging due to the lack of proper emitters in this wavelengths. Currently, there is no organic dye emitting at these wavelength and exhibiting decent QY and photostability.[13–16] Carbon nanotube is another alternative to be used, however, it suffers from a large size, low QY, and poor solubility in water.[67] PbS/CdS core/shell QDs exhibit great potential as a SWIR emitter for deep-tissue imaging with their relative high QY in > 1550 nm, high photostability, and compact size. These QDs contain CdS shell and therefore, ligand/conjugation chemistry used in visible QDs can be adapted to synthesize SWIR QD–bio-molecular conjugates.[68,69]

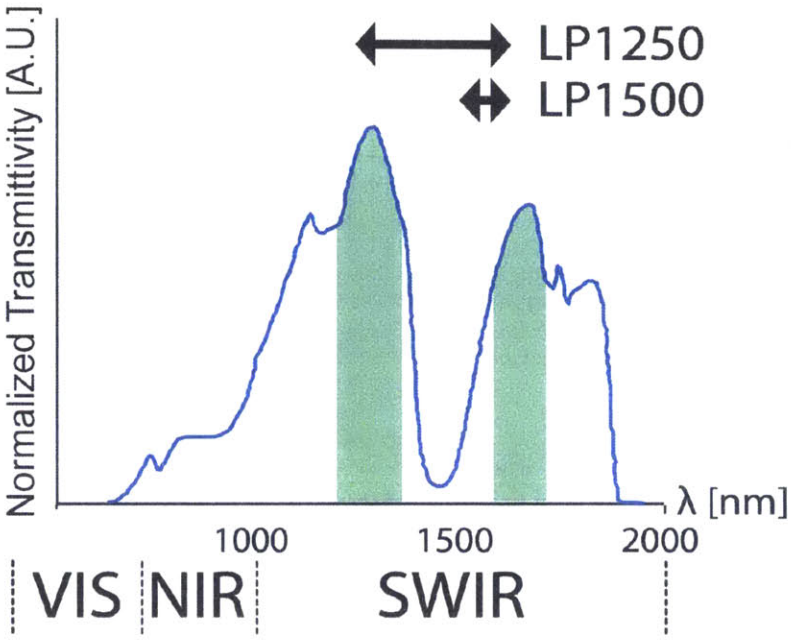

Figure 2-12. Tissue transmission in NIR and SWIR. Image reproduced from [34]

As a preliminary study, we observed the blood circulation of an awaken mouse while they are in motion (Figure 2-13). This is achieved using 1630 nm emitting PbS/CdS QDs. To solubilize PbS/CdS QDs in water, the QDs are encapsulated with 1,2-dioleoyl-sn-glycero-3-phosphoethanolamine-N-[methoxy(polyethylene glycol)-2000] ammonium salt (PEG-Lipids) (25 mg/mL in chloroform from Avanti Polar Lipids).[70]

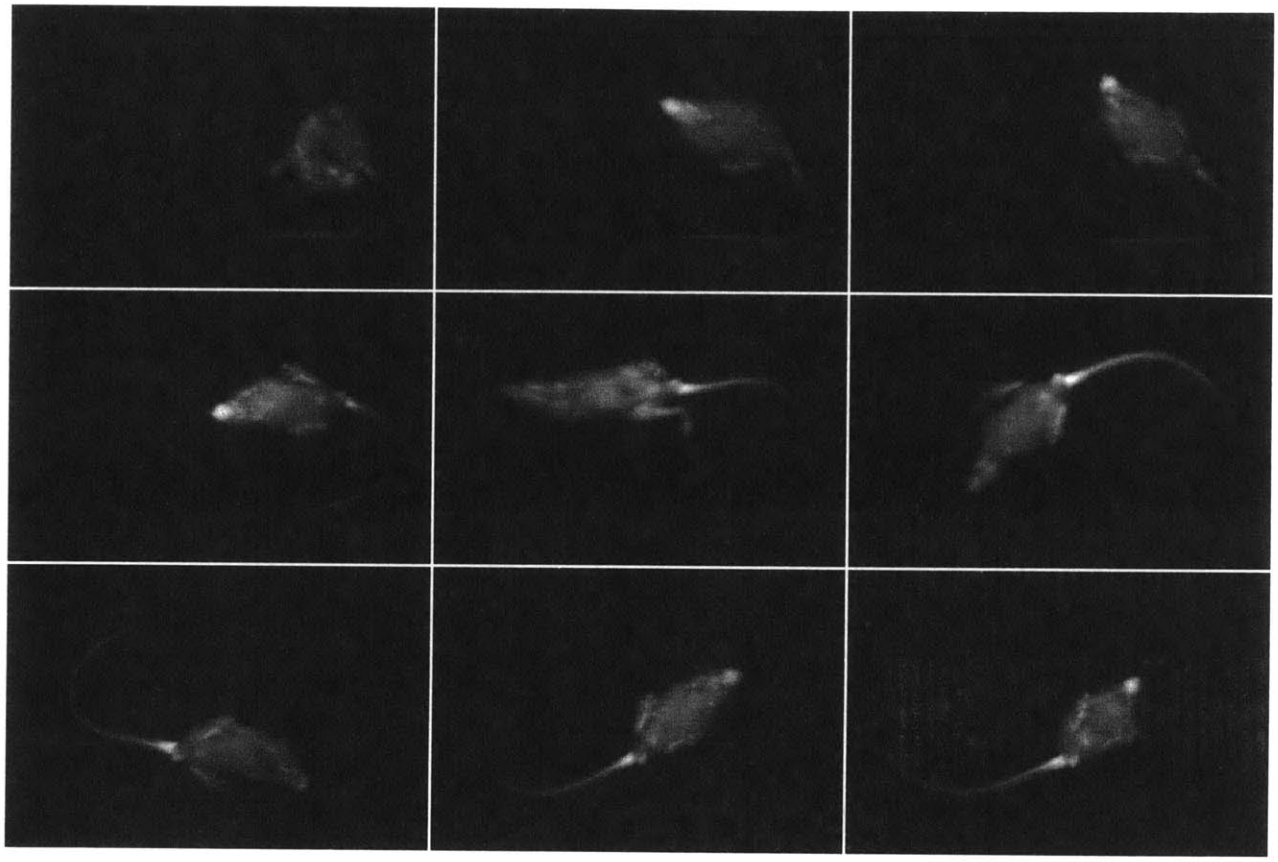

Figure 2-13. Still images captured from the fluorescent deep-tissue imaging video of an awaken mouse to which 1630 nm emitting PbS/CdS QDs were injected.

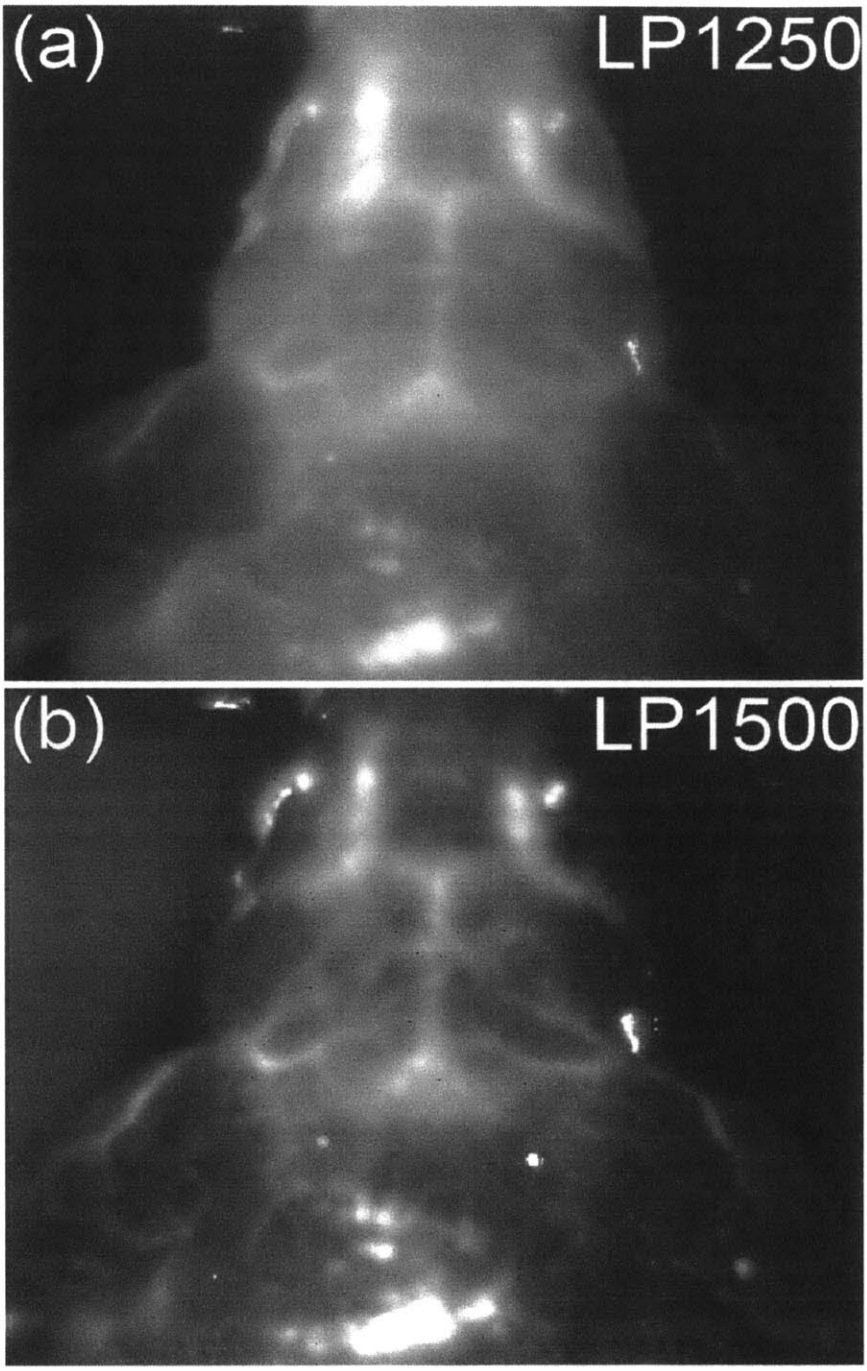

Figure 2-14. Images of brain vasculature through the skull of an anesthetized mouse in the SWIR (a) with 1250-long-pass (LP) filter and (b) 1500-nm LP filter.

For comparative study, we collected grayscale images of a brain vasculature *in vivo* after intravenous injection of 1300-nm emitting InAs and 1630-nm emitting PbS/CdS QDs (Figure 2-14). Figure 2-14 (a) shows emission from both InAs and PbS/CdS QDs with 1250-nm long-pass (LP) filter up to the detector cut-off (1650 nm), and Figure 2-14 (b) shows the emission only from PbS/CdS QDs with 1500-nm LP filter. Figure 2-14 (b) has excellent contrast between vasculature and other tissues because of a small scattering cross-section at these wavelengths.

2.5 Light Emitting Diodes Applications

Conventional SWIR technology is based on epitaxially grown III-V crystalline inorganic semiconductors, which requires high-cost process—high vacuum and high temperature. Unlike in visible, organic dyes have extremely low QY in SWIR and they cannot be used as low-cost alternatives.[33] However, demand has grown to develop SWIR emitters, which can be deposited on any substrate and produced at low cost for their applications. QDs are one of the promising candidates to satisfy these requirements because of their tunable band gap ranges and relative high QY. Among SWIR QD-LEDs, the device exhibiting the highest peak external quantum efficiency (EQE) is PbS QD-LEDs, which is 2.0 %.[31,32] This value is nearly 7 times higher than EQE of organic light emitting diodes (OLEDs) in SWIR, however, it is still inferior to that of III-V semiconductor devices.[13,31,32,71] One strategy to improve the performance of SWIR QD-LED is using core/shell QDs than core only QDs. In visible, the peak EQEs up to 18 % was achieved core/shell QDs (QD vision). [32] High QY of core/shell QDs is thought to contribute to the improved EQE of the device.

2.5.1 Electrical Conductivity of PbS/CdS QD Thin Films

The electrical conductivity is examined for PbS/CdS core/shell QD thin films before incorporation into devices. The thin films even with the thinnest shell QDs synthesized in previous section (2.3.2), which corresponds with 2-monolayers, are not sufficiently conductive as shown in Figure 2-15. (More detailed analysis on carrier density and mobility are presented in Chapter 3. See Figure 3-5 and 3-6.) The reason for this large degradation in electrical conductivity of PbS/CdS QD thin films, a factor of 50, is CdS shell layers playing a role as an additional barrier. To enhance the conductivity of films, this barrier for carrier transports must be reduced. The variable-range hopping (VRH) model[29,72] describes the carrier transport between QDs in films (Equation 2.3). The barrier height—band gap of CdS in this case—is determined by the material selection; however, the barrier width—shell layer thickness in this case—can be modulated to enhance conductivity. Therefore, the synthesis of thinner shell PbS/CdS QDs is required for electrical applications.

$$\Gamma_{ij} = \Gamma_0 \exp(-C\ (\beta \cdot d)^{\frac{3}{4}} \cdot \left(\frac{W}{kT}\right)^{\frac{1}{4}}) \qquad \text{(Equation 2.3)}$$

where Γ_{ij} is a hopping rate between site i and j, Γ_0 is a jump attempt frequency, β is a tunneling decay constant, which represents barrier height[k], d is a barrier width, and W is polydispersity.

[k] The tunneling decay constant, β is expressed as $\beta = \sqrt{(2m^* \bar{E}_{barrier}/\hbar^2)}$ from the Wentzel-Kramers-Brillouin (WKB) approximation.[72] $\bar{E}_{barrier}$ is a barrier height.

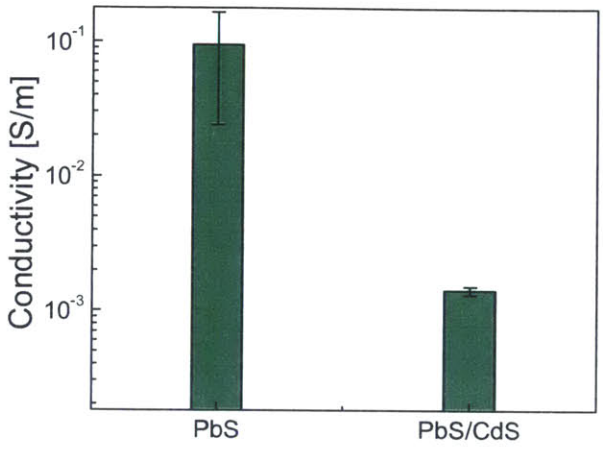

Figure 2-15. Conductivity of QD thin films made with 1,2-ethanedithiol (EDT)-treated PbS core-only QDs and PbS/CdS core/shell QDs.

2.5.2 Monolayer Shell Growth

As discussed in section 2.3.2, it is difficult to grow thin CdS shells with less than 2-ML thickness on the PbS QDs with the current synthesis condition, because of their rapid initial reaction rate. Currently, the reaction at 100 °C yields *ca.* 0.55 nm of shell thickness in 5 min, which corresponds to 2 MLs. As shown in Figure 2-16, the emission of these QDs exhibits a shoulder peak near 1400 nm, which suggests the presence of thinner shell QDs. To synthesize PbS/CdS QDs with a thinner shell, a new reaction condition is required for slowing down the reaction rate.

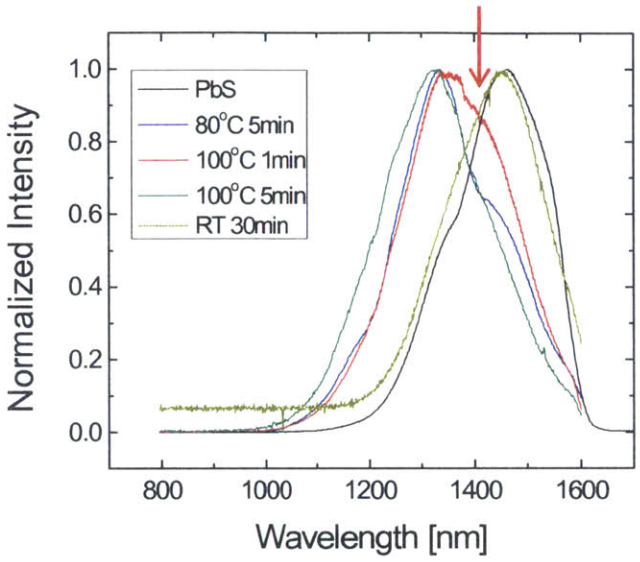

Figure 2-16. Emission of Pbs and PbS/CdS QDs with different reaction conditions. An extra emission peak is observed when cation exchange was performed at lower temperature (80 °C) or for a short time (less than 5 min). The QDs colored in green is PbS/CdS QDs with 2 MLs of CdS. Therefore, we speculate that the shoulder peaks near 1400 nm (arrow) are from PbS/CdS QDs with 1 ML of CdS.

To slow down the grow rate of CdS shell, we attempted to decrease the reaction temperature and Cd-precursor concentration, and search for alternative less-reactive Cd-precursors. The reaction rate decreases as the reaction temperature decreases following Arrhenius equation. The limited concentration of the Cd-precursor is expected to hinder the diffusion of Cd in the cation exchange process.[66] Figure 2-17 shows the emission of core-shell QDs that are cation-exchanged at different temperatures, with different concentration of Pb precursors and with a less reactive precursor. Figure 2-17 (a) shows that performing cation exchange at a lower temperature is effective to create a thinner shell layer. With a lower concentration of the Cd-precursor, a longer reaction time (5 min) still yields the thinner shell layer. WDS measurement confirms that this layer corresponds to 0.21 nm (~1 ML). The reactivity of cadmium tetradecylphosphonate (Cd-TDPA) is too low to create CdS shell layers at 60 °C as shown in Figure 2-17 (b).

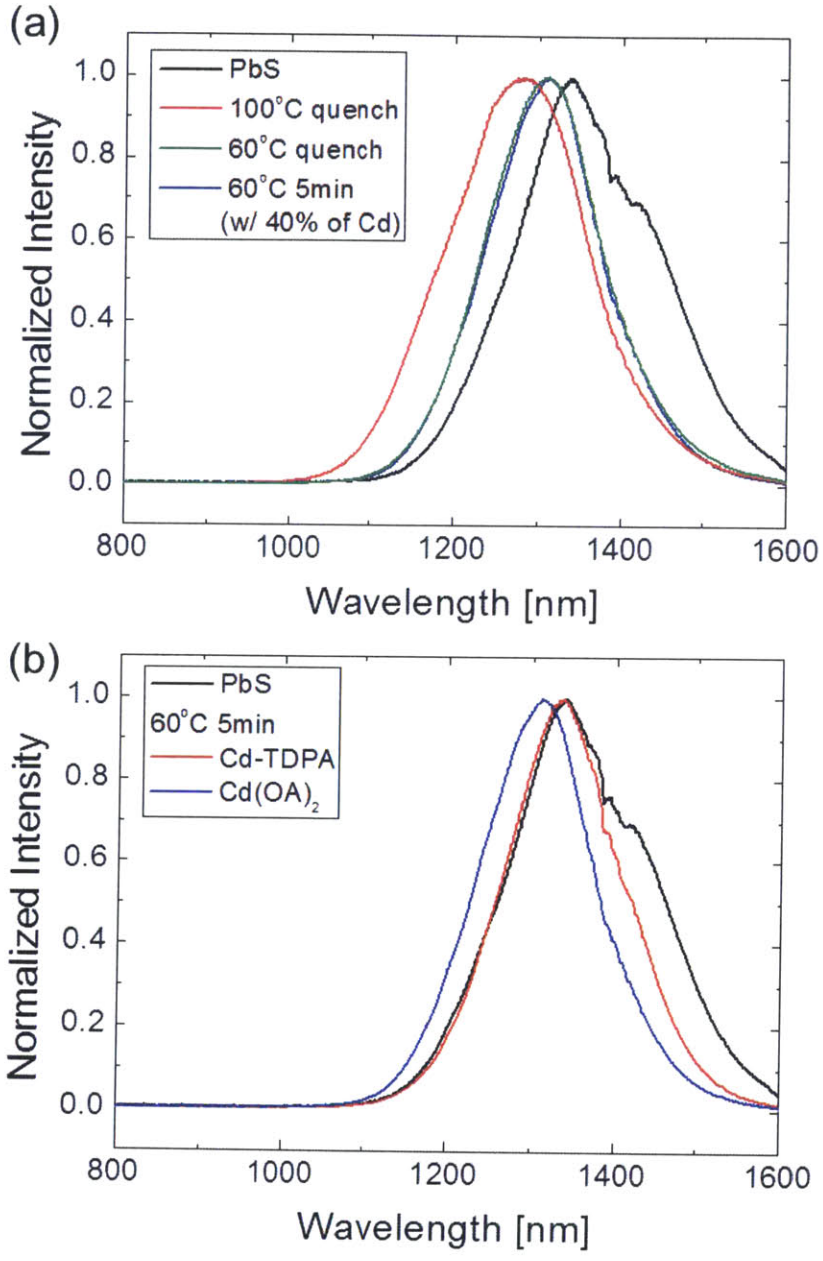

Figure 2-17. (a) When cation exchange of PbS QDs is performed at a lower temperature (60 °C), single emission peak is observed at higher wavelength than PbS/CdS with 2 MLs of CdS shell (red). (b) Emission of PbS/CdS QDs that are cation exchanged with different Cd-precursors – Cd-TDPA and $Cd(OA)_2$.

The QY of PbS QDs are measured before and after growth of the shell. QY is a good measure of the passivation of surface states as it is influenced by the rate of non-radiative decay. As shown in Figure 2-18, QY increases dramatically after the first-shell layer is formed. QY starts to decrease after growing the 2.5 MLs of shells, which is consistent with other core/shell QD systems.[61] A monolayer CdS shell synthesized at the lower temperature shows sufficient passivation of the PbS surface and yields increase of QY by > 60 %. These monolayer-shell QDs are incorporated into LEDs to examine their potential for electrical applications. The electrical properties of the monolayer-shell QDs such as carrier concentration and mobility are characterized using Mott-Schottky analysis and will be presented in Chapter 3.

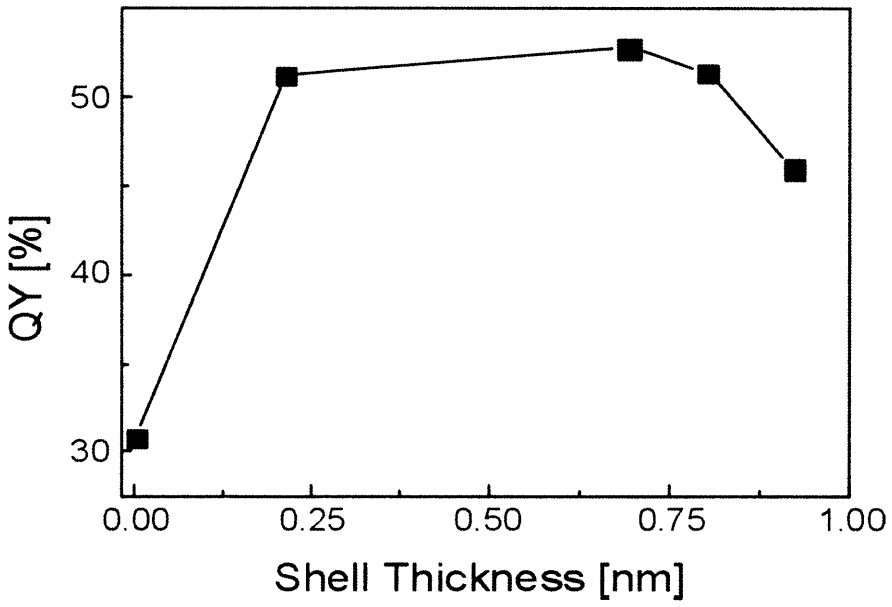

Figure 2-18. QY measurements show that QDs with a monolayer shell have a QY that is comparable to that of the other thicker shell QDs.

2.5.3 Device Characterization

We examined the performance of SWIR LEDs in 'type-IV' QD-LED structures[1] as shown in Figure 2-19.[32] These devices incorporate PbS/CdS core/shell QDs as an electrically-driven emitter. QD-LEDs are prepared with three different QD samples: PbS core-only QDs, PbS/CdS core/shell QDs with a monolayer CdS shell (0.2 nm), and PbS/CdS core/shell QDs with highest QY (0.7-nm shell), and each sample is referred as core-only LEDs, thin-shell LEDs, thick-shell LEDs, respectively. The devices are fabricated as follows: 50-nm-thick sol-gel ZnO film was deposited on a pre-patterned indium-doped tin oxide (ITO)/glass substrate by spin-casting and annealed at 300 °C for 5 min under humidity-controlled (10–20 %) environments. QDs with native OA ligands were spin-casted on the ZnO film to yield a 10-nm-thick layer. On the QD layer, a 150-nm-thick 4,4-bis(9H-carbazol-9-yl)biphenyl (CBP) layer, a 10-nm-thick molybdenum oxide (MoO_x) layer and a 100-nm-thick Au layers are successively deposited by thermal evaporation using shadow masks. These layers are used as a hole transport layer (HTL), a hole-injection layer, and a top electrode respectively.

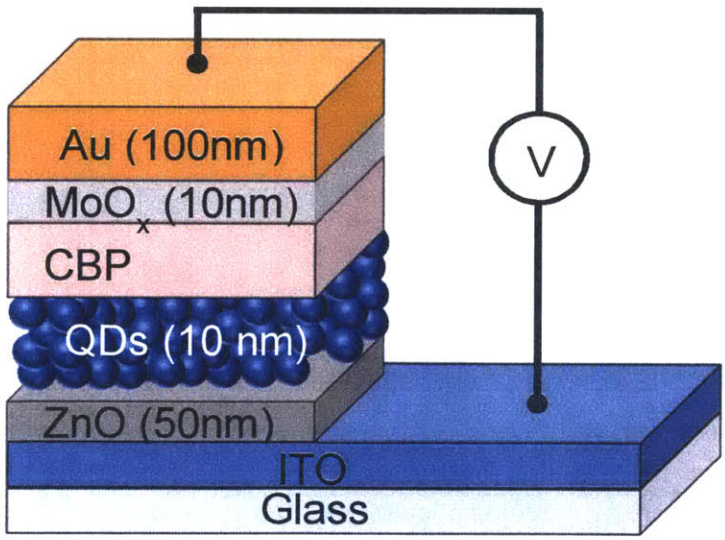

Figure 2-19. Schematic diagram of the 'type-IV' QD-LED structure used for this study.

[1] Using hybrid organic-inorganic charge transport layers (CTLs). In particular, inorganic n-type semiconductor (ZnO) is used for ETLs, and organic semiconductor (CBP) is used for HTLs in this study.

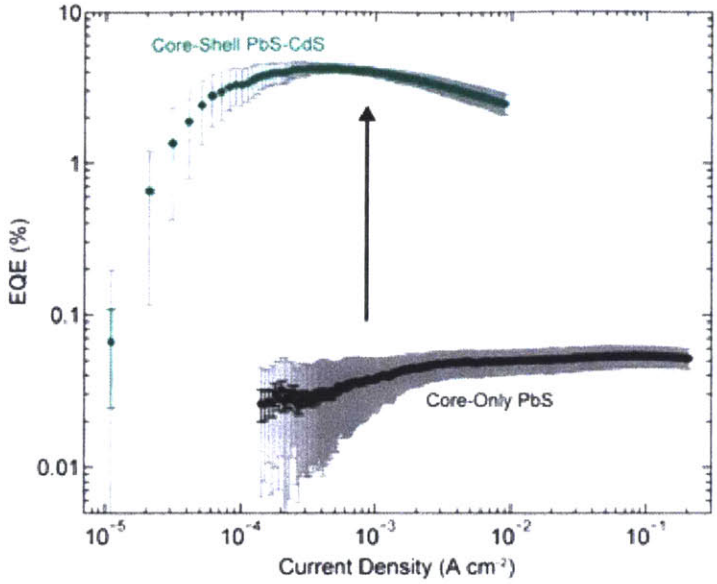

Figure 2-20. Average EQE at near 1300 nm *vs.* current density of IR QD-LEDs with PbS/CdS core/shell QDs and PbS core-only. The EQE of devices depends on current density (as known as efficiency droop) and the highest EQE value is referred as peak-EQE.

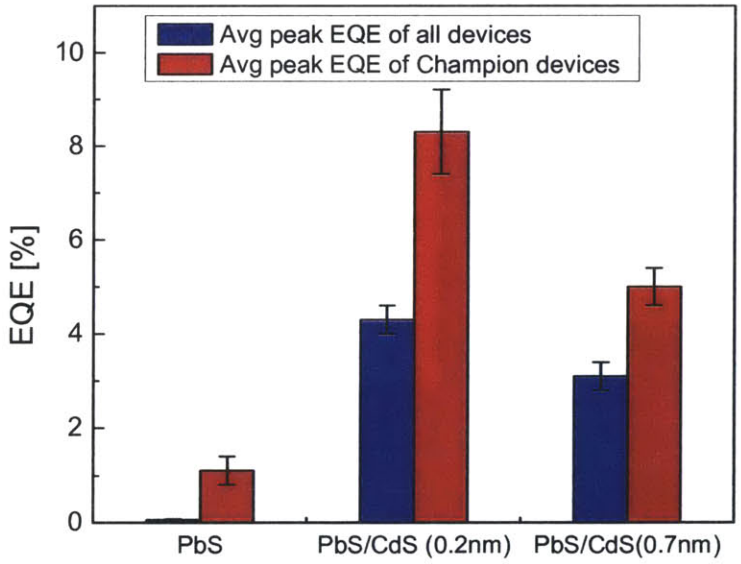

Figure 2-21. Average peak EQEs for all devices and the champion device with PbS core-only QDs and thin-shell and thick shell (highest QY) PbS/CdS QDs. Blue bars represent the average of the peak-EQEs from devices on all chips, and red bars represent the average among the devices on the best-performing chip (1 chip contains 10 devices).

By replacing core only QDs with core/shell QDs, EQE of the devices are improved. The average peak-EQE for core-only LED is 0.05 %. In the same device architecture, the average peak-EQE of thin-shell LED is 4.3 %. This is the best reported value in SWIR QD-LEDs (Figure 2-22). Of note, this highest EQE is achieved without ligand treatments. Considering that Sun *et al.* fabricated the best performing LED by introducing shorter ligands,[31] we speculate that higher peak-EQE can be achieved is by exchanging the native ligands with shorter ligands. The EQE enhancement by using core/shell QDs cannot be solely explained by the increase of PL QY after the shell growth. After growing a monolayer of CdS on PbS, the QY increases from 30.8 % to 51.3 %. However, EQE of device increases 80-fold, from 0.05 % to 4.3 %. Thick-shell LED exhibits EQE of 3.1 %, which is slightly less than that of the thin-shell LED. The lower EQE of the thick-shell LED may be due to the hindered charge injection by a thick shell[m].

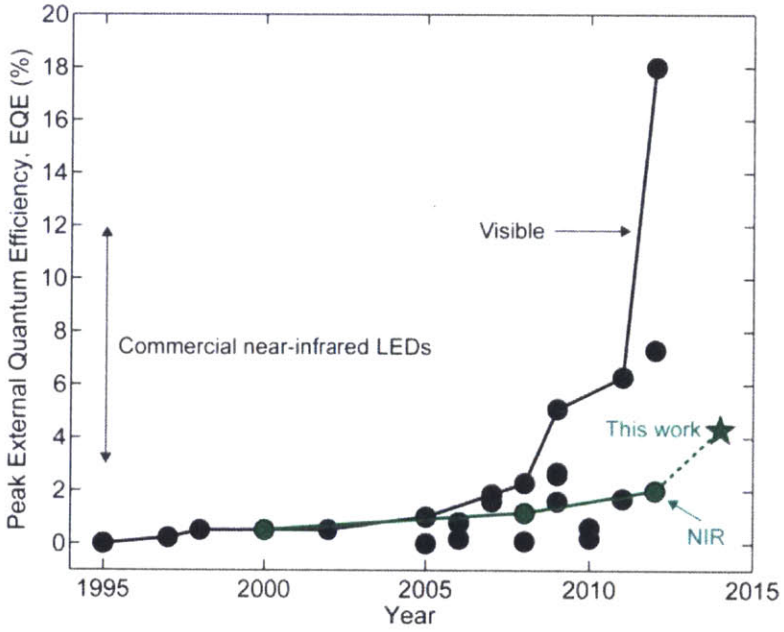

Figure 2-22. Peak EQE progression of visible and IR QD-LED performance over time. Image adopted from Refs: [32,33]

[m] Electrical characterization for mobility and carrier concentration is performed by Mott-Schottky analysis in Chapter 3 (Figure 3-5 and 3-6).

To examine the origin of EQE enhancements, we measured PL intensity of core/shell QD thin films in the sandwich structure of CBP/QDs/ZnO, which resembles the structure in the devices. Relative device QYs are defined by dividing these values with the PL intensity of PbS core-only QD thin films in the same structure. As shown in Figure 2-23, relative device QY increases 32-fold with 0.2-nm shell and 29-fold with 0.7-nm shell. The generally good agreement between relative device QY and EQE indicates that the increase in relative device QY mostly explains the EQE enhancement. Time-resolved PL measurements provide further insight to shell dependent PL intensity in the device. Compared with QDs on a glass substrate, PL lifetimes are reduced for both core-only and core/shell QDs in the presence of CTLs (Figure 2-24). The longer PL lifetimes of core/shell *vs.* core-only QDs with CTLs indicate that CdS shell layer mitigates exciton quenching induced by CTLs (Figure 2-24 (b)). The EQE enhancement by introducing CdS shell layers is mainly from the protection of exciton quenching induced by CTLs.

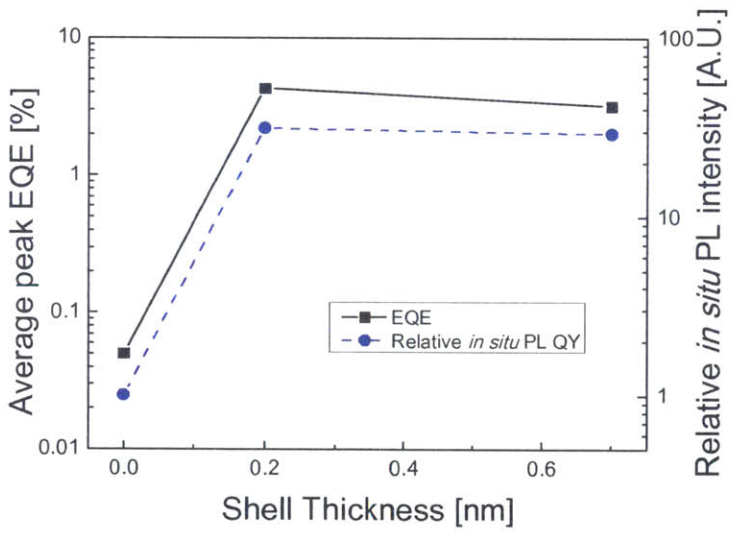

Figure 2-23. Average peak EQE and relative *in situ* PL intensity of QDs with different shell thickness.

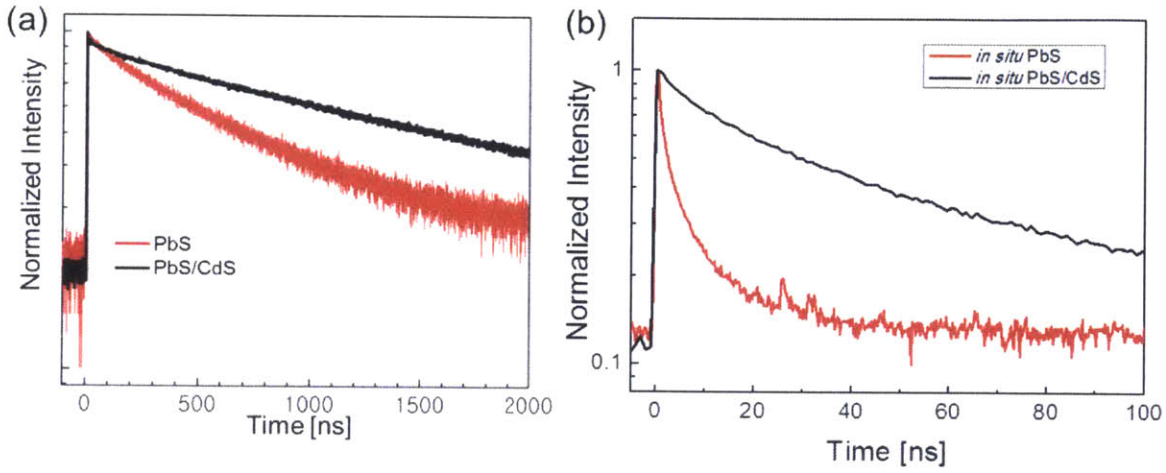

Figure 2-24. PL decay curves for PbS core-only (red) and PbS/CdS core/shell QDs (black) (a) on the glass substrates and (b) with CTLs (*in situ*).

2.6 Summary

In this chapter, PbS/CdS core/shell QDs are synthesized by cation-exchanges, characterized for their optical and electrical properties, and examined their performance in potential SWIR applications. Our results show that growing CdS shell layers effectively passivate the surface states and protect excitons from non-radiative decay by separating them from environments. Therefore, core/shell QDs show an enhanced QY and stability in air and in devices. The potential of PbS/CdS QDs for deep-tissue imaging in SWIR is tested using 1630-nm emitting QDs. For the electrical applications, thinner shell layer is required because thick CdS shell hinders the transport of electrical carriers. After modifying the reaction conditions, we are able to synthesize PbS/CdS QDs with a monolayer of CdS. These QDs also show an improved stability and QY up to 90% compared to those of thick shells. SWIR QD-LEDs made with PbS/CdS QDs with a monolayer-shell exhibit twice higher EQE than any previously reported SWIR QD-LEDs.

Chapter 3.

Electrical Characterization of QD Thin Films

Capacitance-Based measurement Techniques

Previous studies to improve the performance of QD devices lack direct measurements on the electrical properties of QD thin films or trap states. In most cases, researchers report the influence of specific chemical treatments to the efficiency of QD devices instead of unveiling how those chemical treatments change the electrical properties of QD thin films. The surface trap states play an important role in the electronic structure of QD thin films, thereby determines the electrical properties. Even though most of the chemical treatments focus on passivating the trap states, techniques to characterize the density and energy of trap states in QDs are not well developed. Capacitance-based techniques are effectively used to characterize trap states in bulk semiconductors; therefore, we expect that they can also be used for characterizing traps in QDs.

Most of previous electrical characterization of QD thin films relies on current-based measurements such as thin-film field effect transistor (FET) characterization and charge extraction by linearly increasing voltage (CELIV).[63,73,74] These techniques are used to characterize the mobility and the carrier density of thin films, however, they provide extremely limited information on trap states. Capacitance measurements yield the density and energy of trap states and carrier density.[74–76] However, incorrect measurement

procedures used in the characterization of QD thin films or inappropriate analysis of dielectric constants leads to misinterpretation of data.[74] In this chapter, proper procedure for impedance analysis and capacitance-based technique for QD thin films and their interpretation will be discussed.

3.1 Capacitance

Capacitance is a measure of ability to store electric charges. A simple structure that can store charges is a parallel plate capacitor, and its capacitance is determined by its geometry and the dielectric properties of materials inside (Equation 3.1).

$$C = \frac{dQ}{dV} = \varepsilon_r \varepsilon_0 \frac{A}{d} \qquad \text{(Equation 3.1)}$$

where C is capacitance, Q is charge, V is applied bias (or voltage), ε_r is relative permittivity or dielectric constant of materials between the plates, ε_0 is the permittivity of vacuum, A is area of plates, and d is distance between the plates (or electrodes)

The dielectric property of materials arises from the polarizability of materials under electric field. The polarization mechanisms contributing to the dielectric constant are atomic (or electronic), ionic (or vibrational), dipolar (or orientational), and interfacial (or space charge) polarizations. Figure 3-1 shows dependence of the dielectric constant of a material on the frequency of an applied electric field. Dielectric constants measured at extremely low frequency ($f \rightarrow 0$ Hz) is referred as static dielectric constant, while that measured at extremely high frequency ($f \rightarrow \infty$) is called as optical dielectric constant. Static dielectric constant arises from dipolar, ionic and atomic polarization mechanisms, and optical dielectric constant arises only from atomic polarization, which is closely related to refractive index of materials[n].

[n] A relation between complex dielectric constant and refractive index is given by

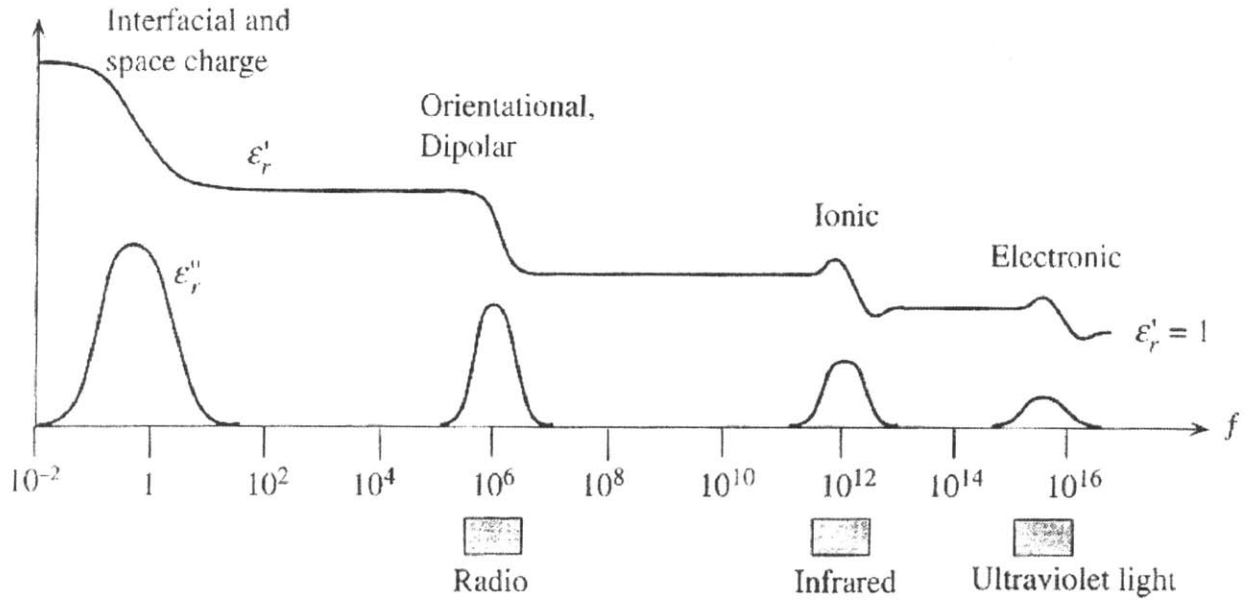

Figure 3-1. Dielectric constant (ε′) and dielectric loss (ε″) *vs.* frequency showing frequency dependence of polarization mechanism. Image taken from Ref: [77]

3.2 Measuring Dielectric Constant

Dielectric constant (ε_r) is an essential constant for characterizing materials with capacitance-based techniques. The dielectric constant of PbS QD thin films is much different from that of PbS bulk materials, because PbS QD thin films consists of PbS and substantial amount of organic ligands, which exhibit far smaller dielectric constant than inorganic materials. Accurate estimation of the dielectric constant of PbS QD thin film is challenging because the value depends on the type of ligands, the length of ligands, the packing density of QDs,

---

$$\underline{\varepsilon_r} = \varepsilon'_r + i\,\varepsilon''_r = \underline{n}^2 = (n + i\kappa)^2$$

Where $\underline{\varepsilon_r}$ is complex dielectric constant, ε' is a real part of dielectric constant and ε" is an imaginary part, $\underline{n}$ is complex refractive index, n is a real part of refractive index, and κ is the distinction coefficient of materials.

and the size of QDs.[78] Hence, careful measurement of the dielectric constant of PbS QD thin films should be the first step for the further electrical characterizations such as Mott-Schottky or any other capacitance-based trap analysis.

In general, the dielectric constant of a material is measured by a simple capacitance-voltage (C-V) measurement using an impedance analyzer. However, the simplified C_P or C_S models offered by impedance analyzers cannot be used to measure the dielectric constant of QD thin films. Instead, capacitance should be calculated by including both contact resistance and parallel resistance. Bozyigit *et al.* pointed out that dielectric constants measured with inadequate procedures are used in previous works.[74]

The metal-QDs-metal capacitor (Figure 3-2 (a)) can be simplified to an equivalent circuit as shown in Figure 3-2 (b). The impedance analyzer measures the real part (Z') and the imaginary part (Z") of impedance (Z), and fits them to a model to calculate the capacitance (C). In the equivalent circuit model (Figure 3-2 (b)), we have three unknown variables (C, R_S, R_P), while having two measured parameters (Z', Z"). This is not a solvable model. Thus, impedance analyzers generally offer two simplified models, C_P and C_S, all of which consist of two unknown variables (Figure 3-2 (c) and (d)). C_P model is valid when R_S from contact resistance is negligible. C_S model is valid when leakage current is negligible ($R_P \rightarrow \infty$). For QD thin films, the validity of each model is not yet confirmed. The major factor determining the validity of models is the level of leakage currents. Grinolds *et al.* solved this problem by inserting additional insulating layers between electrodes and QD films to prevent leakage currents.[78] This strategy requires extraneous sample preparation.

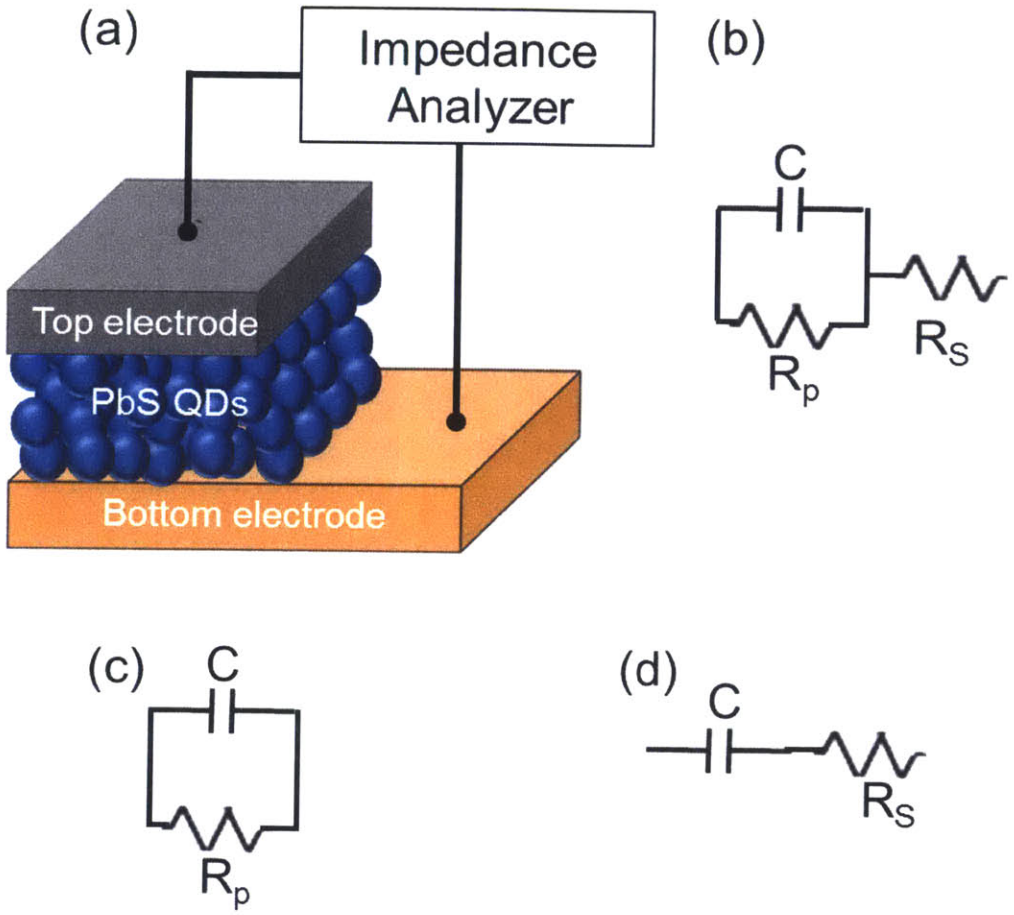

Figure 3-2. (a) Typical C-V measurement scheme for a MIM capacitor, (b) an equivalent circuit model with both contact resistance (R_s) and leakage currents (R_p), (c) a simplified equivalent circuit when R_p is dominant and (d) when R_s is dominant.

Another strategy to solve the model in Figure 3-2 (b) is performing additional measurements at different frequencies. The real parts, R_S and R_P are independent with frequency, however, the imaginary part, the capacitive reactance ($X_c = 1/i\omega C$), depends on frequency. Therefore, after measuring Z at two different frequencies, we have 4 measured parameters—two pairs of Z' and Z" from two different frequencies— and 4 unknown variables—$X_{c,f1}$, $X_{c,f2}$, R_S and R_P.

Nyquist plot is a parametric plot of a frequency response and illustrate the capacitance measurements (Z' and Z") at different frequencies. It gives both dielectric constant and information about the validity of two simple models. The schematic diagrams of Nyquist plots for previously discussed equivalent circuit models illustrated in Figure 3-3. The shape of plots indicates which models can be used for the capacitance measurements. When both C_P and C_S models are not applicable, the dielectric constants can be extracted from the Nyquist plots at resonant frequency ($f_c = 2\pi\omega_c$). The results from PbS QDs with native OA ligands and 1,2-ethanedithiol (EDT) ligands are shown in Figure 3-4. The calculated dielectric constants are 5 for PbS QD films with native OA ligands, and 17 for PbS QDs with EDT ligands.

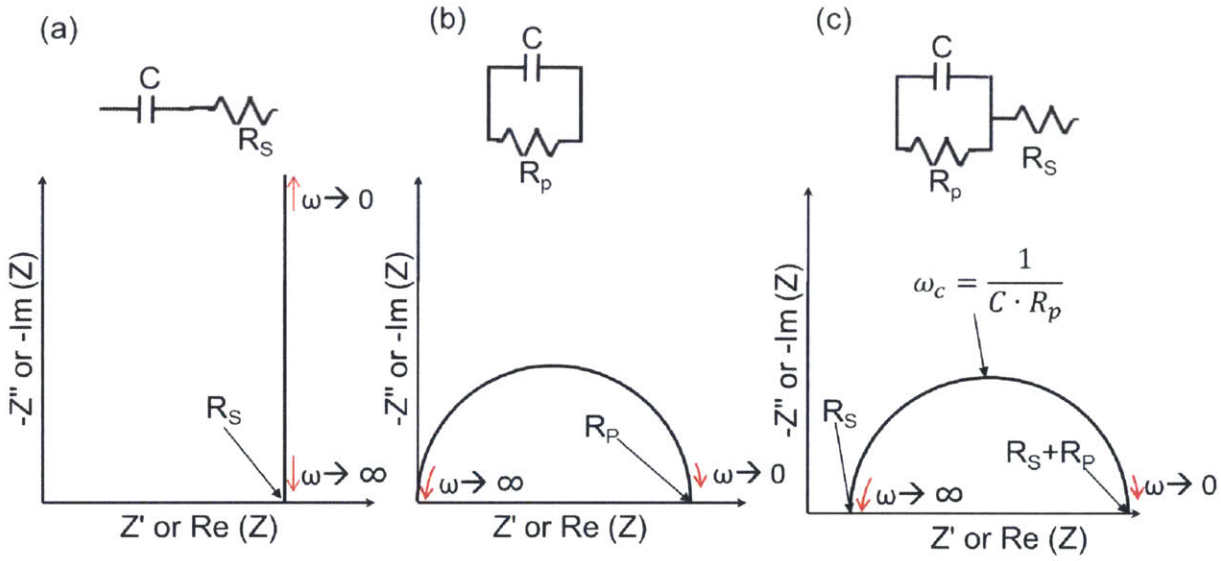

Figure 3-3. Schematic diagram of Nyquist plots for each corresponding equivalent circuit model. (a) C_p model, (b) C_s model, and (c) model considering both R_p and R_s.

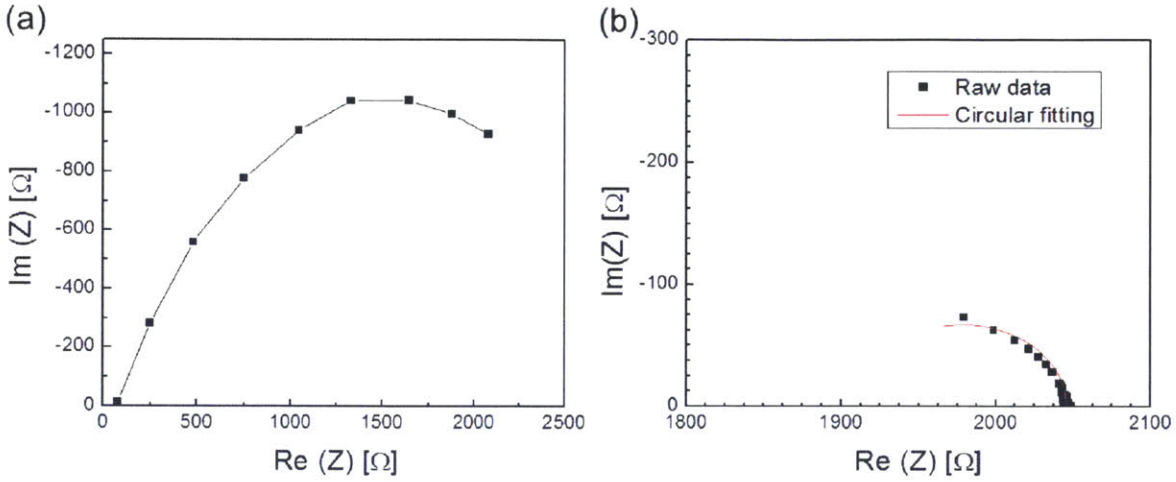

Figure 3-4. Capacitance *vs.* frequency sweep measurement at 0 V with 20 mV modulation results illustrated by Nyquist plots for (a) EDT-treated PbS QD thin films and (b) PbS QD thin films with native OA ligands.

3.3 Junction Capacitance

In semiconductor junctions, capacitance associated with depletion region provides extensive information on the characteristics of electrically active states. Analysis on the capacitance variation (ΔC) *vs.* applied bias (V_a) is the basis of several techniques used for determining the properties of carriers and impurities such as their concentrations, profile and energy levels. Depletion capacitance measurements are particularly useful for estimating the depth distribution of states or impurities without physical removal of the materials. Despite their extensive capabilities to characterize semiconductor junctions, capacitance measurement techniques are not widely utilized for the QD thin films.

The depletion capacitance is associated with the capacitance in the band bending region of Schottky or p-n junction. The depletion capacitance mainly depends on the depletion width inside the junction as shown in Equation 3.2. The depletion width, given by Equation 3.3, is determined by applied bias and several parameters of materials such as ionized donors and

acceptors, and dielectric constant. Assuming uniform doping profile throughout the n- or p-type region, the depletion width for p-n junction and Schottky junction is given by Equation 3.3.

$$C = A\frac{dQ}{dV_a} = \frac{\varepsilon_r \varepsilon_0 A}{x_d} \qquad \text{(Equation 3.2)}$$

In this equation, A is area of devices, Q is stored charge, V_a is applied bias, ε_r is relative dielectric constant of materials, ε_0 is permittivity of vacuum, and x_d is depletion width.

$$x_d = (x_n + x_p) = \left(\frac{2\varepsilon_r \varepsilon_0}{e}\left(\frac{N_A + N_D}{N_A N_D}\right)V\right)^{1/2} \quad \text{(For p-n junction)}$$

$$= \left(\frac{2\varepsilon_r \varepsilon_0}{eN_d} \cdot V\right)^{1/2} \quad \text{(For Schottky junction) (Equation 3.3)}$$

In this equation, x_n is the depletion width for n-side, x_p is the depletion width for p-side, e is an elementary charge, N_A is acceptor concentration, N_D is donor concentration, V is sum of applied bias and built-in potential ($V = V_a + V_b$), and N_d is doping concentration (either donor or acceptor).

3.3.1 Mott-Schottky Analysis

The doping concentration for uniform doping or the doping profile for non-uniform doping can be measured using Mott-Schottky analysis from the C-V measurements. The change of depletion capacitance (ΔC) is measured as the applied reverse bias (V_R) is slowly increased. The depletion width (x_d) increases with increasing reverse bias. The amount of changes is related to the doping (or impurity) concentration. When the reverse bias is increased by a step ΔV_R, the depletion width increases by Δx_d, and the capacitance decreases by ΔC. If $\Delta x_d << x_d$, the relation between ΔV_R and Δx_d can be calculated as:

$$\Delta V_R = \frac{e}{\varepsilon_r \varepsilon_0} N_d(x_d) \cdot x_d \Delta x_d \qquad \text{(Equation 3.4)}$$

where N_d (x_d) is a doping level or impurity level at $x=x_d$.

From the Equation 3.2 and 3.4, the ratio of ΔC and ΔV_R is expressed using $N_d(x_d)$ and x_d as:

$$\frac{\Delta C}{\Delta V_R} = \frac{\Delta C}{\Delta x_d} \cdot \frac{\Delta x_d}{\Delta V_R} = -\frac{\varepsilon_r \varepsilon_0 A}{(\Delta x_d)^2} \cdot \frac{\varepsilon_r \varepsilon_0}{x_d \cdot e N_d(x_d)} \qquad \text{(Equation 3.5)}$$

Using Equation 3.2 and 3.5, the doping concentration at x_d can be derived as:

$$N(x_d) = \frac{-C^3}{e \varepsilon_r \varepsilon_0 A^2} \cdot \left(\frac{\Delta C}{\Delta V_R}\right)^{-1} \qquad \text{(Equation 3.6)}$$

And it can be modified to a different form:

$$N(x_d) = \frac{-2}{e \varepsilon_r \varepsilon_0 A^2} \cdot \left(\frac{\Delta C^{-2}}{\Delta V_R}\right)^{-1} \qquad \text{(Equation 3.7)}$$

In this equation, the small step size can be understood as derivatives, hence, local slopes in the plot of C^{-2} *vs.* V give doping concentration inside depletion region at the corresponding x_d. In addition, the x-intercept gives a built-in potential (V_b).

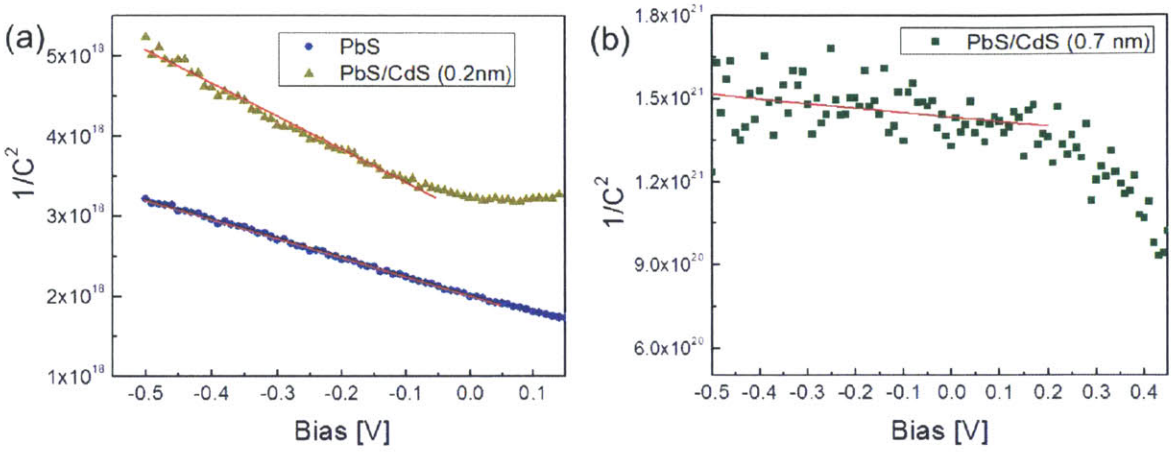

Figure 3-5. Results of Mott-Schottky analysis for thin films of (a) PbS core-only QDs and PbS/CdS QDs with a thin ML CdS shell layer and (b) with a thick CdS shell layer used in Chapter 2.

I measured the carrier concentration of PbS core-only and PbS/CdS core/shell QD thin films, which were used for LED applications in Chapter 2. The slope is extracted from the reverse bias regime as shown in Figure 3-5. Carrier concentration is calculated using Equation 3.7 and mobility is calculated using the carrier concentration and conductivity results from Figure 2-15. As shown in Figure 3-6, the carrier mobility decreases considerably after the shell formation, but carrier concentration in thin shell (0.2 nm) QDs is comparable to core-only QDs. In Figure 2-21 and 2-23, thick-shell LED exhibits lower EQE than thin-shell LED even though they have similar device QY. The dramatic decrease of carrier concentration in the thick-shell QD thin films can be a reason for the lower EQE of thick-shell LED compared to thin-shell LED (Figure 3-6 (a)).

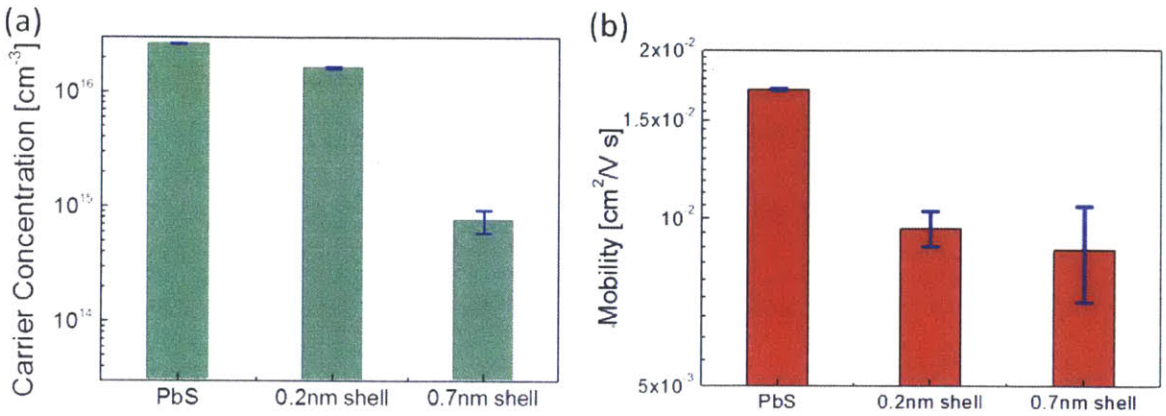

Figure 3-6. (a) Carrier concentration from Mott-Schottky analysis and (b) extracted mobility combining with conductivity measurements for PbS core-only and PbS/CdS core/shell QDs used in Chapter 2.

3.3.2 Drive-Level Capacitance Profiling

Drive-level capacitance profiling (DLCP) is an advanced junction capacitance analyzing technique for the characterization of the density, energy and position of electronic states inside band gap. This technique is originally developed for materials possessing a large number of defects, such as amorphous silicon and poly-crystalline $CuIn_xGa_{1-x}Se_2$.[79,80] To characterize traps in QD thin films, DLCP is more appropriate than commonly-used deep-level transient spectroscopy (DLTS) because conventional DLTS can be only used for materials with sufficiently low defect concentrations to ensure the exponential decay of capacitance,[74,81–83] and QD films are known to have a larger density of traps than the density of free carriers.[73,75,81] In DLCP, the density of trap states is measured by analyzing the capacitance response—which depends on the depletion width in Schottky diodes—at different modulation amplitudes and frequencies. Another advantage of this technique is that the only *a priori* knowledge required for the technique is the dielectric constant, ε, of the semiconductors.

As shown Figure 3-7, the energy difference between trap states and band edge (conduction band minima or valence band maxima) determines the characteristic time constant for capturing rate and emission rate of trap states, and this relation is given by

$$E_t = -kT\ ln\left(\frac{\omega}{2\pi\nu_0 T^2}\right) \qquad \text{(Equation 3.8)}$$

where E_t is trap energy from the band edge, ω is angular frequency, ν_0 is jump attempting frequency of electrons in materials[o].

Free carriers in a conduction or valence band and carriers in trap states can be distinguished by their frequency responses. Under high-frequency modulation, only free carriers in conductive states contribute to the capacitance, because carriers do not have enough time to interact significantly with trap states. By contrast, in the low-frequency regime, carriers do have enough time to occupy and de-trap from sub-bandgap states, so both conductive and trap states contribute to the capacitance. The threshold frequency where carriers start interacting with trap states is determined by the characteristic energy level of the trap states and the temperature as described in Equation 3.8.[79]

[o] In case of hole traps, $\nu = \nu_0 T^2 = N_v(T) < v > \sigma_h$ is the thermal emission prefactor, where $N_v(T)$ is effective density of states in valence band, <v> is average thermal velocity, and σ_h is capture cross-section of states.

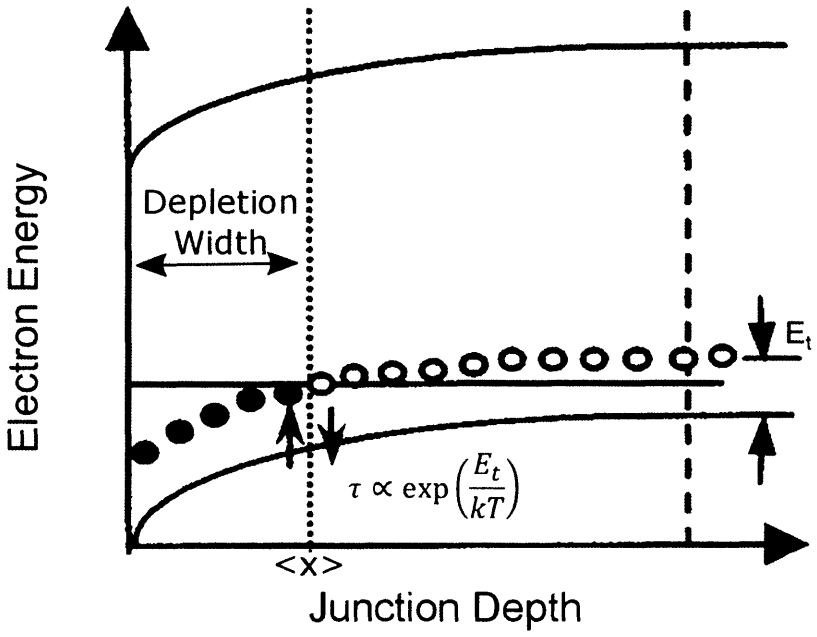

Figure 3-7. Schematic diagram showing trap response at <x> to the AC modulation. Image adopted from Ref: [79]

The measurement scheme for DLCP technique is different from that of the standard C-V measurements. While varying the amplitude of the AC modulation (V_{ac}), the DC bias (V_{dc}) is simultaneously adjusted so that the maximum applied voltage, $V=V_{ac}+V_{dc}$, stays constant (Figure 3-8), thus, the measurement position <x> remains same. The capacitance is measured in a range of frequencies to identify different states by analyzing the frequency response of states. Typical measurement results (C *vs.* V_{ac}) from different frequencies are shown in Figure 3-9.

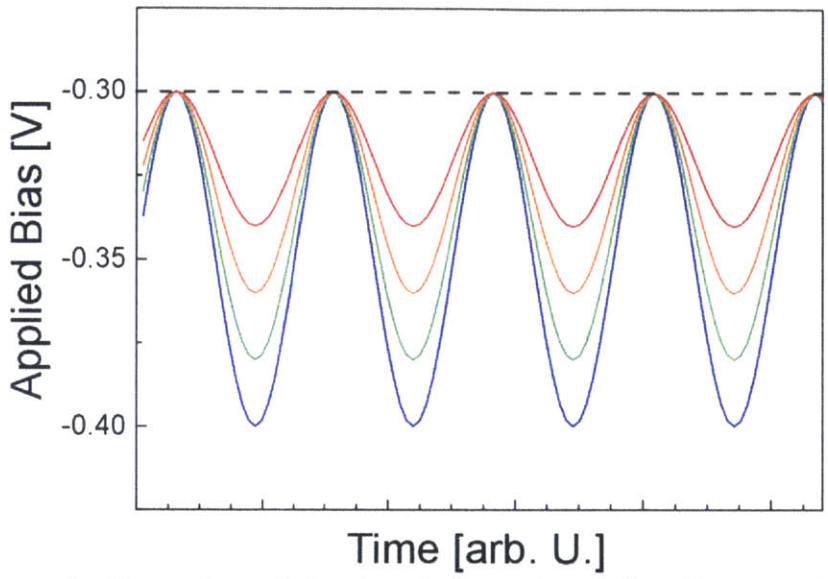

Figure 3-8. Schematic illustration of the description of applying bias. DC bias and AC amplitude must be adjusted together to keep the position <x> same throughout the DLCP measurement. Image reproduced from: [79]

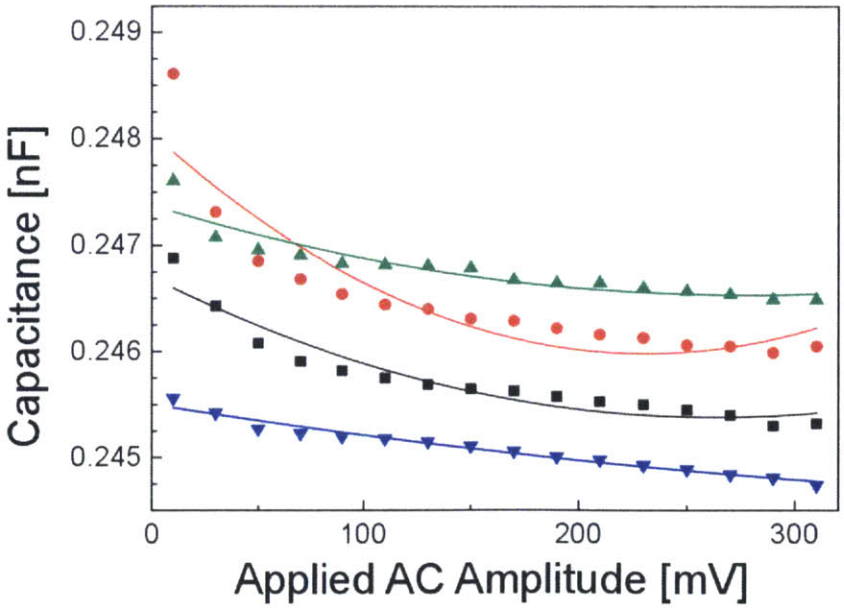

Figure 3-9. Results of DLCP measurement: Raw data (point) and quadratic fitting (line) to extract coefficient C_0 and C_1. Each color represents different measurement frequencies.

In DLCP, the charge response to voltage is not linear, and Equation 3.1 is no longer valid. The non-linear component of charge response becomes significant because the AC amplitude used in DLCP is not negligible compared to the DC bias. In contrast, the amplitude of AC modulation is much smaller for the standard C-V measurements. The non-linear charge (Q)–voltage (V) relation can be expressed by Equation 3.9.

$$\frac{dQ}{dV} = C_0 + C_1 dV + C_2 (dV)^2 + \cdots \qquad \text{(Equation 3.9)}$$

The change of depletion width (δx) induced by the bias modulation (dV or δV) can be derived by applying the Gauss' law to a Schottky junction (Equation 3.10).[79] The Taylor's series for Equation 3.10 is expressed as Equation 3.11.

$$\delta x = \left(\frac{\varepsilon_r \varepsilon_0}{\rho_e} F_E - x_d\right)\left[1 - \sqrt{1 + \frac{2\rho_e \varepsilon_r \varepsilon_0 \, \delta V}{(\varepsilon_r \varepsilon_0 F_E - \rho_e x_d)^2}}\right] \qquad \text{(Equation 3.10)}$$

$$\delta x \approx \frac{\varepsilon_r \varepsilon_0}{(\varepsilon_r \varepsilon_0 F_E - \rho_e x_d)} \delta V - \frac{\rho_e (\varepsilon_r \varepsilon_0)^2}{2(\varepsilon_r \varepsilon_0 F_E - \rho_e x_d)^3} \delta V^2 + \cdots \qquad \text{(Equation 3.11)}$$

In these equations, F_E is electric field and ρ_e is charge density at <x>.

Using Equation 3.11, δQ/δV can be written as:

$$\frac{\delta Q}{\delta V} = \frac{A \rho_e \delta x}{\delta V} = \frac{A \rho_e \varepsilon_r \varepsilon_0}{(\varepsilon_r \varepsilon_0 F_E - \rho_e x_d)} \delta V - \frac{A \rho_e^2 (\varepsilon_r \varepsilon_0)^2}{2(\varepsilon_r \varepsilon_0 F_E - \rho_e x_d)^3} \delta V^2 + \cdots \qquad \text{(Equation 3.12)}$$

By comparing Equation 3.9 and 3.12, we determine C_0 and C_1 as following:

$$C_0 = \frac{A|\rho_e|\varepsilon_r \varepsilon_0}{(\varepsilon_r \varepsilon_0 F_E + |\rho_e| x_d)} \qquad \text{(Equation 3.13)}$$

$$C_1 = -\frac{A \rho_e^2 (\varepsilon_r \varepsilon_0)^2}{(\varepsilon_r \varepsilon_0 F_E + |\rho_e| x_d)^3} \qquad \text{(Equation 3.14)}$$

Drive-level density of states (N_{DL}) can now be expressed using C_0 and C_1.

$$N_{DL} = \frac{|\rho_e|}{q} = -\frac{C_0^3}{2q\varepsilon A^2 C_1} \quad \text{(Equation 3.15)}$$

The position <x> in junction depth is determined by the maximum applied voltage ($V_{ac}+V_{dc}$, the dashed line in Figure 3-8). Of note, <x> is different from the depletion width x_d, and is defined as:

$$< x > = \frac{\int_0^\infty x\, \delta\rho(x)dx}{\int_0^\infty \delta\rho(x)dx} \quad \text{(Equation 3.16)}$$

From Equation 3.2 and 3.13, <x> is expressed as following:

$$< x >= \frac{\varepsilon_r \varepsilon_0 A}{C_0} \quad \text{(Equation 3.17)}$$

Therefore, the depth profile of trap densities can be created from C_0 obtained from different the maximum applied voltage.

The DLCP technique is demonstrated in QD thin films. The density and characteristic energy of trap states in 1,3-benzenedithiol (BDT)-treated PbS QD thin films are measured before and after air-annealing at 100 °C for 30 min. Air-annealing causes oxidation of PbS QDs. Calcium (Ca) and gold (Au) are used as top- and bottom-electrodes, respectively. These samples have similar density of states, $1\text{x}10^{17}$ cm^{-3}, and free carrier densities, $3\text{x}10^{15}$ cm^{-3}, as shown in Figure 3-10. The frequency dependence of N_{DL}, however, is different for two samples. In the oxidized sample, N_{DL} starts to decrease at the lower frequency than in the regular sample. This result indicates that the energy of trap states is shallower for the oxidized sample (Equation 3.8). The DLCP measurements from different temperatures and frequencies yield jump attempting coefficient, v_0, which was introduced in Equation 3.8. The extracted value for v_0 is 6.3×10^4 and this value is consistent with the previously reported value using transient admittance spectroscopy (TAS).[81] The characteristic energy (density-weighted average of energy of each trap states) for traps is calculated using v_0 and

Equation 3.8 (Figure 3-11). As expected in the frequency response, trap energy becomes shallower after oxidation.

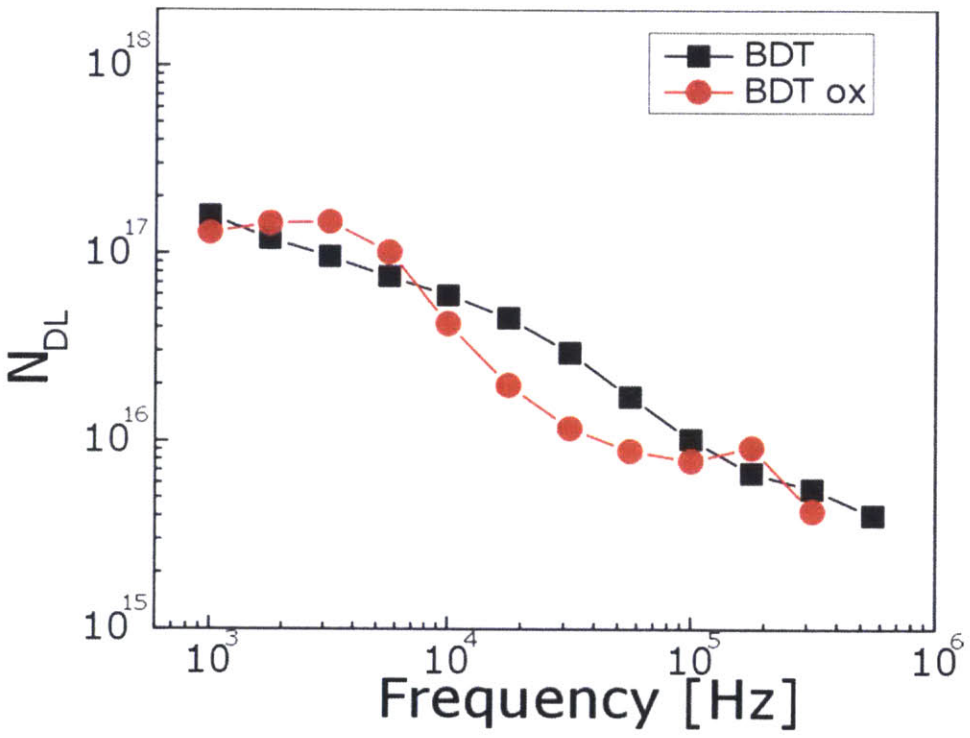

Figure 3-10. Density of drive-level states (N_{DL}) *vs.* frequency for BDT treated PbS QDs before and after oxidation by annealing at 80 °C in air.

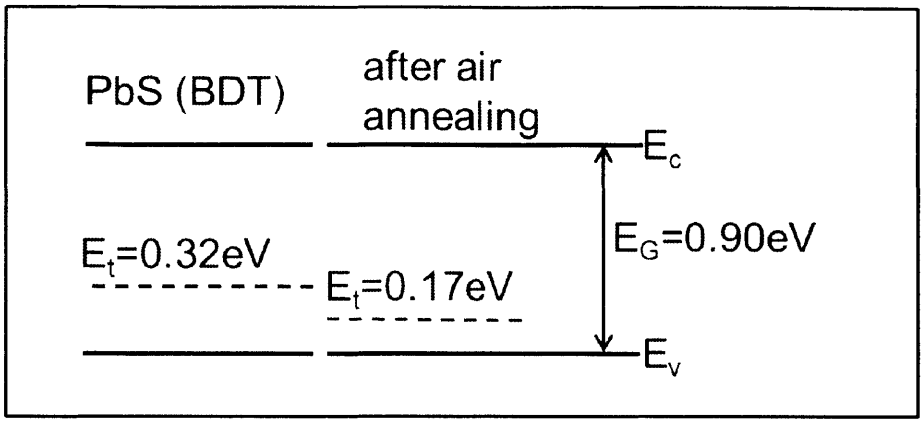

Figure 3-11. Energy of trap states in BDT-treated PbS QD thin films before and after oxidation.

3.4 Summary

In this chapter, I show that the capacitance-based techniques can be used to characterize fundamental electrical properties of QD thin films as they do in conventional semiconductors. I also reviewed the equations for calculating the density of carriers and traps, and their energy distribution inside the band gap from the capacitance measurements. With these techniques, the carrier density and mobility of PbS core-only and PbS/CdS core/shell QD thin films are further analyzed. These results lead to a better understanding of the QD-LED results discussed in Chapter 2. I also introduce DLCP techniques enabling the analysis trap states in QD thin films.

Chapter 4

Chemical Origin of Trap States

Identifying and Elimination of Trap states induced by ligand exchanges

4.1 Motivation

QDs have been actively explored for applications as light emitting diodes,[32,33] photodetectors,[30,44,84] an d photovoltaics.[26,45,85,86] However, further improvements in device performance are required to make them competitive.[73,74,86–89] One well-known factor that presently limits the device performance of QD thin films is sub-bandgap states, also referred to as trap states.[74,89–91] These states, for instance, are thought to give rise to the open-circuit voltage deficit in photovoltaic applications,[92,93] and cause a drastic decrease of charge carrier lifetimes and diffusion lengths.[87,89,94] A common view is that trap states are sub-bandgap surface states caused by dangling bonds or unpassivated surface atoms.[75,88,90,95,96] Thus, previous approaches to reduce the density of traps have included attempts to exchange the binding groups of passivating ligands,[85,88,96] increase the ligand coverage,[88,97] or balance the stoichiometry at the dot surfaces.[98] Recently, Carey *et al.* demonstrated that sub-bandgap emission from PbS QD films treated with 3-mercaptopropionic acid (MPA) can be removed by further treatment with acidic solutions, especially pyruvic acid.[91] Even though these treatments led to improved device

performance, the lack of a fundamental understanding of the mechanism impaired efforts to control trap states in general and, thereby, improve device performance.

In this chapter, chemically reduced (or under-charged) Pb atoms is identified as a chemical origin of trap states in ligand-exchanged PbS QD thin films using X-ray photoelectron spectroscopy (XPS) and density functional theory (DFT) calculations. We then use chemical oxidation to achieve a 40-fold reduction in the density of trap states by controlling the oxidation states of Pb atoms. Our discovery of a chemical origin for the trap states in PbS films offers an opportunity to rationally control their density, and thereby to fabricate improved devices.

4.2 Experiments

Synthesis and fabrication procedures are performed under nitrogen atmosphere using Schlenk line techniques and gloveboxes. OA-capped PbS QDs are synthesized using a method described in Chapter 2, and purified three times by precipitation in a mixture of ethanol and 1-butanol, followed by centrifugation and re-suspension in hexane. OA-capped QD and n-butylamine (nBA) treated QDs are drop-cast to form a film. Solution-phase ligand exchange of nBA is performed by the following steps: After a further precipitation, PbS QDs are dissolved into nBA with a concentration of 25 mg/mL and the solution is stirred overnight. Films are fabricated by drop-casting. QD solutions at a concentration of 50 mg/mL in octane are used for spin-casting. EDT, tetrabutylammonium iodide (TBAI), and MPA treated QD films are prepared by sequential spin-casting. For each layer, 20 μL of QD solution is spin-cast at 1500 rpm for 30 s on a Si substrate. Roughly 0.1 mL of ligand solution is then dispensed onto the substrate, allowed to sit for 30 s, and spun dry. The substrate is then washed with the excess solvent used for ligand exchange and spun dry three times to remove unbound ligands, and the entire process is repeated; each complete iteration results in the deposition of ~20 nm of QDs. The ligand concentrations and solvents

used in this study are EDT 0.02 % (v/v) in acetonitrile, TBAI 10 mg/mL in methanol, and MPA 1 % (v/v) in methanol. For the selected films, the oxidation process is performed between layer depositions. Roughly 0.1 mL of 10 mg/mL 1,4-benzoquinone (BQ) solution in methanol is dispensed onto the ligand-exchanged films, allowed to sit for 30 s, and spun dry followed by three sequential washes with methanol.

PL measurements were conducted at a room temperature with 532nm diode laser excitation. [3.0 mW into a ~135μm spot ($1/e^2$ diameter) for an irradiance of ~150mW/cm^2] The photoluminescence was collected using reflective optics, passed through a long-pass filter (3mm Schott RG780) to remove pump scatter, spectrally dispersed using an Acton 300i spectrometer, and measured using an InGaAs array detector (Roper Scientific). XPS measurements were performed using a PHI Versaprobe II X-ray Photoelectron Spectrometer, and the spectra were analyzed using CasaXPS software. WDS measurements were performed using a JEOL JXA-8200 SuperProbe. DLCP measurement was performed as described in Chapter 3 in a nitrogen-filled glove box.

4.3 Sub-Bandgap Emission and Its Origin

As-synthesized QDs have bulky organic ligands, so it is generally necessary to exchange these with smaller molecules to facilitate charge transport.[44,85,88,99] Typical ligands used for the fabrication of QD devices include: EDT, MPA, TBAI, and nBA. EDT-, MPA-, and TBAI-treated PbS films were prepared by conventional solid-state ligand exchange procedures.[26,73,85–88,96,100] Additionally, nBA-treated samples were prepared by an established solution-phase ligand exchange procedure.[101] As seen in Figure 4-1, photoluminescence (PL) measurements show that additional sub-bandgap emission is observed following every ligand exchange process—independent of the binding group of the ligands. In detail, PbS QDs with native OA ligands (black) show only band edge emission at *ca.* 1050 nm. By contrast, EDT- (blue), TBAI- (green), and nBA- (red) treated

samples show broad, but distinct emission peaks near 1500 nm, 1600 nm, and 1400 nm respectively, and the MPA-treated sample (orange) shows a long red tail. All these additional emissive features reside at lower energies than the band edge emission, which indicates that the newly formed emissive states are located inside the band gap. For the nBA-treated sample, we note that band edge emission near 1100 nm is considerably weaker than the trap emission, while the band edge emission for all ligand-exchanged samples are slightly red-shifted due to the increased dielectric environments and altered diffusion of photoexcitations induced by the shorter dot-to-dot distance.[102–104]

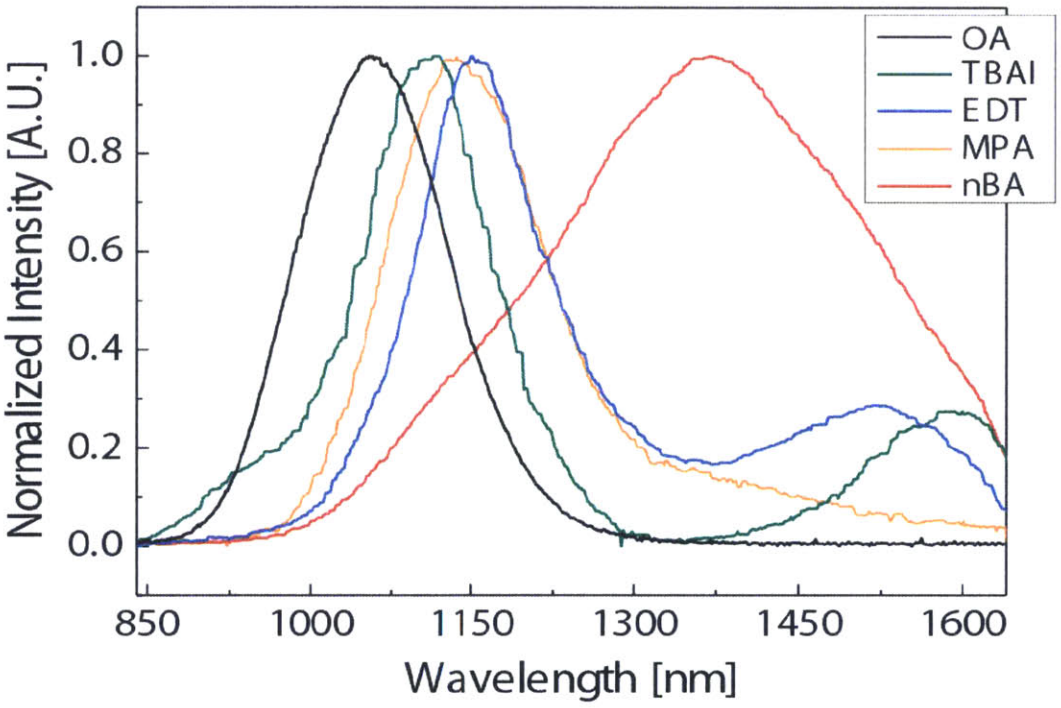

Figure 4-1. PL from PbS QD thin films with different ligands – OA (black), TBAI (green), EDT (blue), MPA (orange), and nBA (red).

To identify whether a chemical species is associated with this trap emission, high-resolution XPS was performed on each film, focusing on the Pb 4f spectral feature to obtain information on the bonding character of the Pb atoms (Figure 4-2) The expected spectral positions for three species[105] are highlighted with colored bands: metallic Pb as tan, Pb-S as blue, and Pb-carboxylate as grey. Peak locations for Pb bonded to other ligands are not explicitly marked since these features are not prominent in our data, and are covered under the tails of Pb-S peaks. Before ligand exchange, the OA-coated film shows a single, relatively broad feature due to the overlap between the two peaks from Pb-S and Pb-carboxylates. The deconvoluted spectrum of the OA-coated QD film is shown in Figure 4-3. PbS QDs ligand-exchanged with different length of dithiol ligands and TBAI-treated PbS QDs from different batch of synthesis by Hines method and $PbCl_2$-method are examined by XPS, and every samples exhibit metallic Pb features in Pb 4f regime as shown in Figure 4-4 and 4-5.

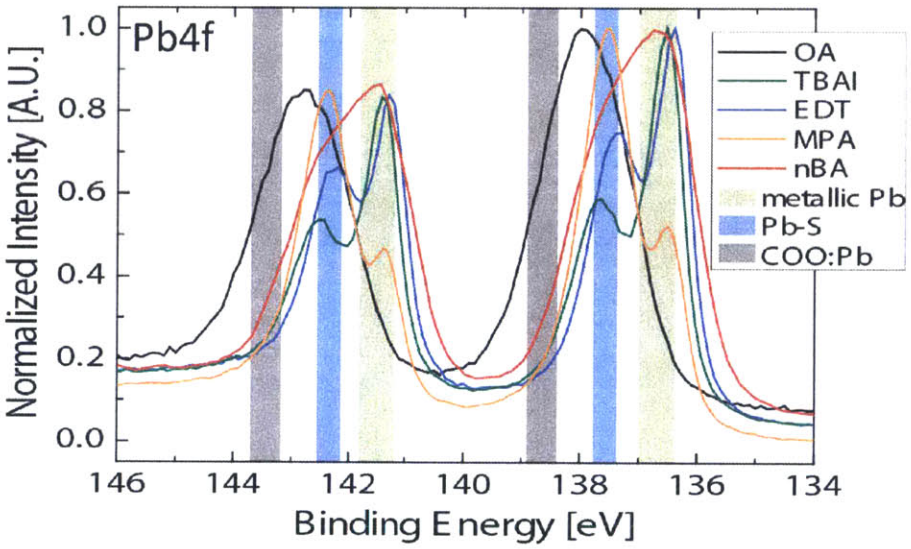

Figure 4-2. XPS on the Pb 4f feature for PbS QD thin films with different ligands – OA (black), TBAI (green), EDT (blue), MPA (orange), and nBA (red). The binding energies of metallic Pb, Pb-S, and COO:Pb are highlighted.

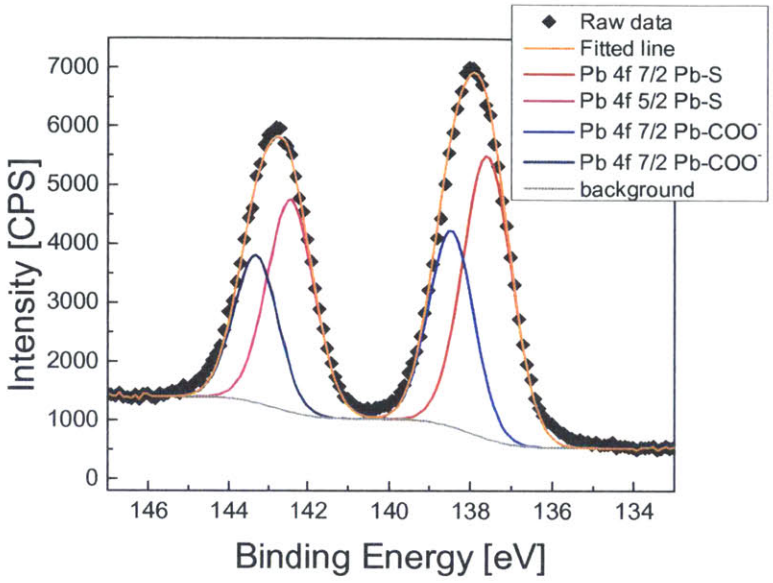

Figure 4-3. The deconvoluted spectrum of PbS QD thin films with native OA ligands. The spectrum is well fitted with the sum of the peaks from Pb-S and Pb-carboxylates.[105]

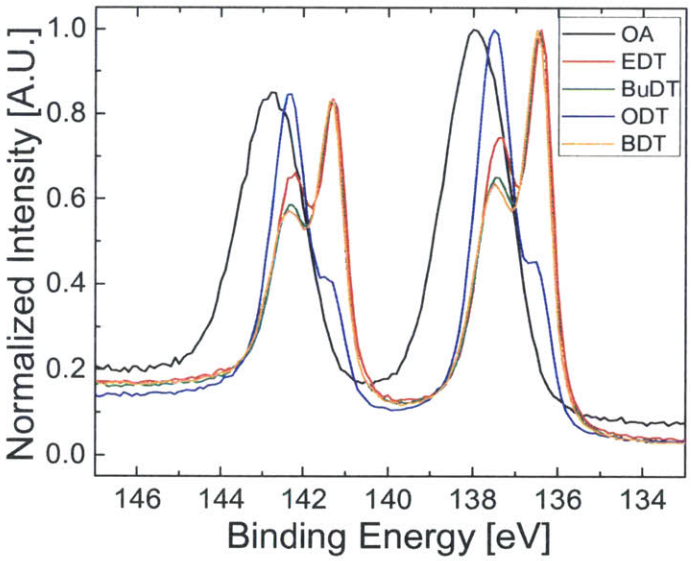

Figure 4-4. The XPS results of PbS QD thin films with different length of dithiol ligands are compared with oleic acid (OA) ligand : 1,2-ethanedithiol (EDT), 1,4-butanedithiol(BuDT), 1,8-octanedithiol(ODT), and 1,3-benzendithiol (BDT). Under-charged Pb atoms exist regardless of the length of dithiol ligands.

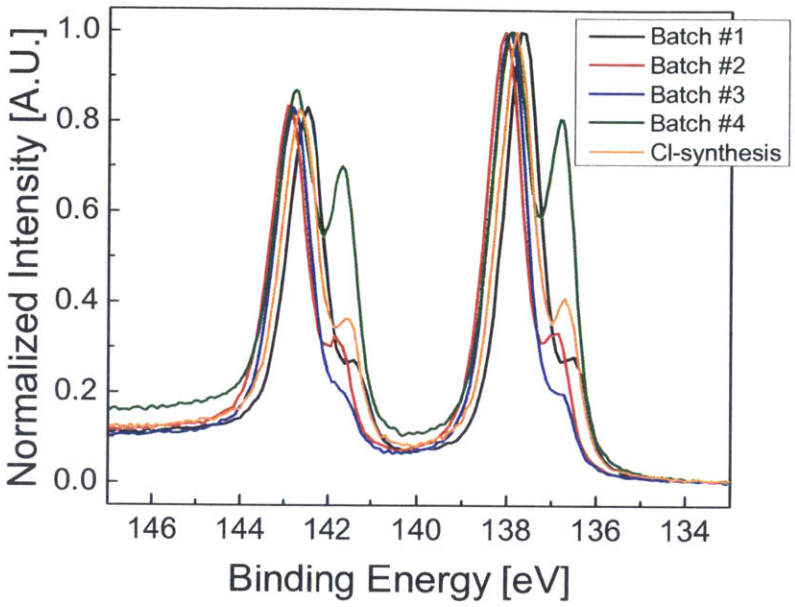

Figure 4-5. XPS results show the under-charged Pb atoms in TBAI-treated PbS QDs result from four different synthetic batches of Hines method and Cl-synthesis.

After ligand exchange, the Pb-carboxylate features are diminished for all samples, and an additional peak is evolved with a lower binding energy than either Pb-S or Pb-carboxylate bonds. The new peak corresponds to the binding energy of metallic Pb,[105] which indicates that a few Pb^{2+} atoms in Pb-S bonds have been chemically reduced to have less charge than regular Pb-S bonds. The consistent trend in our XPS results for each ligand implies that the origin of these additional emissive trap states is reduced or 'under-charged' Pb atoms.

To verify whether the formation of under-charged Pb atoms contributes to the emissive sub-bandgap states, we oxidized the ligand exchanged films with a mild oxidizing agent, BQ. As shown in Figure 4-6, the XPS measurements confirm that the BQ treatment successfully removes the under-charged Pb atoms. Further, after oxidation, all ligand-exchanged PbS QD films exhibit only band edge emission, as shown in Figure 4-7. Additional XPS results shown in Figure 4-8 demonstrate that this effect can be achieved with other oxidation methods, such as pyruvic acid treatment and annealing in air. Of note, after air-annealing

additional oxidation feature of Pb arises at higher binding energy than the Pb-S feature. These results all support a causal relationship between under-charged Pb and emissive trap states.

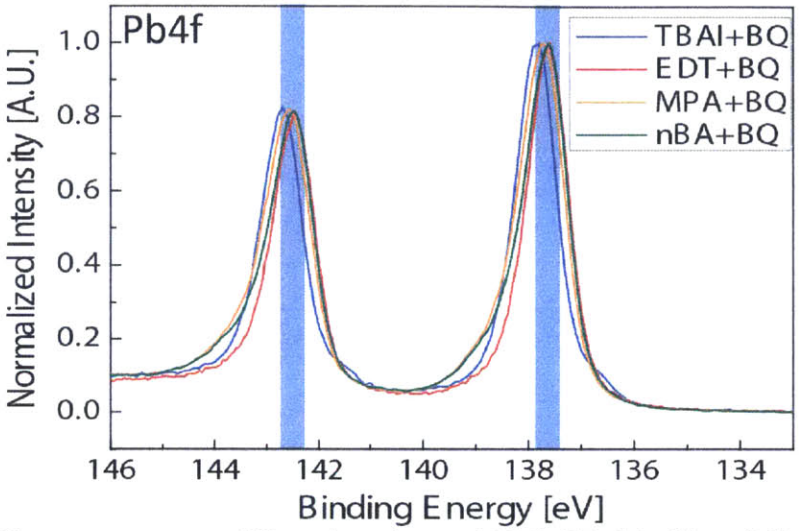

Figure 4-6. XPS measurements of ligand-exchanged PbS QD thin films following oxidation with BQ – OA (black), TBAI (green), EDT (blue), MPA (orange), and nBA (red). The binding energies of Pb-S are highlighted.

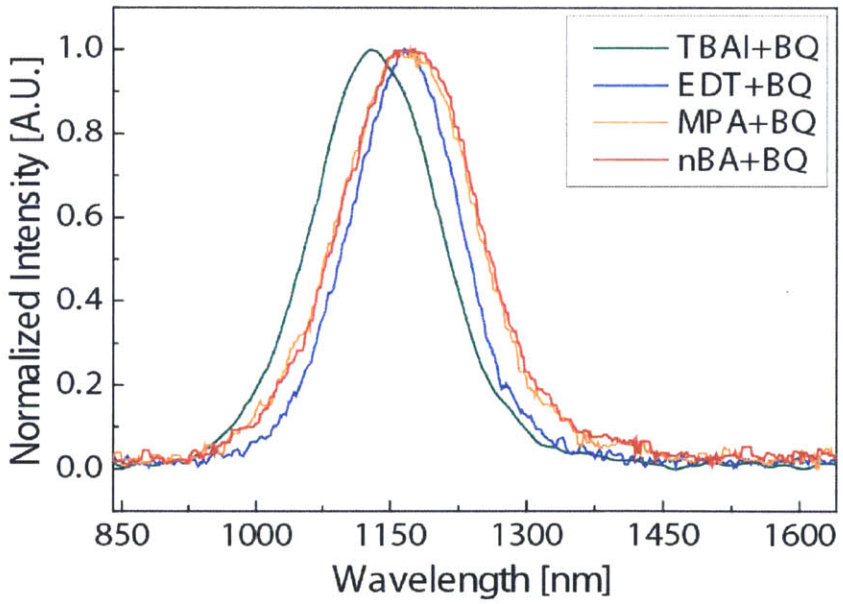

Figure 4-7. PL measurements of ligand-exchanged PbS QD thin films following oxidation with BQ– OA (black), TBAI (green), EDT (blue), MPA (orange), and nBA (red).

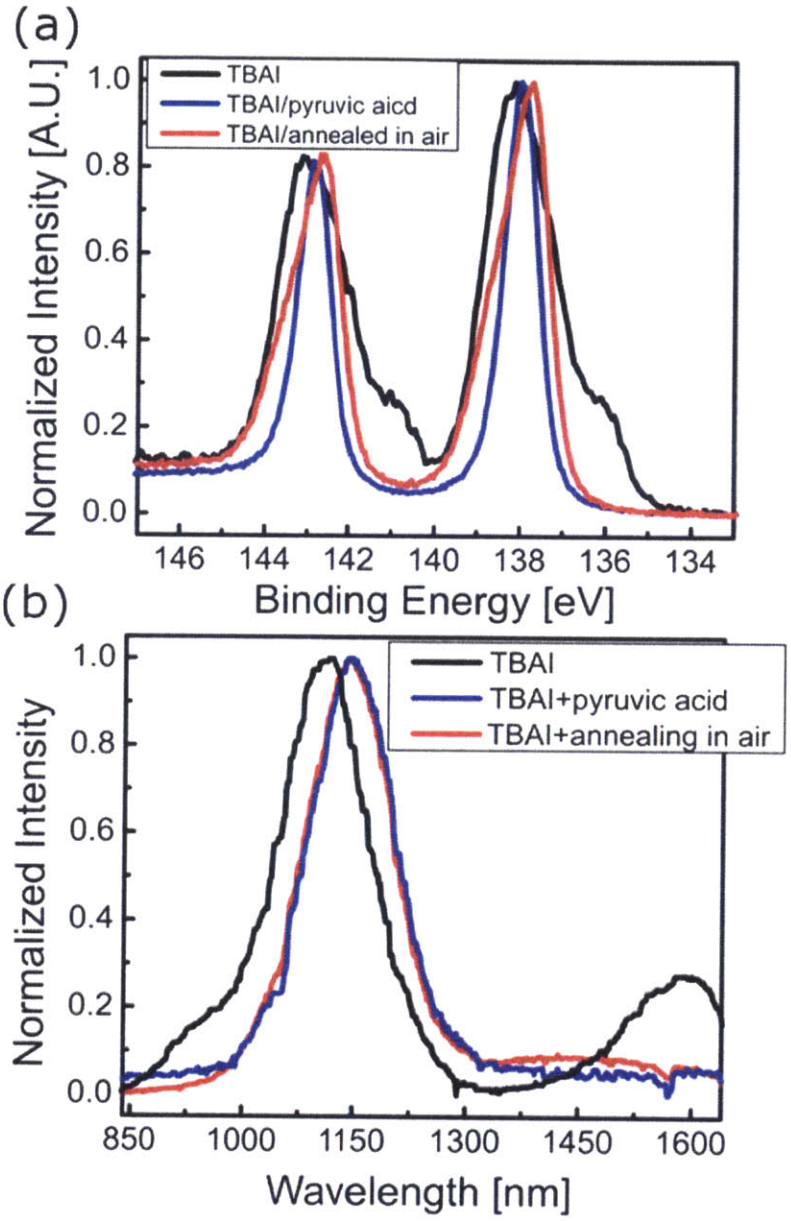

Figure 4-8. (a) The XPS results of TBAI-treated PbS QD thin films with different oxidation methods: TBAI-treated films as a reference (black), TBAI-treated films followed by 0.8 % (v/v) pyruvic acid treatment[91] (blue), which is a well-known oxidant in metabolic pathways in muscles,[106] TBAI-treated films followed by annealing at 80°C in air for 30min (red). Under-charged Pb features at the shoulder of Pb-S peak are disappeared with pyruvic acid treatment and air-annealing. (b) The PL shows that the emission from sub-bandgap states removed after the treatment.

It is important to ensure that the removal of the emissive sub-bandgap states by BQ treatment is not due to an additional ligand exchange or a change in the ligand coverage. Compared to sulfur- and nitrogen-bearing ligands, TBAI-treated PbS QDs have the convenient property that the elemental signature of iodine (I) is readily distinguishable in XPS experiments. As shown in Table 4-1, XPS measurements on TBAI-treated PbS QDs confirm that the I-to-Pb ratio stayed constant after the BQ treatment, which verifies that the ligand binding on QDs is still intact after the BQ treatment. Moreover, benzene-1,4-diol as known as hydaroquinone (HQ), which a product from the reduction of BQ, is tested as ligands. As shown in Figure 4-9, HQ treatments on TBAI-treated QDs has no effects on Pb 4f peak in XPS, and only leads slight increase of O contents in the QD thin films. Thus, these results demonstrate that the changes after BQ treatments are induced by the oxidation not by additional ligands effects.

Table 4-1. The atomic ratios of PbS QDs used in this work. Experimental data for the Pb-to-S ratio is obtained using WDS, and the I-to-Pb in TBAI-treated PbS QD thin films is measured using XPS. The ratios for the simulated QD used in DFT calculations is included for comparison.

Samples	I/Pb ratio	Pb/S ratio
PbS:OA	n.a.	1.58±0.08
PbS:TBAI	0.336 ±0.010	1.51±0.14
PbS:TBAI/BQ	0.353±0.016	1.45±0.04
Simulated PbS QDs	0.302	1.47

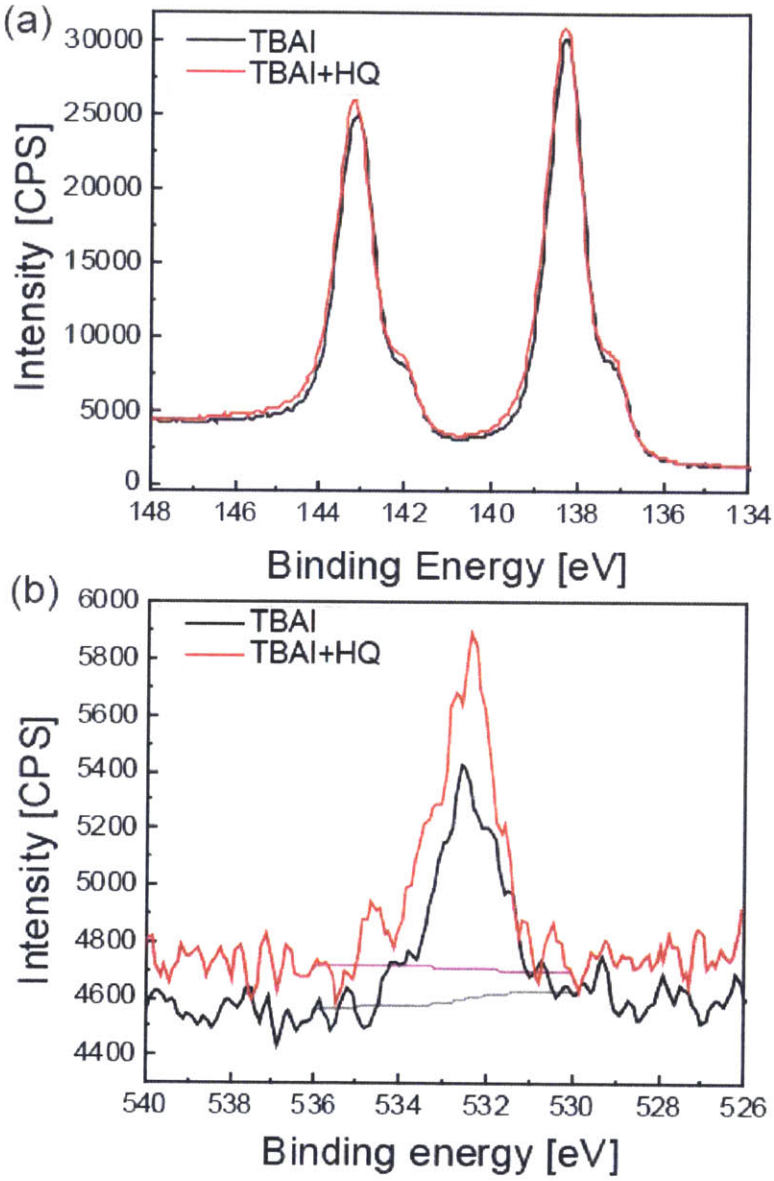

Figure 4-9. XPS results of TBAI-treated samples with and without 1,4-hydroquinone (HQ) treatment. HQ is a product from the reduction of BQ. Minimal change in the spectral features of (a) Pb 4f and (b) O 1s is observed before and after the HQ treatment. This result indicates limited binding of HQ on the QD surface. O-to-Pb ratio with background correction increases 9% after the HQ treatment. We suspect that oxygen in the samples is originated from residual OA ligands or air-exposures during the sample transfer to XPS chamber.

4.4 Theoretical Study

To test the possibility that under-charged Pb atoms can form under these conditions, and give rise to sub-bandgap states, we calculate the electronic structure of a PbS QD using DFT. DFT calculations were performed using the Vienna Ab initio Simulation Packages (VASP)[107] with the generalized gradient approximation of Perdew–Burke–Ernzerhof (PBE)[108] for the exchange and correlation functional. The projector-augmented-wave method was adopted to describe the core electrons. An energy cutoff of 400 eV and a Monkhorst–Pack k–point sampling of $1 \times 1 \times 1$ were used. A large vacuum spacing of > 15 Å was used to prevent spurious inter-QD interactions. PbS QDs bearing iodine ligand were fully relaxed using the conjugate gradient method until the structure satisfied the following relaxation criteria: (i) the energy difference between two consecutive ionic steps is less than 10^{-4} eV, and (ii) the maximum Hellmann-Feynman forces acting on each atom are less than 0.01 $eV \cdot Å^{-1}$. Bader charge analysis was post-performed on charge density results obtained from DFT in order to calculate local charge that each atom in a QD possess.[109]

For the study, we construct a model QD based on the elemental composition of TBAI-treated QDs, which is measured by WDS and XPS (Table 4-1). The Pb-to-S ratio determines the proportion between stoichiometric (100) facets and Pb-terminated (111) facets in a truncated octahedron shape. The final QD used for simulations is 1.95 nm in diameter and consists of 116 Pb atoms, 79 S atoms, and 35 I atoms (Figure 4-10). We focus on QDs with iodide (I^-) ligands as they are used in modern, high-performance photovoltaic devices,[86] and the simple structure reduces the computational burden, allowing the simulation of larger QDs.

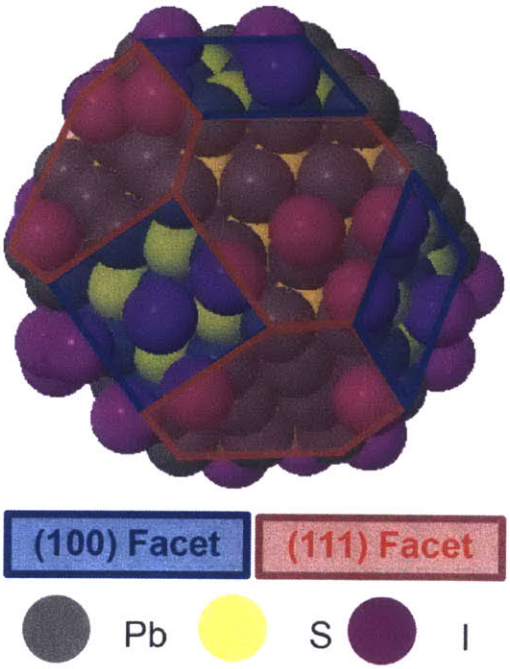

Figure 4-10. The truncated octahedron shape of the model PbS QD used for the DFT calculations.

Using this model QD, a Bader charge analysis on the DFT calculation shows the existence of the under-charged Pb atoms. Bader charge analysis is a post-processing method which can partition the continuous charge density along the whole system obtained from DFT so that local charges of individual atoms can be determined.[109] Figure 4-11 shows the charge distribution—*i.e.* the atom population density *vs.* local charge—of each atomic species in the constructed NC. For Pb atoms, a major peak in population density is observed at +0.90 (in units of electron charge) with weaker, broader features at lower levels of charge (+0.4–0.75). These broad features in lower ranges indicate the existence of stable, under-charged Pb atoms, which is consistent with our experimental observations using XPS. In comparison, the S atoms and I atoms have single, narrow peaks at −0.90 and at −0.5 electron charges, respectively. We note that these values are less than the formal valence charge because the bonds have mixed covalent/ionic nature. For example, as shown in Figure 4-12, Pb and S atoms in PbS bulk possess a local charge of about +0.95 and −0.95, respectively.

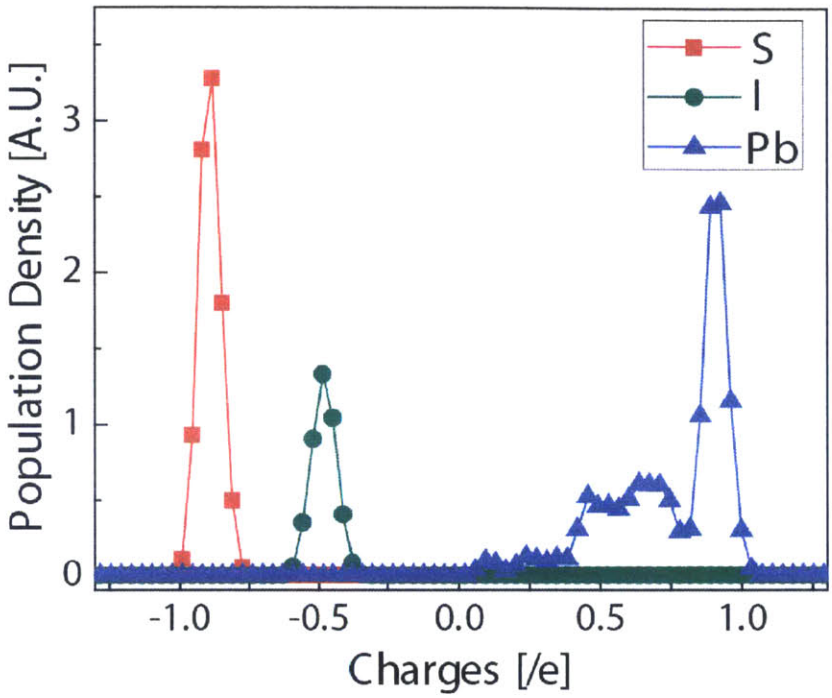

Figure 4-11. Bader charge analysis gives the charge distribution for each element—Pb (blue), S(red) and I (green).

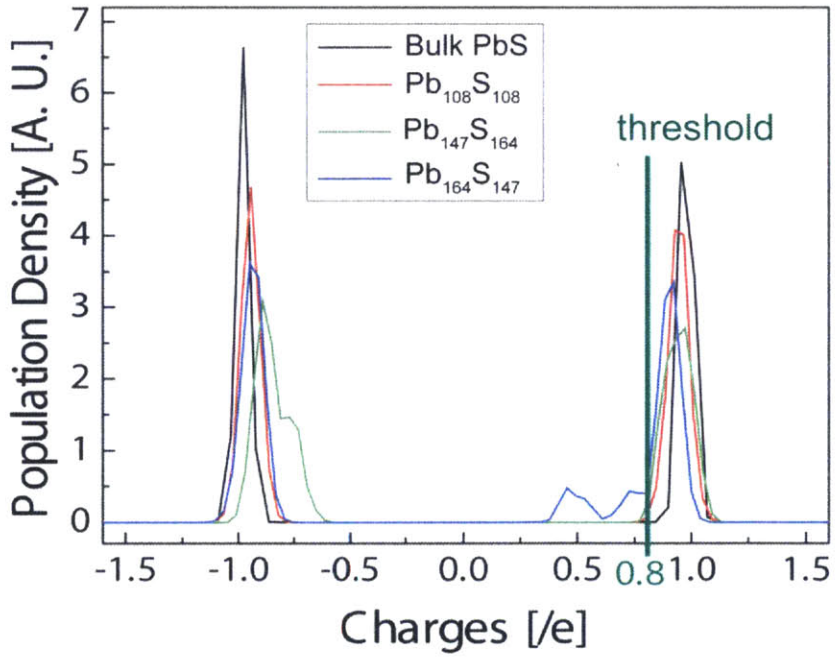

Figure 4-12. The simulated charge distribution of different Pb-to-S ratio samples to show that the level of charge threshold for under-charged Pb species is 0.8.

Figure 4-13 (a) and (b) show the density of states (DoS) for our model QD calculated using DFT. The total DoS (black) reflects all available electronic states, and is broken down into a projected density of states (PDoS) for each atomic species, S (orange), I (purple), and Pb (blue). The PDoS of Pb atoms is further subdivided into contributions from regular-charged (green) and under-charged Pb atoms (red). We define under-charged Pb atoms as those having a charge less than 0.8 electron charges. This threshold value was suggested by the profile of the atomic population density for Pb in Figure 4-11, and supported by additional Bader charge calculations that showed that neither bulk PbS, nor stoichiometric and sulfur-rich QDs have features in this region (Figure 4-12). Returning the PDoS in Figure 4-13 (b), it is clear that the density of states inside the bandgap arises overwhelmingly from under-charged Pb atoms (< 0.8), which is in good agreement with our conclusions from the PL and XPS results shown in the previous section. This is an important refinement over a simple 'dangling bond' picture. Additional calculations (Figure 4-14) on 'bare' QDs—where all surface Pb atoms have dangling bonds—show that only Pb atoms on (111) surfaces are under-charged and contribute to sub-bandgap states, while Pb atoms on (100) surface are not under-charged and do not contribute to sub-bandgap states.

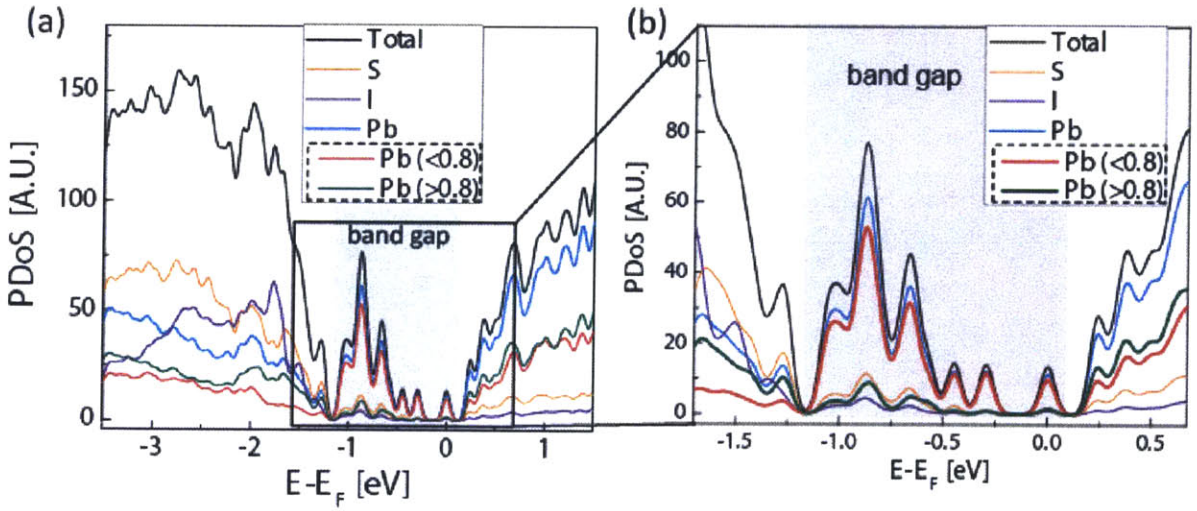

Figure 4-13. (a) The DoS (total, black) from DFT, broken into PDoS for each chemical species—S (orange), I (purple), all Pb (blue). The PDoS of Pb further subdivided—contributions from under-charged Pb atoms (<0.8, red), and Pb atoms with a charge greater than 0.8 (green). (b) An enlarged view of (a) highlighting the DoS near the band gap.

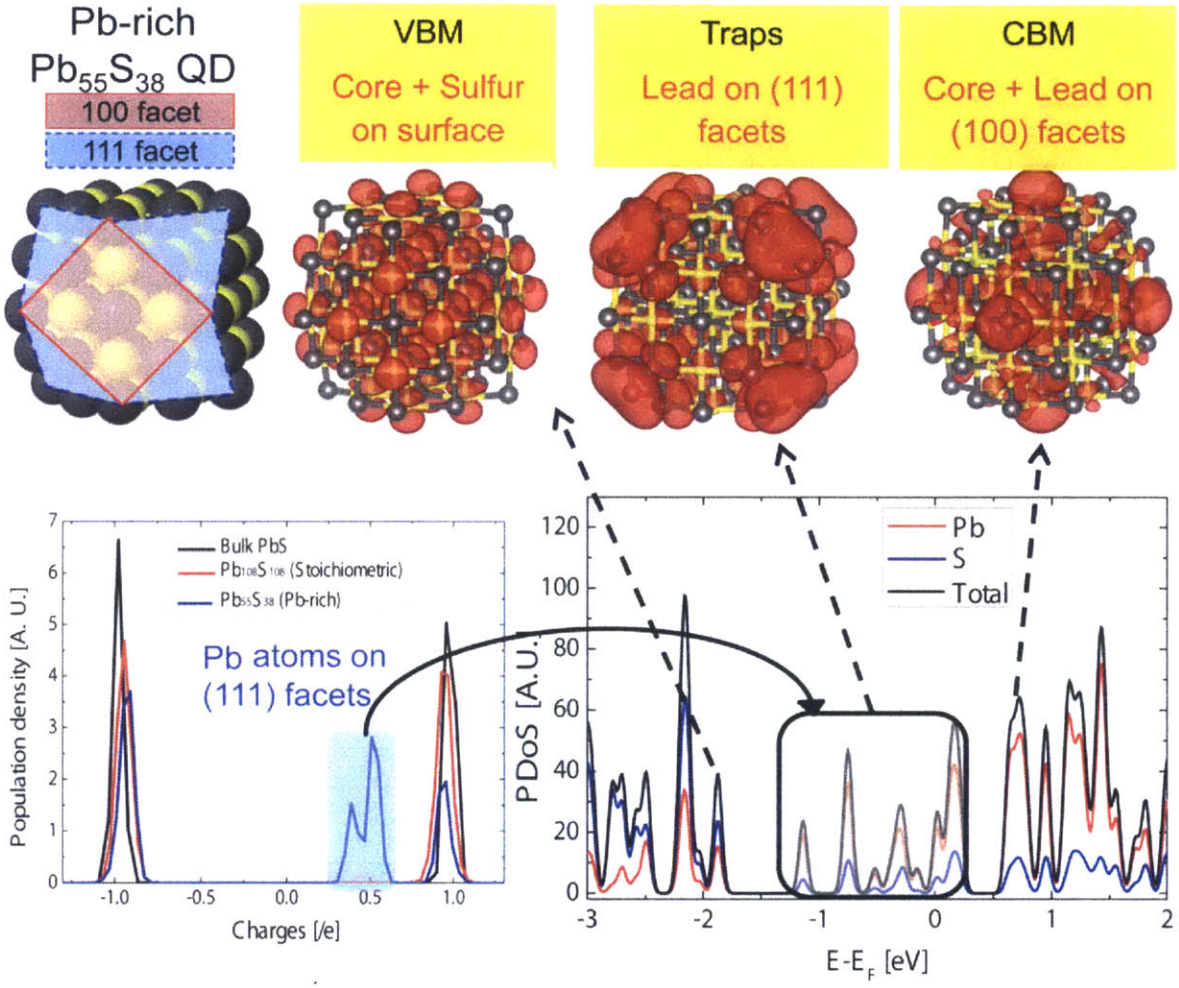

Figure 4-14. The DFT results shows that under-charged Pb species are located on the (111) facet, and induce sub-bandgap states.

Our calculations allow us to investigate the effect of ligands on the electronic structure of off-stoichiometric (lead-rich) PbS QDs, and provide a fundamental explanation of previous approaches to control trap states with ligand treatments.[88,94–96,98,100] As we (Table 4-1) and others[9,66] have shown, as-synthesized PbS QDs tend to be lead-rich. The excess Pb atoms are located on the off-stoichiometric (111) surface, and calculations on bare (ligand-free) QDs show that overall charge balance is maintained by the under-charged Pb atoms.

However, as shown in Figure 4-15, the addition of I^- ligands decreases the number of under-charged Pb atoms by contributing partial negative charge. This is consistent with a previous theoretical study that indicates that the level of the suppression depends on ligand coverage.[97] However, we note that this cancellation is not expected to be exact under most conditions used in device fabrications.[86,91,92,98] Instead, because the electronegativity of the binding groups determines the amount of partial charge that can be donated, different types of ligands are expected to yield different levels of suppression (Figure 4-16 (a)) and a different profile of sub-bandgap states (Figure 4-16 (b)). This provides a rationale for the many studies showing that ligands affect the electronic structure and Fermi level of QD thin films.[97,100,110–113]

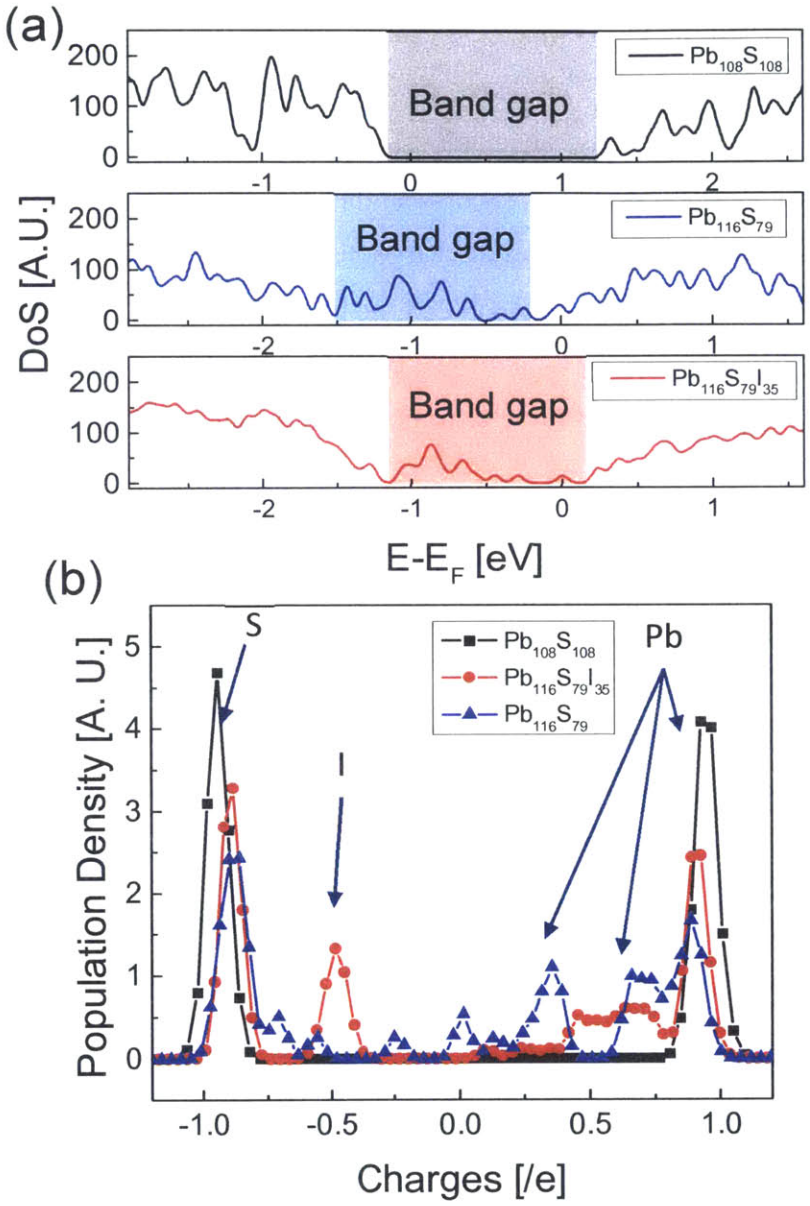

Figure 4-15. (a) DoS and (b) Bader analysis for the comparison of bare QDs and iodine passivated QDs. I^- ligands suppress under-charged Pb species, and sub-bandgap states in off-stoichiometric PbS QDs. As a reference, calculations on stoichiometric QDs show no sub-bandgap states and no reduced Pb atoms.

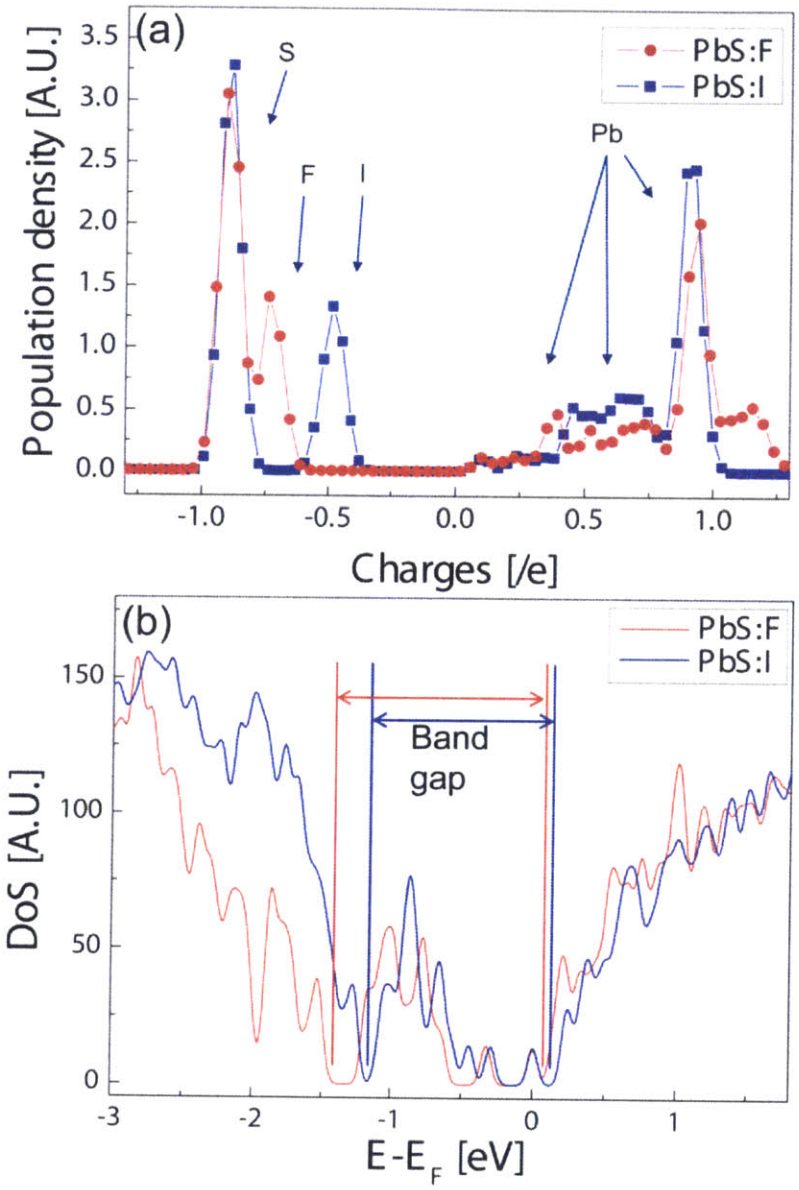

Figure 4-16. DFT results show that I^- and fluoride (F^-) ligands induce different suppression of under-charged Pb species and a different profile of sub-bandgap states.

4.5 Effect of Oxidation

Density of trap states are electrically measured by DLCP to demonstrate that BQ treatment effectively removes electrically-active trap states, and does not simply suppress the spectroscopically-observed trap emission by causing the trap states to become wholly non-radiative.[73,75,81] As described in Chapter 3, conductive and trap states can be distinguished by their frequency responses in DLCP.

The structure of Schottky diodes used in the DLCP measurement is shown in Figure 4-17. We compare density of trap states of EDT-treated PbS QD films with and without BQ treatment, and present our results in Figure 4-18. Prior to BQ treatment, we observe that there is a much greater density of available states at low modulation frequencies compared to the high-frequency regime, which is consistent with the presence of trap states. We find that the absolute density of trap states is 4.8×10^{16} cm^{-3} ($\sim 2.7 \times 10^{-3}$/dot), which is in agreement with values measured using other methods.[73,81] After oxidation, we observe that the low-frequency feature is strongly diminished, and our analysis shows a 40-fold decrease of trap density to 1.2×10^{15} cm^{-3}—a level of suppression that is expected to yield a 6-fold improvement in the carrier diffusion length.[89] Therefore, we conclude not only that oxidation by BQ effectively reduces the density of trap states, but also that the emissive sub-bandgap states induced by ligand exchange are electrically active. Further, we rule out the alternative explanation that oxidation by BQ only suppresses trap emission by rendering the states totally non-radiative—the DLCP results show that the sub-bandgap states have been removed.

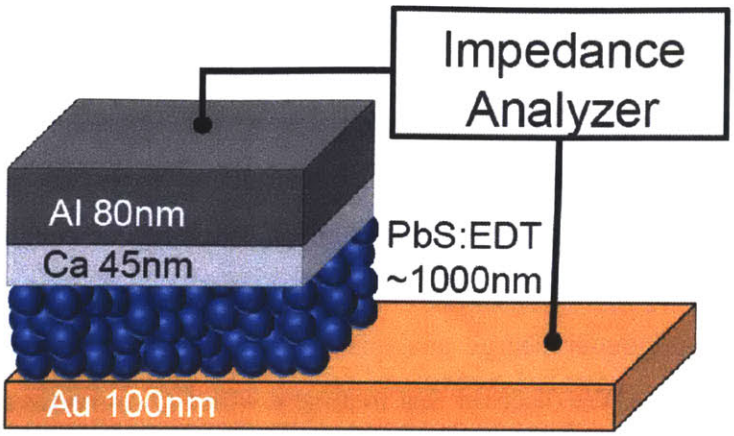

Figure 4-17. A schematic of the Schottky diodes used for the DLCP measurements

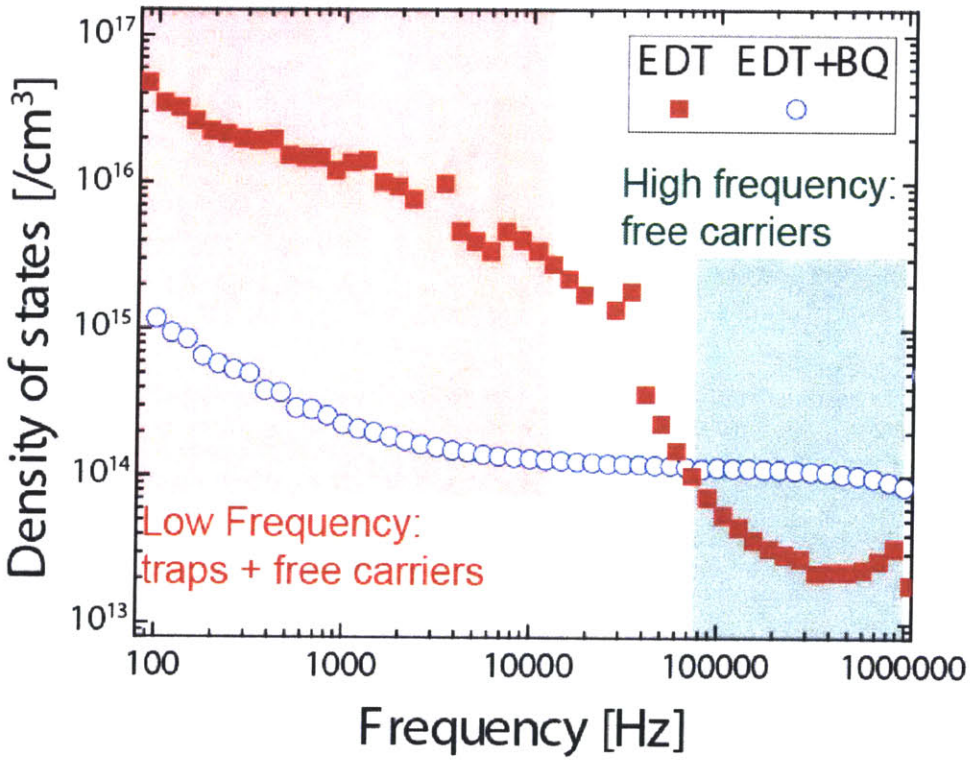

Figure 4-18. DLCP measurement of the density of states of EDT-treated PbS films with and without the BQ treatment. The low frequency regime (red box) includes contributions from carriers interacting with conductive and trap states, while the high frequency regime (green box) gives the density of conductive states only.

4.6 Summary

In this chapter, we have identified the chemical origin of sub-bandgap states in ligand exchanged PbS QD thin films using a combined experimental/theoretical approach. We show experimentally that under-charged Pb atoms result from ligand exchange, and are associated with sub-bandgap states that are both optically and electrically active. Theoretical calculations using DFT and Bader charge analysis confirm that under-charged Pb atoms give rise to sub-bandgap states. We discover that treatment with BQ re-oxidizes these under-charged Pb atoms and suppresses trap emission, and then use DLCP to show quantitatively that it achieves 40-fold decrease in the density of trap states. We expect that insights developed in this paper on the fundamental origin of trap formation will provide directionfor controlling the density of trap states in thin films of QDs, and thereby improve the performance of QD devices.

Chapter 5

Conclusion and Future Outlook

Colloidal PbS QDs have potentials for optical and electrical applications, because of their unique properties such as the tunable band gap and relative high QY in NIR and SWIR, low-cost synthesis, and process-compatibility to Si technology. Their development is mainly driven by the interest in QD photovoltaics, while their high QY in IR makes them still attractive in other applications such as optical communications and bio-imaging. However, PbS QD devices suffers inferior device performance due to the surface trap states in QDs. The trap states impair the device performance as well as optical properties. The researches described in this thesis pursue to design rationales for passivating trap states on the QD surfaces.

The first approach is passivating the dangling bonds on PbS QD surfaces with inorganic CdS shell layers. This method helps to improve QY and protect QDs from external environmetns, but CdS shell layers degrade the electrical conductivity severely by decreasing both carrier concentration and moblity. The potential as a bright SWIR fluorophore is investigated in fluorescent deep-tissue bio-imaging. To minimize the degradation of electrical conductivity, the shell growth condition is modified to enable a monolayer-thickness control. The QDs with a monolayer-thick CdS shell exhibit still improved optical properties and environmental stability comparable to thicker shell QDs and better electrical conductivity due to higher carrier concentration. The IR QD-LEDs

using a thin-shell PbS/CdS QDs demonstrate the twice higher EQE in SWIR than any previous reported devices because the CdS shell provide excellent protection from the degradation of QD surfaces during device fabrications.

To find another solution without degrading the electrical properties of QD thin films, specific chemical origins of trap states need to be identified, and proper electrical characterization for traps in QD thin films is required. Capacitance-based techniques are introduced as complementary techniques with charge transport-based techniques. Using Nyquist plots, dielectric constants and an impedance analyzing model for further analysis can be easily determined. Mott-Schottky measurement provides information about carrier concentration, and the mobility also can be calculated by combining this result with conductivity measurements. DLCP is a key technique to analyze traps in QD thin films electrically. DCLP provides fundamental information about traps, such as their density, characteristic energy, and depth-profile in the junction.

Then, the origin of trap states is identified to design a rationale to suppress trap states with combination of electrical, optical, chemical and theoretical techniques. Optical and electrical characterization reveal the formation of trap states in QD thin films after ligand exchanges for device fabrication. XPS demonstrates the presence of under-charged Pb atoms in ligand-exchanged QD thin films, which is predicted by DFT. Moreover, the DFT calculation illustrates the contribution of under-charged Pb atoms to the trap states. The density of trap states is reduced by a factor of 40 with removing under-charged Pb atoms by oxidation.

During the past decades, the development of PbS QD synthesis and post-treatment methods has been driven for improving efficiency of photovoltaics. Over 9 % of power conversion efficiency (PCE) is achieved by several advances such as improving the size distribution in synthesis and discovering the role of halides for surface passivation.[18,21,22,86] However, further improvements requires for utilizing knowledge from device physics to design a rationale such as engineering band alignment.[86]

Device physics can model the behavior of devices when the electrical properties of materials are well characterized. However, the influence of chemical treatment to electrical properties of QDs is not predictable. The black box between chemical treatments and electrical properties of QD thin films could be revealed through more thorough electrical and chemical characterization of QD thin films. Theoretical calculation also provides insight to connect chemical treatment and electrical properties of QDs.

A detailed understanding of electrical properties of QD thin films increases predictability of QD device behavior, and eventually allows us to design a rational model to customize the QD properties for each application.

Appendix A

Self-Assembly Binary Nanocrystal Superlattice

A.1 Motivation

Self-assembly process is of great interest as a key process for bottom-up fabrication in nanotechnology.[114–116] A well-designed periodic pattern from nano-scale self-assembly has potential as a mask in nanolithography.[117] Here, we attempt to utilize self-assembly binary nanocrystal superlattice (BNSL) of QDs as an active layer in QD-LEDs and use these devices for EQE drooping studies.

We speculate that a major reason for EQE drooping in QD-LEDs is Auger recombination.[118] This problem can be avoided by separating light-emitting QDs and the materials for charge injection and transport in the active layer. We adopt this concept into QD-LEDs using BNSL of QDs as an active layer. In our design, charges are not directly injected into light-emitting QDs; instead, energy for emission is delivered by Förster resonance energy transfer (FRET). We choose PbS/CdS core/shell QDs for light-emitting QDs because CdS shell is expected to be a barrier for charge injection and Auger ionization. The second component of BNSL is CdSe/CdZnS core/shell QDs, which are used for charge transport because they have high QY. High QY indicates a minimal non-radiative decay, which prevents efficient FRET to PbS/CdS QDs. Metal NCs cannot be used as a charge transport component, because they quench the exciton of adjacent QDs.

A.2 Preparation

8-nm CdSe/CdZnS QDs (C-QDs) and 4-nm PbS/CdS QDs (P-QDs) are prepared. Including the ligand length, their size ratio (γ) is estimated to be 0.55–0.60. Helmholtz free energy, a driving force for self-assembly BNSLs, is minimized when the space filling ratio is maximized.[119–121] As shown in Figure A-1 (a), when γ is near 0.56, the space filling ratio is maximized for AlB_2, *ico*-$NaZn_{13}$, and *cub*-$NaZn_{13}$. Figure A-1 (b) shows a calculated phase diagram using hard-sphere model at γ=0.558, and highlights a suitable composition between two NCs to form a self-assembly structure. These thermodynamic predictions show that the possible BNSL structures at γ=0.558 are AB_2, *ico*-AB_{13}, and *cub*-AB_{13} (Figure A-2). In nature, AlB_2, *ico*-$NaZn_{13}$, and *cub*-$NaZn_{13}$ have these structures. AB_2 structure is constructed from alternating hexagonal planes made with nanocrystal A (NC-A) and B (NC-B). *ico*-AB_{13} is constructed with a primitive cubic unit cell with NC-A and icosahedron-shaped 13 NC-Bs located at the center of the cube. *cub*-AB_{13} has cuboctahedron-shaped 13 NC-Bs instead of icosahedron shape at the center of the cube. Among those possible structures, AB_2 is thought to be the most appropriate structure for QD-LEDs. In the AB_2 structure, C-QDs are neighboring each other with a hexagon-shape, which ensures efficient charge transport, and P-QDs, FRET acceptors, are located at the tetrahedral interstitial sites.

The solution of C-QDs and P-QDs are prepared in tetrachloroethene (TCE). To prepare BNSLs, the mixed solution is dried slowly to deposit BNSL thin films on different substrates as illustrated in Figure A-3. Films are deposited on Cu grids for TEM, on Si and SiO_2/Si for characterization, and ZnO/ITO/glass for device fabrication.

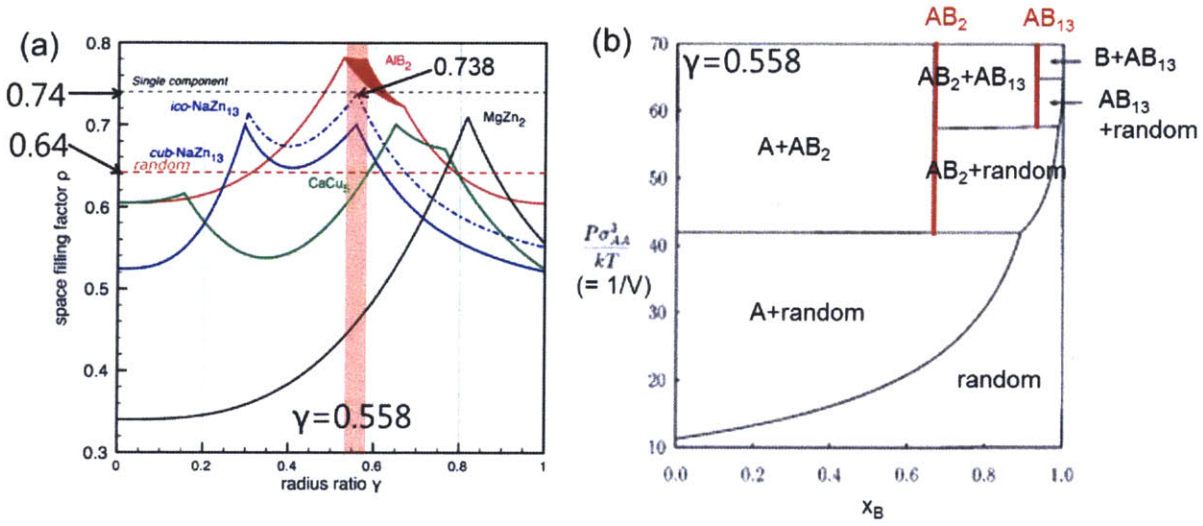

Figure A-1. (a) Space filling factor, ρ *vs.* radius ration between two spheres, γ showing the criteria for various binary ordered structures. Image adopted from Refs:[114,122,123] (b) Calculated phase diagram at γ=0.558 showing possible phases. Image adopted from Refs:[119]

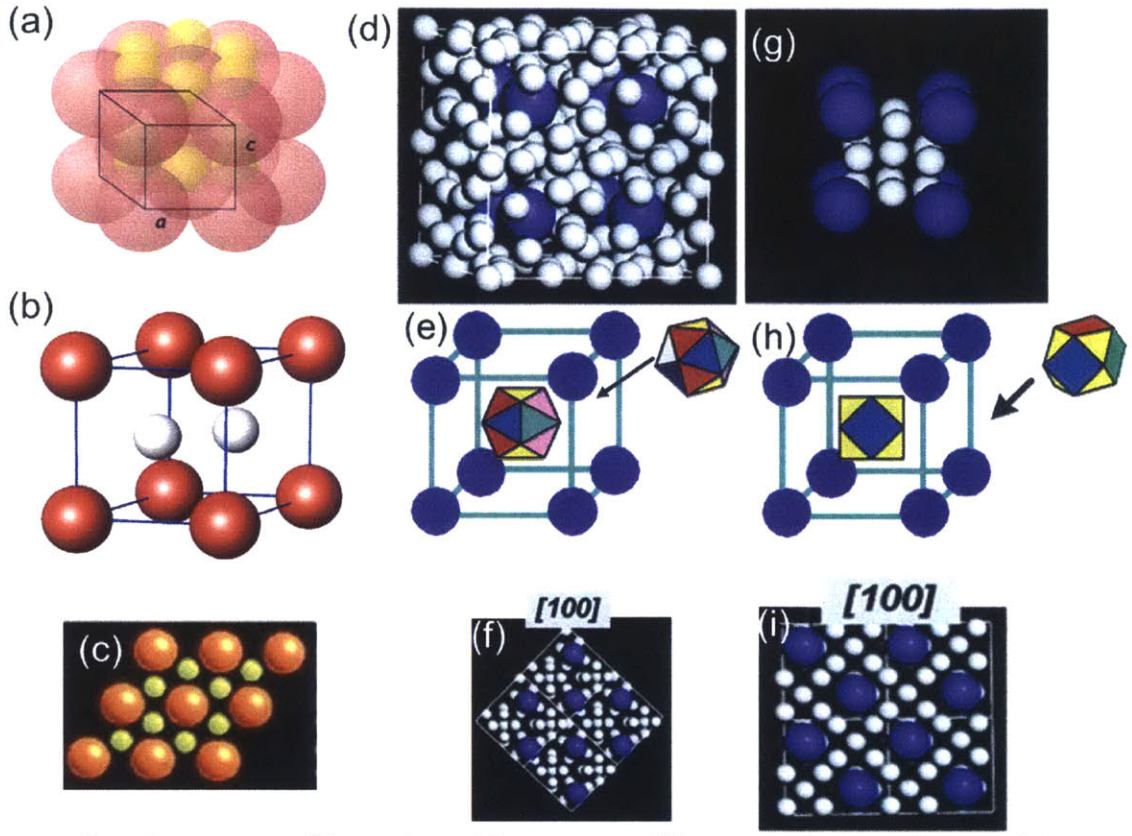

Figure A-2. AB_2 structure illustrating with (a) space filling model, (b) ball-and-stick model, and (c) (001) projection. Same illustration for *ico*-AB_{13} structure (d), (e), and (f) and for *cub*-AB_{13} structure (g), (h), and (i). Images adopted from Refs: [123–125]

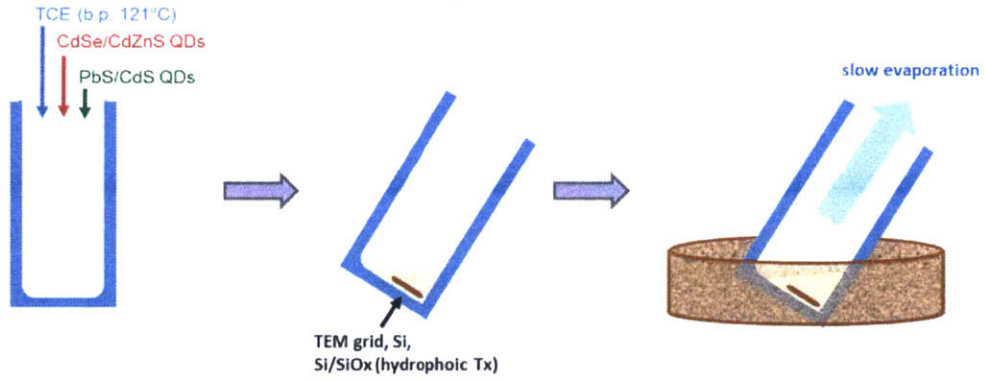

Figure A-3. Schematic diagram for BNSL preparation steps: Two different QDs are dissolved in TCE. The solution is slowly dried in tilted vial under controlled environments to deposit BNSL films on substrates.

A.3 Characterization

The BNSL films are imaged using TEM as shown in Figure A-4. Samples are prepared with different composition of C-QDs and P-QDs to find a condition yielding the largest domain size of AB_2 structures. Unexpectedly, in most cases a *cub*-AB_{13} structure is observed instead of a desired AB_2 structure. As described earlier, three self-assembly structures have the maximum ρ at γ=0.56, AB_2, *ico*-AB_{13}, and *cub*-AB_{13}. Throughout the various composition ranges, AB_2 is barely observed. Even in the composition of 1:2 (x_c:x_p), which is expected to be most favorable to AB_2 (Figure A-1 (b)), the area of *cub*-AB_{13} is larger than that of AB_2. In lower concentrations of P-QD (x_c:x_p down to 1:1), no BNSL is observed, instead, separated domains of P-QDs and C-QDs are observed. C-QD only domains are frequently observed in a wide range of x_c:x_p up to 1:10. In any tested condition, the area of AB_2 is not large enough for further characterization using other techniques rather than TEM. Thus, we use *cub*-AB_{13} instead of AB_2 throughout this section.

We examine whether we can deposit large-area BNSLs on various substrates for fabrication of devices. We deposited BNSLs of *cub*-AB_{13} structure on various substrates such as Si, thermally grown SiO_2 on Si, and sol-gel ZnO on patterend-ITO/glass. After making the surface hydrophobic with (3-Mercaptopropyl)trimethoxysilane (MPTS) treatment, BNSL layers are successfully deposited on those substrates. These BNSL layers are inspected with scanning electron microscopy (SEM) and fluorescent optical microscopy as shown in Figure A-5. They exhibit domain size up to 3.2 μm and well-ordered structures in each domain. In all samples, the micron-size domains are adjacent to each other forming a large continuous area (Figure A-5 (b) and (d)). Due to this morphology, BNSL can be used as an active layer in QD-LEDs.

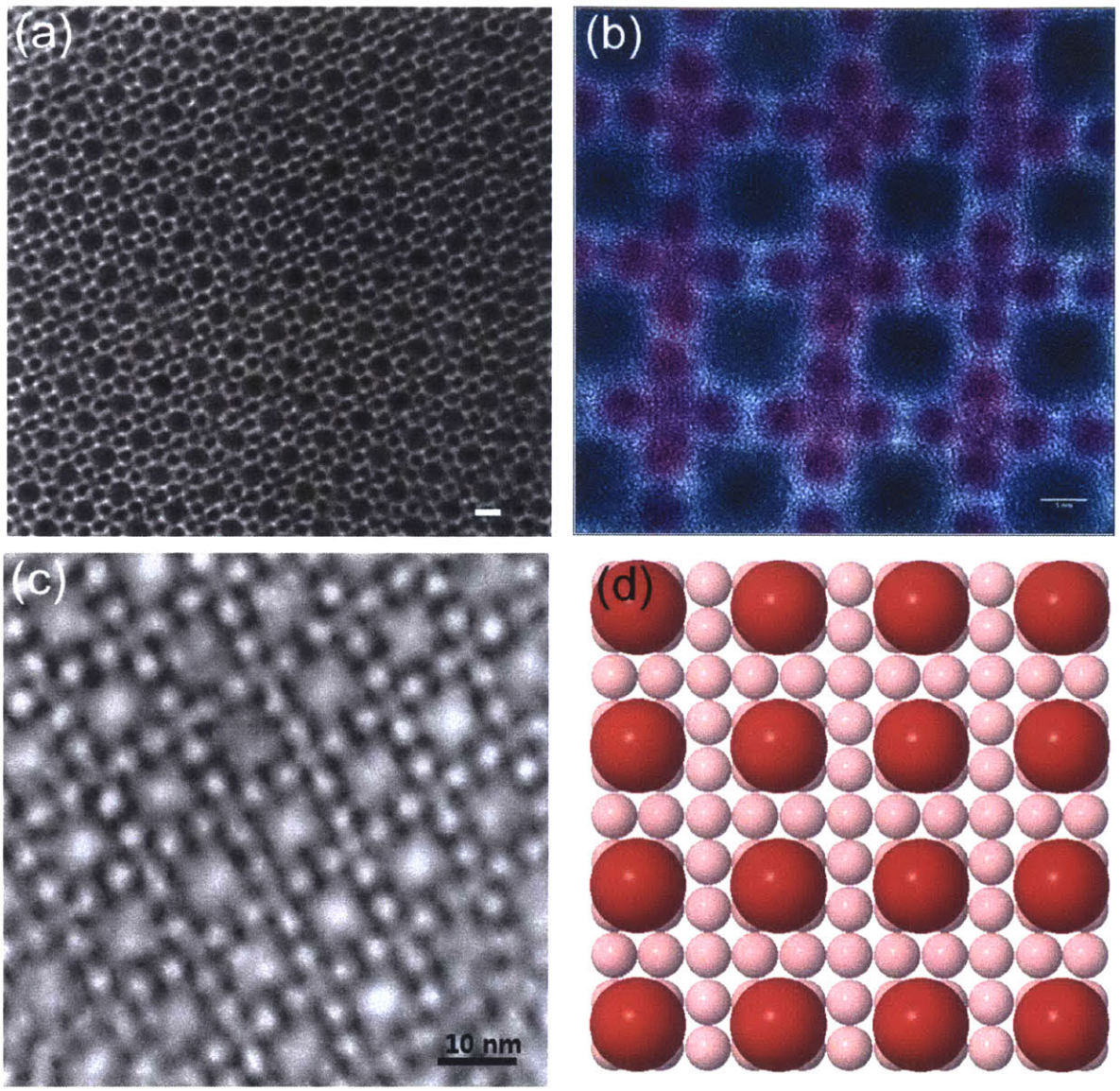

Figure A-4. (a) High-resolution (HR) TEM image and (b) false color image of *cub*-AB_{13} structure deposited on TEM grid. (c) Dark-field scanning transmission electron microscopy (DF-STEM) image and (d) (100) view of *cub*-AB_{13} structure, image taken from Refs:[114]

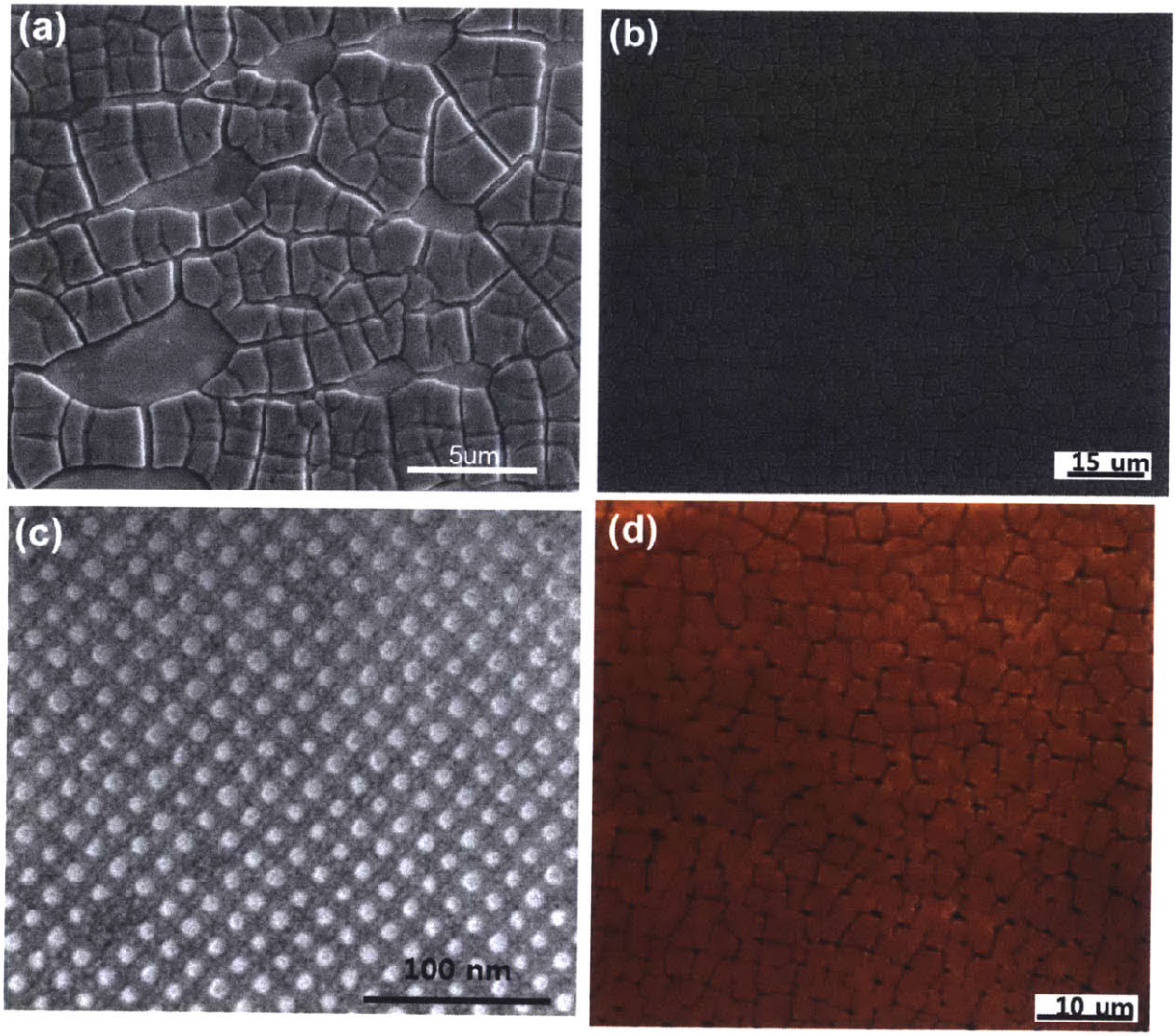

Figure A-5. SEM image of *cub*-AB_{13} BNSL thin films on (a) Si substrates and (b) and (c) on SiO_2 substrates. (d) Fluorescent optical microscopy images taken with 595 nm ± 25 nm band-pass filter.

The optical characterization of BNLS thin films demonstrates that FRET is more efficient in BNSLs than in spin-casted films. The spin-casted films are created with the same composition of QDs and exhibit a disordered structure. PL from C-QDs are efficiently quenched after incorporating P-QDs regardless of their structures. In contrast, PL from P-QDs increases only when the QDs have ordered AB_{13} structures. This is because in ordered BNSL structure, C-QDs are always neighboring with evenly distributed P-QDs, but in disordered structure, C-QDs are not always neighboring with P-QDs. Another evidence of energy transfer from C-QDs to P-QDs is a PL increase right after the excitation pulse.

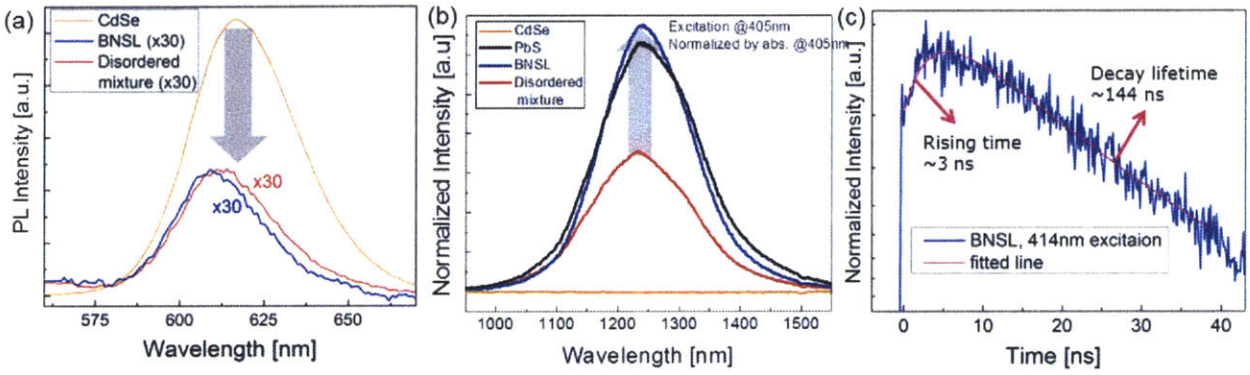

Figure A-6. Optical characterization showing (a) energy donation from C-QDs and (b) energy acceptance by P-QDs. (c) tPL demonstrating a rising time at the beginning by FRET.

A.4 Device Applications

BNSL QD-LEDs are fabricated using this large area *cub*-AB_{13} BNSLs. We test whether the quality of BNSLs is sufficient to be used as an active layer in QD-LEDs. We use a 'type-IV' structure for BNSL QD-LED as demonstrated in section 2.5. N,N'-Bis(3-methylphenyl)-N,N'-bis(phenyl)-9,9-spirobifluorene (spiro-NPB) is used as HTL and ZnO is used as ETL (Figure A-7). The electrical characterizations of these devices are presented in Figure A-8. The performance of device is not impressive as a turn-on voltage is near 1.2 V and a peak EQE is 0.5 %. One possible reason for this low performance is the low conductivity of

BNSL films due to their large thickness. The thickness of BNSL QD films is 80–100 nm, which is much thicker than the QD layers in SWIR QD-LEDs, 10nm, from section 2.5.

Due to a failure to produce large area AB_2 structure, EQE drooping phenomena is not studied. In the *cub*-AB_{13} structure, C-QDs are surrounded by P-QDs in as seen in Figure A-2, thus, charge cannot be transported through C-QDs. Therefore, P-QDs will be participated in both charge transports and light emission.

In this appendix, we demonstrate the formation of BNSLs with different semiconductor–semiconductor NCs on various substrates. The structure of BNSL is confirmed with TEM and their domain size is observed with SEM and optical microscopy. By fabricating and characterizing the BNSL QD-LEDs, we demonstrate that BNSL thin films with core/shell QDs have sufficient quality to be used as an active layer in devices. To use BNSLs in devices, fine control of their self-assembly is required.

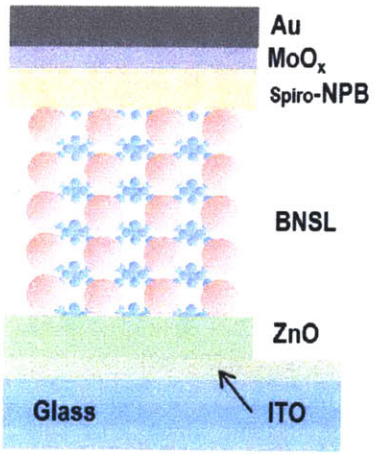

Figure A-7. Schematic illustration for a structure of BNSL LEDs.

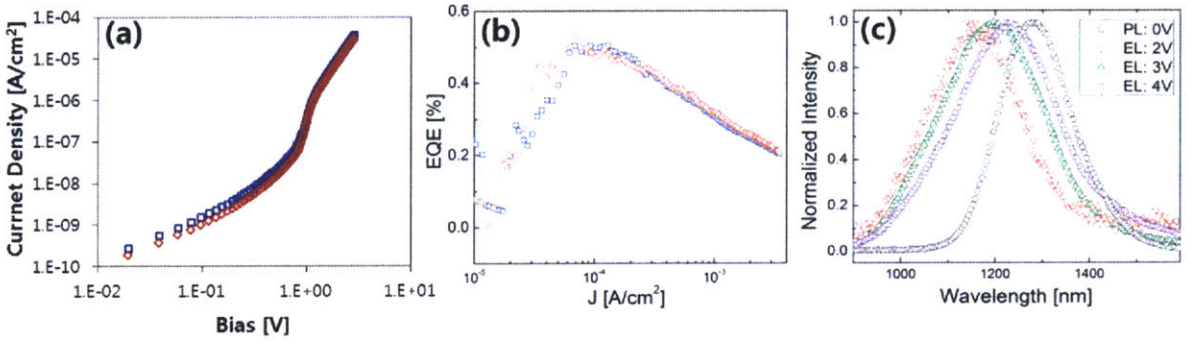

Figure A-8. Electrical characterization of BNSL-LEDs. (a) J-V, (b) EQE, and (c) electroluminescence (EL) spectra.

References

[1] M. G. Bawendi, M. L. Steigerwald, L. E. Brus, *Annu. Rev. Phys. Chem.* **1990**, *41*, 477.

[2] F. W. Wise, *Acc. Chem. Res.* **2000**, *33*, 773.

[3] G. Konstantatos, E. H. Sargent, *Colloidal Quantum Dot Optoelectronics and Photovoltaics*, Cambridge University Press, **2013**.

[4] D. Norris, in *Nanocrystal Quantum Dots, Second Ed.* (Ed.: Klimov), CRC Press, **2010**, pp. 63–96.

[5] O. Madelung, U. Rössler, M. Schulz; SpringerMaterials; sm_lbs_978-3-540-31360-1_889 (Springer-Verlag GmbH, Heidelberg, 1998), http://materials.springer.com/lb/docs/sm_lbs_978-3-540-31360-1_889; accessed: 30-03-2015, 10:58:07 GMT-0400 (Eastern Daylight Time) / O. Madelung, U. Rössler, M. Schulz, Eds. , in *SpringerMaterials - Landolt-Börnstein Database.*

[6] S.-H. Wei, A. Zunger, *Phys. Rev. B* **1997**, *55*, 13605.

[7] S. E. Kohn, P. Y. Yu, Y. Petroff, Y. R. Shen, Y. Tsang, M. L. Cohen, *Phys. Rev. B* **1973**, *8*, 1477.

[8] O. Madelung, U. Rössler, M. Schulz; SpringerMaterials; sm_lbs_978-3-540-31360-1_885 (Springer-Verlag GmbH, Heidelberg, 1998), http://materials.springer.com/lb/docs/sm_lbs_978-3-540-31360-1_885; accessed: 30-03-2015, 10:59:00 GMT-0400 (Eastern Daylight Time) / O. Madelung, U. Rössler, M. Schulz, Eds. , in *SpringerMaterials - Landolt-Börnstein Database.*

[9] H. Choi, J. H. Ko, Y. H. Kim, S. Jeong, *J. Am. Chem. Soc.* **2013**, *135*, 5278.

[10] L. Cademartiri, E. Montanari, G. Calestani, A. Migliori, A. Guagliardi, G. A. Ozin, *J. Am. Chem. Soc.* **2006**, *128*, 10337.

[11] L.-Y. Chang, Development of Low-Temperature Solution-Processed Colloidal Quantum Dot-Based Solar Cells, Ph.D Thesis, Massachusetts Institute of Technology, **2013**.

[12] M. A. Hines, G. D. Scholes, *Adv. Mater.* **2003**, *15*, 1844.

[13] G. Qian, Z. Zhong, M. Luo, D. Yu, Z. Zhang, Z. Y. Wang, D. Ma, *Adv. Mater.* **2009**, *21*, 111.

[14] J. R. Sommer, R. T. Farley, K. R. Graham, Y. Yang, J. R. Reynolds, J. Xue, K. S. Schanze, *ACS Appl. Mater. Interfaces* **2009**, *1*, 274.

[15] O. E. Semonin, J. C. Johnson, J. M. Luther, A. G. Midgett, A. J. Nozik, M. C. Beard, *J. Phys. Chem. Lett.* **2010**, *1*, 2445.

[16] S. Hatami, C. Wurth, M. Kaiser, S. Leubner, S. Gabriel, L. Bahrig, V. Lesnyak, J. Pauli, N. Gaponik, A. Eychmuller, U. Resch-Genger, *Nanoscale* **2015**, *7*, 133.

[17] L. Cademartiri, J. Bertolotti, R. Sapienza, D. S. Wiersma, G. von Freymann, G. A. Ozin, *J. Phys. Chem. B* **2006**, *110*, 671.

[18] M. C. Weidman, M. E. Beck, R. S. Hoffman, F. Prins, W. A. Tisdale, *ACS Nano* **2014**, *8*, 6363.

[19] M. P. Hendricks, M. P. Campos, G. T. Cleveland, I. J.-L. Plante, J. Owen, **2015**, *Submitted.*

[20] D. Zherebetskyy, M. Scheele, Y. Zhang, N. Bronstein, C. Thompson, D. Britt, M. Salmeron, P. Alivisatos, L.-W. Wang, *Science* **2014**, *344*, 1380.

[21] Z. Ning, O. Voznyy, J. Pan, S. Hoogland, V. Adinolfi, J. Xu, M. Li, A. R. Kirmani, J.-P. Sun, J. Minor, K. W. Kemp, H. Dong, L. Rollny, A. Labelle, G. Carey, B. Sutherland, I. Hill, A. Amassian, H. Liu, J. Tang, O. M. Bakr, E. H. Sargent, *Nat Mater* **2014**, *13*, 822.

[22] M. Yuan, K. W. Kemp, S. M. Thon, J. Y. Kim, K. W. Chou, A. Amassian, E. H. Sargent, *Adv. Mater.* **2014**, *26*, 3513.

[23] I. Moreels, Y. Justo, B. De Geyter, K. Haustraete, J. C. Martins, Z. Hens, *ACS Nano* **2011**, *5*, 2004.

[24] D. Deng, J. Cao, J. Xia, Z. Qian, Y. Gu, Z. Gu, W. J. Akers, *Eur. J. Inorg. Chem.* **2011**, *2011*, 2422.

[25] D. K. Harris, Synthesis and Characterization of Infrared Quantum Dots, Ph.D Thesis, Massachusetts Institute of Technology, **2014**.

[26] L.-Y. Chang, R. R. Lunt, P. R. Brown, V. Bulović, M. G. Bawendi, *Nano Lett.* **2013**, *13*, 994.

[27] E. H. Sargent, *Nat Phot.* **2009**, *3*, 325.

[28] M. Graetzel, R. A. J. Janssen, D. B. Mitzi, E. H. Sargent, *Nature* **2012**, *488*, 304.

[29] S. M. Geyer, Science and Applications of Infrared Semiconductor Nanocrystals, Ph.D. Thesis, Massachusetts Institute of Technology, **2010**.

[30] S. M. Geyer, J. M. Scherer, N. Moloto, F. B. Jaworski, M. G. Bawendi, *ACS Nano* **2011**, *5*, 5566.

[31] L. Sun, J. J. Choi, D. Stachnik, A. C. Bartnik, B.-R. Hyun, G. G. Malliaras, T. Hanrath, F. W. Wise, *Nat Nano* **2012**, *7*, 369.

[32] Y. Shirasaki, G. J. Supran, M. G. Bawendi, V. Bulovic, *Nat Phot.* **2013**, *7*, 13.

[33] G. J. Supran, K. W. Song, G. W. Hwang, R. E. Correa, J. Scherer, E. A. Dauler, Y. Shirasaki, M. G. Bawendi, V. Bulović, *Adv. Mater.* **2015**, *27*, 1437.

[34] Y. T. Lim, S. Kim, A. Nakayama, N. E. Stott, M. G. Bawendi, J. V. Frangioni, *Mol. Imaging* **2003**, *2*, 50.

[35] O. T. Bruns, T. S. Bischof, D. K. Harris, Y. Shi, L. Riedemann, T. Reiberger, A. Bartelt, F. B. Jaworski, D. Franke, M. W. B. Wilson, O. Chen, H. Wei, G. W. Hwang, D. Montena, I. Coropceanu, J. Kloepper, J. Heeren, D. Fukumura, R. K. Jain, M. G. Bawendi, *Nat. Med.* **2015**, *Submitted.*

[36] M. G. Bawendi, P. J. Carroll, W. L. Wilson, L. E. Brus, *J. Chem. Phys.* **1992**, *96*, 946.

[37] E. Lifshitz, A. Glozman, I. D. Litvin, H. Porteanu, *J. Phys. Chem. B* **2000**, *104*, 10449.

[38] M. Nirmal, C. B. Murray, D. J. Norris, M. G. Bawendi, *Zeitschrift für Phys. D Atoms, Mol. Clust.* **1993**, *26*, 361.

[39] V. I. Klimov, *Nanocrystal Quantum Dots*, Boca Raton : CRC Press, 2010., **2010**.

[40] J. M. Caruge, J. E. Halpert, V. Wood, V. Bulovic, M. G. Bawendi, *Nat. Photonics* **2008**, *2*, 247.

[41] Z. Popović, W. Liu, V. P. Chauhan, J. Lee, C. Wong, A. B. Greytak, N. Insin, D. G. Nocera, D. Fukumura, R. K. Jain, M. G. Bawendi, *Angew. Chemie* **2010**, *49*, 8649.

[42] M. V Jarosz, V. J. Porter, B. R. Fisher, M. A. Kastner, M. G. Bawendi, *Phys. Rev. B - Condens. Matter Mater. Phys.* **2004**, *70*, 195327.

[43] G. Konstantatos, E. H. Sargent, *Infrared Phys. Technol.* **2011**, *54*, 278.

[44] G. Konstantatos, E. H. Sargent, *Nat. Nanotechnol.* **2010**, *5*, 391.

[45] J. Tang, E. H. Sargent, *Adv. Mater.* **2011**, *23*, 12.

[46] E. Lifshitz, M. Brumer, A. Kigel, A. Sashchiuk, M. Bashouti, M. Sirota, E. Galun, Z. Burshtein, A. Q. Le Quang, I. Ledoux-Rak, J. Zyss, *J. Phys. Chem. B* **2006**, *110*, 25356.

[47] V. J. Porter, S. Geyer, J. E. Halpert, M. a. Kastner, M. G. Bawendi, *J. Phys. Chem. C* **2008**, *112*, 2308.

[48] H. Zhao, M. Chaker, N. Wu, D. Ma, *J. Mater. Chem.* **2011**, *21*, 8898.

[49] W. Liu, Design and Synthesis of Biocompatible Fluorescent Semi-Conductor Nanocrystals for in-Vivo and in-Vitro Imaging / Sensing Applications, Ph.D Thesis, Massachusetts Institute of Technology, **2010**.

[50] M. Ohring, D. Gall, *Materials Science of Thin Films*, Academic Press, San Diego, CA, **2002**.

[51] D. A. Porter, K. E. Easterling, *Phase Transformations in Metals and Alloys*, Chapman & Hall, London, UK, **1992**.

[52] M. Sykora, A. Y. Koposov, J. A. McGuire, R. K. Schulze, O. Tretiak, J. M. Pietryga, V. I. Klimov, *ACS Nano* **2010**, *4*, 2021.

[53] E. Kinder, P. Moroz, G. Diederich, A. Johnson, M. Kirsanova, A. Nemchinov, T. O'Connor, D. Roth, M. Zamkov, *J. Am. Chem. Soc.* **2011**, *133*, 20488.

[54] A. F. Wells, *Structural Inorganic Chemistry*, Oxford Science, **1984**.

[55] S. Musikhin, V. Il'in, O. Rabizo, L. Bakueva, *Semiconductors* **1997**, *31*, 46.

[56] Bethke P.M., "Cd-Pb-S Phase Diagram," can be found under http://www1.asminternational.org/AsmEnterprise/APD.

[57] Leute V., "Cd-Pb-S Phase Diagram," can be found under http://www1.asminternational.org/AsmEnterprise/APD.

[58] V. K. LaMer, R. H. Dinegar, *J. Am. Chem. Soc.* **1950**, *72*, 4847.

[59] C. B. Murray, C. R. Kagan, M. G. Bawendi, *Annu. Rev. Mater. Sci.* **2000**, *30*, 545.

[60] A. Baldan, *J. Mater. Sci.* **2002**, *37*, 2171.

[61] P. M. Allen, Semiconductor Nanocrystals: Synthesis, Mechanisms of Formation, and Applications in Biology, Ph.D. Thesis, Massachusetts Institute of Technology, **2010**.

[62] J. M. Pietryga, D. J. Werder, D. J. Williams, J. L. Casson, R. D. Schaller, V. I. Klimov, J. a Hollingsworth, *J. Am. Chem. Soc.* **2008**, *130*, 4879.

[63] J. Tang, L. Brzozowski, D. A. R. Barkhouse, X. Wang, R. Debnath, R. Wolowiec, E. Palmiano, L. Levina, A. G. Pattantyus-Abraham, D. Jamakosmanovic, others, *ACS Nano* **2010**, *4*, 869.

[64] N. Zhao, T. P. Osedach, L.-Y. Chang, S. M. Geyer, D. Wanger, M. T. Binda, A. C. Arango, M. G. Bawendi, V. Bulovic, *ACS Nano* **2010**, *4*, 3743.

[65] R. T. Lechner, G. Fritz-Popovski, M. Yarema, W. Heiss, O. Paris, in *MRS 2011 Fall Meet.*, Boston, MA Nov. **2011**

[66] Y. Justo, L. K. Sagar, S. Flamee, Q. Zhao, A. Vantomme, Z. Hens, *ACS Nano* **2014**, *8*, 7948.

[67] G. Hong, Y. Zou, A. L. Antaris, S. Diao, D. Wu, K. Cheng, X. Zhang, C. Chen, B. Liu, Y. He, J. Z. Wu, J. Yuan, B. Zhang, Z. Tao, C. Fukunaga, H. Dai, *Nat Commun* **2014**, *5*, 4206.

[68] H.-S. Han, E. Niemeyer, Y. Huang, W. S. Kamoun, J. D. Martin, J. Bhaumik, Y. Chen, S. Roberge, J. Cui, M. R. Martin, D. Fukumura, R. K. Jain, M. G. Bawendi, D. G. Duda, *Proc. Natl. Acad. Sci.* **2015**, *112* , 1350.

[69] M. Howarth, W. Liu, S. Puthenveetil, Y. Zheng, L. F. Marshall, M. M. Schmidt, K. D. Wittrup, M. G. Bawendi, A. Y. Ting, *Nat Meth* **2008**, *5*, 397.

[70] B. Dubertret, P. Skourides, D. J. Norris, V. Noireaux, A. H. Brivanlou, A. Libchaber, *Sci.* **2002**, *298* , 1759.

[71] N. Tessler, V. Medvedev, M. Kazes, S. Kan, U. Banin, *Sci.* **2002**, *295* , 1506.

[72] Y. Liu, M. Gibbs, J. Puthussery, S. Gaik, R. Ihly, H. W. Hillhouse, M. Law, *Nano Lett.* **2010**, *10*, 1960.

[73] D. D. Wanger, R. E. Correa, E. A. Dauler, M. G. Bawendi, *Nano Lett.* **2013**, *13*, 5907.

[74] D. Bozyigit, V. Wood, *J. Mater. Chem. C* **2014**, *2*, 3172.

[75] D. Bozyigit, S. Volk, O. Yarema, V. Wood, *Nano Lett.* **2013**, *13*, 5284.

[76] D.-K. Ko, P. R. Brown, M. G. Bawendi, V. Bulović, *Adv. Mater.* **2014**, *26*, 4845.

[77] S. Kasap, *Principles of Electronic Materials and Devices*, McGraw-Hill Education, **2005**.

[78] D. D. W. Grinolds, P. R. Brown, D. K. Harris, V. Bulovic, M. G. Bawendi, *Nano Lett.* **2015**, *15*, 21.

[79] J. T. Heath, J. D. Cohen, W. N. Shafarman, *J. Appl. Phys.* **2004**, *95*, 1000.

[80] C. E. Michelson, A. V. Gelatos, J. D. Cohen, *Appl. Phys. Lett.* **1985**, *47*, 412.

[81] D. Bozyigit, M. Jakob, O. Yarema, V. Wood, *ACS Appl. Mater. Interfaces* **2013**, *5*, 2915.

[82] P. Blood, J. W. Orton, *The Electrical Characterization of Semiconductors: Majority Carriers and Electron States*, Academic Press, **1992**.

[83] D. K. Schroder, *Semiconductor Material and Device Characterization*, John Wiley & Sons, Inc., **2006**.

[84] J. Clifford, G. Konstantatos, *Nat. Nanotechnol.* **2008**, *4*, 40.

[85] J. Y. Kim, O. Voznyy, D. Zhitomirsky, E. H. Sargent, *Adv. Mater.* **2013**, *25*, 4986.

[86] C.-H. M. Chuang, P. R. Brown, V. Bulović, M. G. Bawendi, *Nat. Mater.* **2014**, *13*, 796.

[87] D. Zhitomirsky, O. Voznyy, S. Hoogland, E. H. Sargent, *ACS Nano* **2013**, *7*, 5282.

[88] A. H. Ip, S. M. Thon, S. Hoogland, O. Voznyy, D. Zhitomirsky, R. Debnath, L. Levina, L. R. Rollny, G. H. Carey, A. Fischer, K. W. Kemp, I. J. Kramer, Z. Ning, A. J. Labelle, K. W. Chou, A. Amassian, E. H. Sargent, *Nat. Nanotechnol.* **2012**, *7*, 577.

[89] D. Zhitomirsky, O. Voznyy, L. Levina, S. Hoogland, K. W. Kemp, A. H. Ip, S. M. Thon, E. H. Sargent, *Nat. Commun.* **2014**, *5*, 3803.

[90] P. Stadler, B. R. Sutherland, Y. Ren, Z. Ning, A. Simchi, S. M. Thon, S. Hoogland, E. H. Sargent, *ACS Nano* **2013**, *7*, 5757.

[91] G. H. Carey, I. J. Kramer, P. Kanjanaboos, G. Moreno-bautista, O. Voznyy, L. Rollny, J. A. Tang, S. Hoogland, E. H. Sargent, *ACS Nano* **2014**, *8*, 11763.

[92] C.-H. Chuang, A. Maurano, R. Brandt, G. W. Hwang, J. Jean, T. Buonassisi, V. Bulovic, M. G. Bawendi, *Nano Lett.* **2015**, DOI:10.1021/acs.nanolett.5b00513 *(ASAP)*.

[93] D. Bozyigit, W. M. M. Lin, N. Yazdani, O. Yarema, V. Wood, *Nat. Commun.* **2015**, *6*, 6180.

[94] K. S. Jeong, J. Tang, H. Liu, J. Kim, A. W. Schaefer, K. Kemp, L. Levina, X. Wang, S. Hoogland, R. Debnath, L. Brzozowski, E. H. Sargent, J. B. Asbury, *ACS Nano* **2012**, *6*, 89.

[95] E. J. D. Klem, H. Shukla, S. Hinds, D. D. MacNeil, L. Levina, E. H. Sargent, *Appl. Phys. Lett.* **2008**, *92*, 212105.

[96] Z. Ning, Y. Ren, S. Hoogland, O. Voznyy, L. Levina, P. Stadler, X. Lan, D. Zhitomirsky, E. H. Sargent, *Adv. Mater.* **2012**, *24*, 6295.

[97] D. Kim, D. H. Kim, J. H. Lee, J. C. Grossman, *Phys. Rev. Lett.* **2013**, *110*, 196802.

[98] S. J. Oh, N. E. Berry, J.-H. Choi, E. A. Gaulding, T. Paik, S.-H. Hong, C. B. Murray, C. R. Kagan, *ACS Nano* **2013**, *7*, 2413.

[99] I. J. Kramer, E. H. Sargent, *Chem. Rev.* **2014**, *114*, 863.

[100] P. R. Brown, D. Kim, R. R. Lunt, N. Zhao, M. G. Bawendi, J. C. Grossman, V. Bulović, *ACS Nano* **2014**, *8*, 5863.

[101] T. S. Mentzel, D. D. Wanger, N. Ray, B. J. Walker, D. Strasfeld, M. G. Bawendi, M. A. Kastner, *Nano Lett.* **2012**, *12*, 4404.

[102] P. Guyot-Sionnest, *J. Phys. Chem. Lett.* **2012**, *3*, 1169.

[103] J. Gao, J. C. Johnson, *ACS Nano* **2012**, *6*, 3292.

[104] J. Gao, J. Zhang, J. van de Lagemaat, J. C. Johnson, M. C. Beard, *ACS Nano* **2014**, *8*, 12814.

[105] J. F. Moulder, W. F. Stickle, P. E. Sobol, K. D. Bomben, *Handbook of X-Ray Photoelectron Spectroscopy*, Perkin-Elmer Corporation, Eden Prairie, MN, **1992**.

[106] J. M. Berg, J. L. Tymoczkom, L. Stryer, *Biochemistry*, W. H. Freeman And Company, New York, **2002**.

[107] G. Kresse, J. Furthmüller, *Comput. Mater. Sci.* **1996**, *6*, 15.

[108] J. P. Perdew, K. Burke, M. Ernzerhof, *Phys. Rev. Lett.* **1996**, *77*, 3865.

[109] G. Henkelman, A. Arnaldsson, H. Jónsson, *Comput. Mater. Sci.* **2006**, *36*, 354.

[110] O. Voznyy, D. Zhitomirsky, P. Stadler, Z. Ning, S. Hoogland, E. H. Sargent, *ACS Nano* **2012**, *6*, 8448.

[111] O. Voznyy, S. M. Thon, A. H. Ip, E. H. Sargent, *J. Phys. Chem. Lett.* **2013**, *4*, 987.

[112] C. Giansante, I. Infante, E. Fabiano, R. Grisorio, G. P. Suranna, G. Gigli, *J. Am. Chem. Soc.* **2015**, *137*, 1875.

[113] M. T. Frederick, V. A. Amin, E. A. Weiss, *J. Phys. Chem. Lett.* **2013**, *4*, 634.

[114] J. Chen, X. Ye, C. Murray, *ACS Nano* **2010**, *4*, 2374.

[115] J. J. Urban, D. V Talapin, E. V Shevchenko, C. B. Murray, *J. Am. Chem. Soc.* **2006**, *128*, 3248.

[116] J. J. Urban, D. V Talapin, E. V Shevchenko, C. R. Kagan, C. B. Murray, *Nat. Mater.* **2007**, *6*, 115.

[117] J. Bang, U. Jeong, D. Y. Ryu, T. P. Russell, C. J. Hawker, *Adv. Mater.* **2009**, *21*, 4769.

[118] J. Iveland, L. Martinelli, J. Peretti, J. S. Speck, C. Weisbuch, *Phys. Rev. Lett.* **2013**, *110*, 177406.

[119] X. Cottin, P. a. Monson, *J. Chem. Phys.* **1995**, *102*, 3354.

[120] M. Eldridge, P. Madden, D. Frenkel, *Nature* **1993**, *365*, 35.

[121] B. A. Grzybowski, C. E. Wilmer, J. Kim, K. P. Browne, K. J. M. Bishop, *Soft Matter* **2009**, *5*, 1110.

[122] M. I. Bodnarchuk, M. V Kovalenko, W. Heiss, D. V Talapin, *J. Am. Chem. Soc.* **2010**, *132*, 11967.

[123] Z. Chen, S. O'Brien, *ACS Nano* **2008**, *2*, 1219.

[124] B. A. Korgel, *Nat. Mater.* **2010**, *9*, 701.

[125] E. V Shevchenko, D. V Talapin, S. O. Brien, C. B. Murray, *J. Am. Chem. Soc.* **2005**, *127*, 8741.

[126] J. L. Miller, *Principles of Infrared Technology : A Practical Guide to the State of the Art*, Van Nostrand Reinhold, New York, **1994**.

[127] W. Shockley, H. J. Queisser, *J. Appl. Phys.* **1961**, *32*, 510.

[128] G. Nair, L.-Y. Chang, S. M. Geyer, M. G. Bawendi, *Nano Lett.* **2011**, *11*, 2145.

[129] J. Noolandi, K. M. Hong, *J. Chem. Phys.* **1979**, *70*, 3230.

[130] D. D. Wagman, *The NBS Tables of Chemical Thermodynamic Properties: Selected Values for Inorganic and C1 and C2 Organic Substances in SI Units*, American Chemical Society And The American Institute Of Physics For The National Bureau Of Standards, **1982**.